Synthesis, Characterization and Application of Barium Titanate Particles in Light Emitting Devices

Antoine Dumont

A THESIS SUBMITTED TO
THE FACULTY OF GRADUATE STUDIES
IN PARTIAL FULFILLMENT FOR THE REQUIREMENTS
FOR THE DEGREE OF
MASTER OF SCIENCE

GRADUATE PROGRAM IN PHYSICS AND ASTRONOMY
YORK UNIVERSITY
TORONTO, ONTARIO
April 2016

Abstract

The main objective of this project is to create barium titanate nanoparticles that are better suited for use in screen-printed electroluminescent devices than commercially available particles. As the name suggests, these devices produce light by electroluminescence. They need to be as thin and malleable as possible, so as to increase their performance and make them suitable for a greater number of applications than presently possible. Typically, these devices are built by superimposing printed layers, made respectively of conductive, insulating (barium titanate), luminescent and, again, conductive materials.

The barium titanate nanoparticles created for this project will enable a more efficient use of the necessary electric energy for the emission of light. They could also potentially reduce the thickness of the overall device, which would result in lower production costs and increased brightness.

There is one key property to observe when attempting to reduce the electric energy used by this light-emitting device: the dielectric constant of barium titanate. This property can be adjusted by altering the size, crystal structure and chemical composition of the particles. The size can technically be tweaked by varying the concentration of acetylacetone (although the results were inconclusive in this study), while the chemical composition can be fine-tuned by the addition of a dopant – in this case, lanthanum.

For this project, the new barium titanate particles are synthesized through two different protocols, which make the study of a wide spectrum of electric and structural properties possible. Four main characterization tools were employed to study the new particles: the scanning electron microscope was used to determine their morphology; the powder X-ray diffractometer was used

to determine their structure; once they were printed as a dielectric layer, the profilometer was used to determine the average thickness of the printed film; and the impedance spectrometer was used to determine their dielectric constant (the Nyquist and Bode plots of the various samples are presented in this thesis).

It was expected that the samples of undoped barium titanate would show a slight increase in the dielectric constant with a decrease in particle size. However, since the size of the particles turned out to be the same within statistical error, it wasn't possible to determine a correlation between the dielectric constant and particle size.

On the other hand, there was a marked improvement in the general potency (including the dielectric constant) of the barium titanate doped with lanthanum. One concentration in particular (0.5% Lan) yielded a very high dielectric constant of 168 ± 9 (mixed with epoxy), which is 340% higher than that of the best undoped material, which is 49 ± 5 (mixed with epoxy). It should be noted that this marked difference lowers to 250% when considering the difference in concentration of barium carbonate within the samples. A new series of doped samples was created to verify the results and the 0.5% La-doped material was confirmed to be optimal with the highest dielectric constant, but by a small margin above the 0,7% La-doped powder.

This observation is confirmed by luminescence measurements (3% error) done in a dark environment (evaluated at 0.0 nW of light). The 0.5% Lan samples generated significantly more light, at an average of 83.7 nW versus 52.3 nW for the best un-doped sample, and 29.1 nW for commercially available barium titanate. One of the 0.5% Lan samples gave an extremely interesting result by emitting an astonishing 652 nW. Although the result was not reproduced with new samples, it was not considered a complete anomaly either.

Acknowledgements

I would like to express my gratitude to my research supervisor Prof. Sylvie Morin for her continuous support during my M. Sc. degree. Through her advices and guidance as I worked on my research I was able to learn extensively how to be a finer scientist and I feel better suited to confront the challenges that await me after this project. I am very grateful for this.

I would also like to thank the rest of my thesis committee Prof. William Pietro and Prof. William van Wijngaarden for their valuable insight on my work, their pin-pointed questions that were always asked respectfully in an educative manner, as well as their encouragements. A particular thank you to Prof. Pietro for letting me work in his laboratory during the screen-printing process and letting me use the materials and devices in play.

A large amount of gratitude goes to the profesionals at Scobil Inc. who gave me some of their commercial $BaTiO_3$ powder to compare with my experimental material. They also let me borrow an essential circuit board to activate the electroluminescence in my devices.

I'd like to thank my research group colleagues for the great environment in which I worked during my degree. I was a pleasure to have many stimulating discussions and share those intense, stressful, funny and merry moments with all of them. A special thank you goes to Takyi (Frederick) Ofori who worked with me on the synthesis of barium titanate during his undergraduate degree in Chemistry. It was a great experience to share my work with this dedicated person that I know will do great things in the future. With his help, this project that had a difficult beginning was able to return on track and yield great results.

The last person, and certainly not the least, I would like to thank is the woman I've been sharing my life for almost eight years : Élyssa Marcoux Bissoondath. Not only was I able to go

through my degree a tenfold more easily thanks to her amazing encouragements, but she also always managed to help me by reading and correcting my written tasks and presentations. I appreciate enormously the time and patience it took to accompany me on this journey.

Table of Contents

List of Figures

Chapter 1: Introduction

1.1 Dielectric Permittivity of $BaTiO_3$

The dielectric permittivity (DP) of a material is its ability to store electric energy when a an electric field is applied to it. The material has a polarizable structure that rotates the electric charges proportionally to the field. The relative permittivity (ε_r, ε in this thesis) is simply the DP but expressed as a ratio relative to the permittivity of vacuum. Dielectrics are used to increase the accumulation of charges in capacitors, since they can store electric energy from a field more efficiently than if there were only vacuum between the conductive plates. Historically, the relative permittivity has more commonly been referred to as the dielectric constant and is still used in the scientific community. The term is technically problematic because it has been known for a long time that the "constant" varies according to the frequency of the electric field acting on the material [1]. Therefore, organizations in charge of setting scientific standards increasingly deplore the use of the term [2].

Barium titanate ($BaTiO_3$) is an oxide of the perovskite family, which inlcudes any material with the same ABX_3 structure as calcium titanate, also referred to as perovskite, an abundant mineral discovered in 1839 [3]. $BaTiO_3$ was first intentionally synthesised during World War II for the production of capacitors. The supply line of mica, which was the principal dielectric used in capacitors at the time, was threatened and scientists had to turn to new materials. Another common dielectric, titanium dioxide (TiO_2), was reported as showing interesting hikes in its dielectric permittivity when doped with barium oxide (BaO). A proper combination of the two gave a $BaTiO_3$ compound, which then showed a permittivity remarkably

higher than that of any other dielectric [4]. In 1946, It was established that this marked improvement came from the ferroelectric behavior of the $BaTiO_3$ crystal [5,6]. Since then, $BaTiO_3$ has been used as an international standard for dielectric permittivity.

Synthesizing barium titanate is not complicated and can be done in various ways. However, it is still unclear how to create the most dielectrically potent barium titanate crystal. The dielectric constant of $BaTiO_3$ is correlated to its ferroelectricity which depends on its crystal structure, the morphology of the particles and the possible dopants. Many researchers were inspired by the idea of figuring out precisely how these distinct parameters impact the dielectric constant. Despite a considerable amount of research, we still lack a global perspective on how the material is influenced by these variables.

1.2 Applications of High Dielectric Material and Thin Films

With the constant miniaturization of hardware, researchers in nanotechnology must find a way of maintaining or improving the processing performance of various devices, within a decreasing amount of space. The study of high-ε dielectrics such as barium titanate is crucial in the advancement of the field of condensed matter. Emerging applications such as Dynamic Random Access Memory (DRAM) demand extremely small dielectric layers in the capacitors (at the nm scale) which requires efficient, high quality materials [7,8,9].

Electroluminescence technology is increasingly popular for commercial and industrial purposes as a more energy-efficient and sustainable system than other light-emitting technologies. Although electroluminescent (EL) systems usually emit less light than incandescent or phosphorescent bulbs, which makes them less suitable to be the principal source

of light in a room, they are leading the way for flat panel lighting displays (e.g. safety warnings, advertising). Research and development in EL systems is driven by their potential for significant advantages on other display technologies [10]. Their methods of fabrication can be quick and simple, such as the screen-printing process [11] used in this study, and can reduce the manufacturing costs. Also EL systems can display higher contrasts in the light emitted, which enables the technology to perform well in dark or bright environments.

Thin-film electroluminescent devices (TFED) are also an emerging technology that can be used for different purposes in the future, for which $BaTiO_3$ would be very well suited to. The combination of solar cells and TFEDs are a new and promising field of research that could revolutionize the industry with a durable system that is independent from conventional sources of energy.

1.3 Description of the Presented Research

This project's main objective is the synthesis of $BaTiO_3$ nanoparticles of a controlled size and structure for the improvement of an electroluminescent application device (EAD), developed by a collaborator, Professor W. J. Pietro (York University). The EAD consists of: a conductive plastic substrate, a zinc sulfide light-emitting layer, a dielectric layer and a conductive silver layer. Our barium titanate film acts as an insulating-dielectric layer that covers the light-emitting layer. This device requires $BaTiO_3$ particles that have a better dielectric constant, are more homogenous and are smaller than the currently used commercial particles (on average 0.5 μm in diameter). The higher the dielectric constant, the lower is the amount of energy required for the EAD to function with the same efficiency.

Two methods were used to synthesise the nanoparticles. One enabled the adjustment of the particles' size depending on the concentration of one chemical component, and the second consisted in doping the $BaTiO_3$ with lanthanum to increase its relative permittivity. The particles' morphology and composition could be observed with scanning electron microscopy (SEM) and X-ray Diffraction (XRD), respectively. The resulting powder product was afterwards mixed with an epoxy resin to create dielectric inks. Two other inks were used, a luminescent ink made with a ZnS fine powder and a silver-based conductive one, both acquired commercially. Two different kinds of samples were made: the first series was prepared without a phosphor layer to facilitate the measurement of the dielectric permittivity of our $BaTiO_3$, while the second series consisted of the full EAD to test the luminescence and hence the general efficiency of the dielectric particles. Though a few of our samples were made with a commercial printer, most of the final samples were made manually, one layer at a time, by using a screen-printing technique. We calculated the relative permittivity of the layer by measuring its capacitance given by impedance spectroscopy, and its thickness obtained by using a profilometer.

Various challenges arose during this project. A common problem with the synthesis of the particles was the creation of barium carbonate ($BaCO_3$) in the samples during the synthesis and processing of the samples. Boiling the water used for the preparation of the solutions and applying a flow of argon in order to decarbonise it, significantly reduced the amount of $BaCO_3$ in the final product. The screen-printing, which is done manually, required much practice before the samples could be prepared due to the small amount of powder available from each synthesis. Hence, the printing had to be done in an efficient and reproducible manner to minimize losses.

1.4 Thesis Structure

This thesis is divided into five chapters. Chapter One introduces the important concepts behind this research and its objectives. Chapter Two outlines the theories that were the basis for the research as well as previous work done on $BaTiO_3$ nanoparticles and the dielectric properties of this material. In that chapter, the major theoretical concepts related to this work are explored, such as: $BaTiO_3$ structures and properties, scanning electron microscopy (SEM), X-ray diffraction (XRD) analysis, X-ray photoelectron spectroscopy (XPS), profilometry, impedance spectroscopy, electroluminescence and photometry. Chapter Three will describe the various experimental techniques that were used, such as: the two protocols according to which the particles were synthesized, the characterization methods with SEM and XRD, the printing process (once the particles were made), the measurement of the thickness of the printed samples by profilometry, the hardware and software needed for the impedance spectroscopy, the device used for photometry and the calculations that followed. Chapter Four shows the data from all the measurements and the results of the calculations, comparing the dielectric proficiency of the different samples. This chapter discusses the results and puts them into perspective with respect to previous work and the performance of the commercially available $BaTiO_3$. The fifth and final chapter is a conclusion that summarizes this research project and offers suggestions for future work that could further advance this field of research.

Chapter 2 : Theory and Background

2.1 : Previous Work

As introduced in the previous chapter, barium titanate has been recognized as an important material for dielectric purposes since the Second World War. However, it was not only seen as having great potential for capacitive applications, but also as the first piezoelectric ceramic candidate [12]. This last path was short-lived as $BaTiO_3$ was quickly replaced by zinc oxide (ZnO), which was found to be much more efficient for piezoelectric applications. To date, barium titanate still maintains its status as a great dielectric and researchers continue to optimize the various variables affecting its relative permittivity. The effect of the size of the particles in ceramic state was studied in 1975 [13]. It was demonstrated that the dielectric constant increased significantly as the size decreased – although without ever going under a micrometer in diameter.

The effects of doping on barium titanate's electric properties have been studied for a long time. Rare-earth elements, such as lanthanum or europium, are usually an interesting choice of dopant to lightly modify the crystal structure and improve the electric properties. A study doped $BaTiO_3$ with lanthanum by using the Pechini resin method. This showed a significant increase of the dielectric constant compared to pure $BaTiO_3$ [14]. The measurements were done on highly compressed pellets of fine powder sintered at 1300°C. They showed a relative permittivity of over 5500 for a 0.5% Lan doped barium titanate. Electronic properties of such materials have been frequently measured by compressing the powder into pellets, which makes it easy to affix the contact electrodes to their surfaces. It has also been demonstrated that the addition of lanthanum to barium titanate is easily done through the advantageous sol-gel process of synthesis [15].

The crystal structure of $BaTiO_3$ nanoparticles is difficult to define precisely because of the variations in phase depending on temperature and particle size. This has lead some groups to speculate about the possibility of a core-shell structure containing cubic and tetragonal phases. A first definite proof of this hypothesis was brought forward by S. Aoyagi *et al.* [16] in 2005, by using high-energy synchrotron radiation powder diffraction. The identified structure consisted of a tetragonal core with a cubic shell of ca. 8 nm in thickness regardless of the particle size (16 to 300 nm in diameter).

The literature on the subject makes it clear that particles between 70 and 100 nm show the highest dielectric constant [17]. Hence, one of the main objective of this project was to compare their behavior with the 500 ± 100 nm particles, typically produced and used commercially. It was also decided that a sol-gel method would be an efficient way to prepare the samples as the protocol can be fine-tuned to permit the adjustments of particle size and the addition of a dopant to the material.

The process of screen-printing is a very old technique that goes back centuries. It is, however, still useful for commercial and academic applications. In 2002, Stojanovic *et al.* reported the use of screen-printing to make barium titanate thick-films and study their dielectric properties [11]. They obtained a uniform film without any secondary phases with relative dielectric constants ranging from 500 to 2600 at the material's Curie temperature. A similar process was also employed with barium strontium titanate by Tick *et al.*, using low-temperature sintering [18]. This showed the great potential of printed $BaTiO_3$ for multilayered dielectrics and other printed systems such as electroluminescent devices.

2.2 Barium Titanate

2.2.1 Structure and Properties

Barium titanate adopts a crystal structure with a cubic or tetragonal symmetry at room temperature. The unit cell consists of a Ba atom at its origin (0, 0, 0), a Ti atom at its center (1/2, 1/2, 1/2) and three O atoms occupying face centered (1/2, 1/2, 0) (0, 1/2, 1/2) (1/2, 0, 1/2) sites. This creates six bonds between the Ti^{4+} atom and the six O^{2-} surrounding it. Although it has been studied thoroughly, there is no clear consensus on the cubic lattice constant of $BaTiO_3$. Theoretical calculations gave values between 3.94 and 4.03 Å [19] through different methods of computation. In its bulk form, $BaTiO_3$ is cubic above its Curie Temperature (T_C = 120 °C) and tetragonal below it. However studies showed that its tetragonality – the ratio between lattice parameters a and c – is affected by the size of the particles [20, 21]. $BaTiO_3$ can have a cubic structure for particles around 100 nm, but tetragonality will quickly increase in slightly larger particles (tetragonality above 1,01 for 600nm particles) and continue as an asymptotic curve [16]. The tetragonality is also affected by the concentration of a donor dopant and it has been found that it will slightly decrease as the lanthanum doping concentration increases in barium titanate [14]. The band structure of un-doped barium titanate shows the large band gap that is responsible for the insulating properties of the material. It has been verified experimentally [19] and by theoretical calculations [19, 22] that the optical band gap is typically equal to 3.2 eV, see **Figure 2.1**.

As mentioned earlier, the most appealing characteristic of $BaTiO_3$ is its high dielectric constant. With its perovskite structure, $BaTiO_3$ offers a good range of displacement for the Ti^{4+} cation relative to the O^{2-} ions, which gives rise to spontaneous polarization [23]. When a voltage is applied, the positive Ti^{4+} atom is attracted to the negative plate and the negative O^{2-} are

attracted to the positive plate, which creates a dipole moment. The Ti^{4+} ion is displaced relatively to the O^{2-} octahedral enclosure. This dipole electric field vector at the opposite direction of the capacitor's electric field vector enables more charges q to accumulate on the plates for a same voltage V to compensate for the total lower electric field. The capacitance C can be defined through this :

$$C = \frac{q}{V} \tag{2.1}$$

C is also directly proportional to the material's dielectric constant ε_r which dictates the amplitude of the dipole moment.

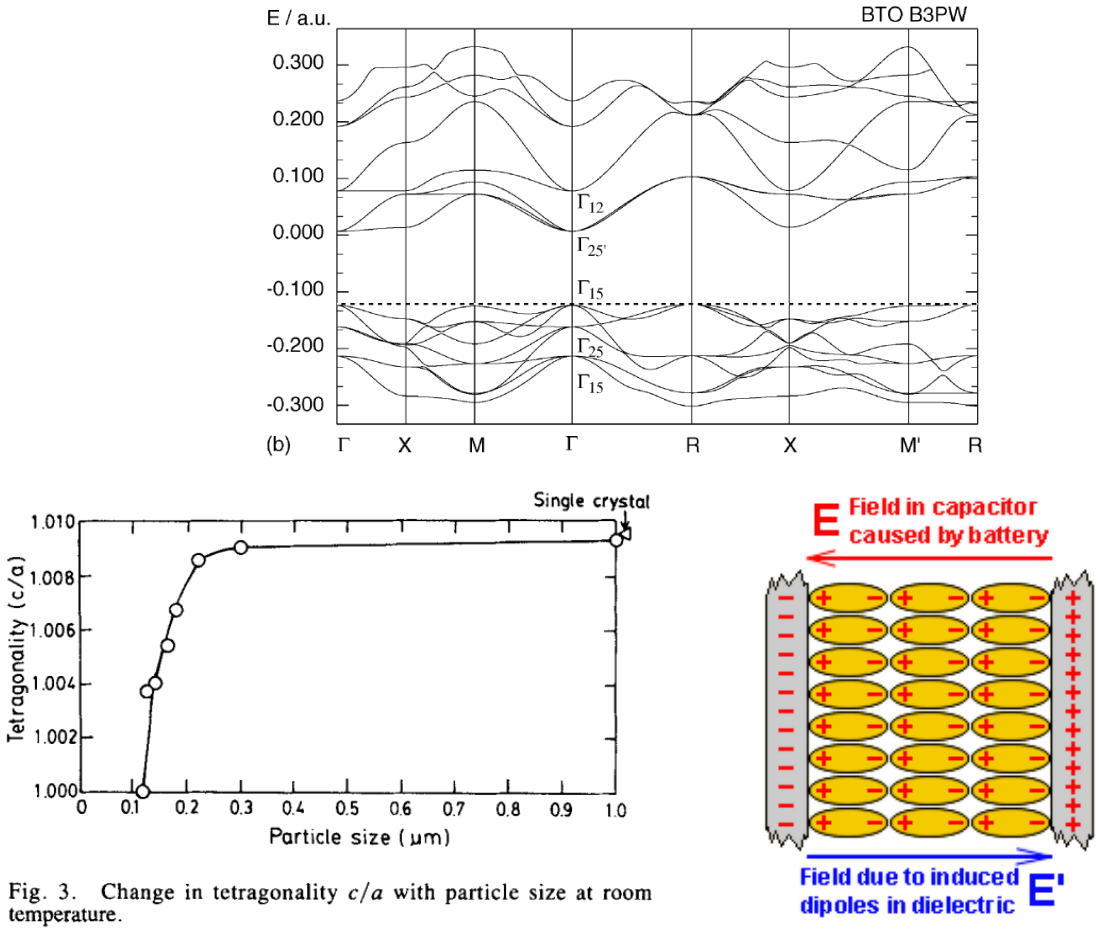

Figure 2.1 : (A) The calculated band structure of cubic $BaTiO_3$, where the energy units are Hartree. [23] (B) Change in tetragonality according to particle size. [20] (C) Electric fields created in the capacitor by the dielectric dipoles and charges on the conductor plates [23B]

It has been shown frequently that the modification of barium titanate ceramic can yield significant improvements to the dielectric and ferroelectric properties of the material [24], [25] and could potentially create nonlinear properties on the surface [26].

2.2.2 Synthesis

A common way to create homogeneous and solid ceramic-type materials is the sol-gel process [15]. This method enables the creation of ceramics in a solution at room temperature when they would usually be synthesized at high temperature. This method is also known to yield some of the biggest specific surface areas due to the resulting smaller particles. A standard definition of sol-gel is as follows [28] :

A solution (sol) is prepared by bonding carbon or a metal (titanium in this project) bonded to an organic oxide as a precursor $M(OR)_n$. Water is added to this solution in order to initiate a polymerization hydrolysis. This will form a compound $M(OH)_n$ because one of the water's H^+ takes the place of the organic compound R which in turn bonds with the remaining OH to, most commonly, become an alcohol. When the hydrolysis is complete, a base is added to the solution to promote condensation and obtain an MO_n ceramic. The hydrolysis/condensation reaction can occur very easily when any amount of water is present, even the humidity in the air can activate the reaction in a small amount of time.

These M-O-M-O-M-(...) bonds are very strong and only break at a temperature above 1000°C. It is important to note that no heat was ever applied to the solution to obtain this product. This is one of the greatest advantages of the sol-gel method. The nucleation of ceramic starts after the condensation reaction and particles slowly grow from these nucleation points. As more particles are created, they collide at an increased frequency and can combine so that it

becomes more energetically favorable to grow connecting "necks". These necks are superimposed bonded particles that create a large network, which finally fills the whole container and can solidify when the density is high enough. The solution would then formed a gel. The product is then washed, dried and ground before a heat treatment burns the remaining organic compounds and breaks the necks' weaker bonds to obtain non-agglomerated nanoparticles.

In this project, the metal organic precursor is titanium isopropoxide, specifically tetraisopropoxide $Ti\{OCH(CH_3)_2\}_4 \rightarrow Ti(OR)_4$, mixed in an ethanol solution and with a small amount of acetylacetone (acac) as a ligant that helps to control the size and the homogeneity of the particles as well as limiting the aggregation [29]. Instead of using pure water for the hydrolysis, we used a solution of barium acetate salt in water. When adding the aqueous solution to the metal precursor, the barium bonds with the titanium during the hydrolysis an forms $BaTi(OH)_3$. The condensation reaction removes an H^+ from the molecule, leaving behind the barium titanate ceramic $BaTiO_3$. When the process begins, the acetylacetone needs to bond with two orbitals, which would be difficult with the large barium atom that would have very distant orbitals. The acac thus coordinates with the titanium as the atom is much smaller than barium and has a much higher electronegativity.

2.3 Electron Microscopy

2.3.1 Scanning Electron Microscopy

Two major advances in Physics opened the door to scanning electron microscopy : First is the introduction of the concept of the wave-particle duality by De Broglie around 1924, which associates a wavelength to a moving particle and paved the way for the field of optics with electron waves. The second, which occurred during the same period, the study of trajectories of charged particles in electromagnetic fields by Busch. He compared these EM fields to lenses, for particles, creating the concept of geometrical electron optics [36]. Optical microscopes use white light that theoretically has a resolution limit of 250 nm. To observe smaller objects, electrons were chosen for their much smaller wavelength following De Broglie's principle, with a resolution down to 1 nm.

The SEM scans the sample with a focused beam of electrons that interact with the surface. The electron beam usually has an energy ranging from 5 keV to 40 keV. This produces various ejected electrons or X-ray photons, see **Figure 2.2**, all of which can be captured with different detectors. The secondary electrons and backscattering electrons are the main signals used to create a clear image of the sample.

A frequent problem that occurs with non-conductive samples is the accumulation of charges that can't be dispersed on the material [32]. This 'charging' blurs the image of the detector and once this happens in the microscope, it is irreversible. To avoid this problem, gold is deposited on the insulating material to prevent the accumulation of electrons.

2.3.2 Energy Dispersive X-ray

EDX generates an X-ray spectrum of the material currently under observation in an SEM. The microscope's electron beam is used to transmit a sufficient amount of energy to an electron of lower energy, to expulse it from the atom, leaving a hole on that energy level. A higher-level electron will then fill the hole, releasing the difference in energy in the form of electromagnetic waves, X-ray in this case [33]. The excess of energy can also be transferred to another electron that is expelled from the atom and becomes an *Auger electron*. Auger spectroscopy is a whole field in itself and is very useful for chemical analysis, but was not necessary in this project.

The energy difference between the electron shells is characteristic to each atom and thus the EDX can give a clear picture of the elemental composition of the substance. One of the major constraints for this useful tool is the ± 15% error for a rough surface or particles without a standard [34], which is the case in this project.

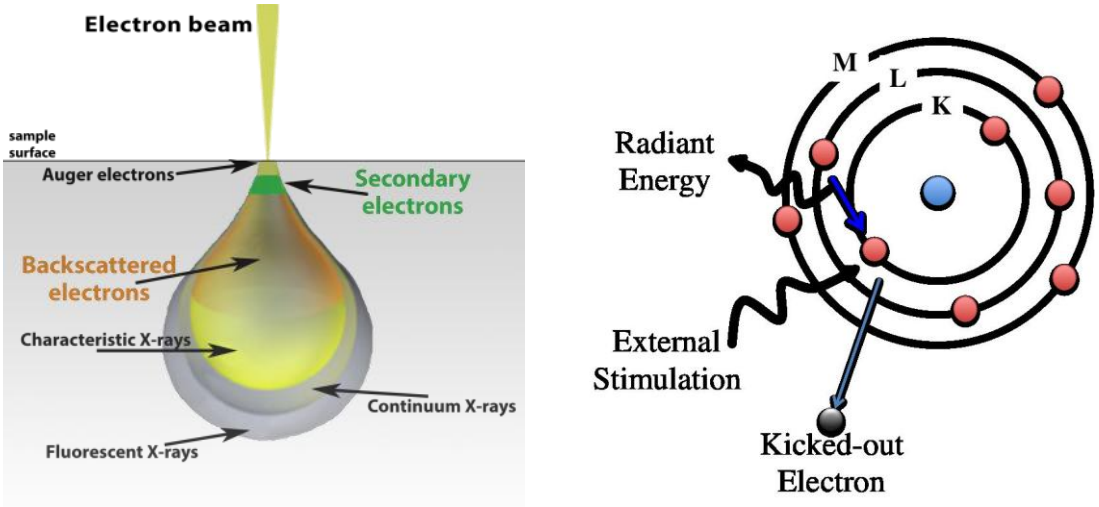

Figure 2.2 : (A) Signals created by the electron beam colliding with the sample. (B) Process of X-ray radiation from electron shell transition [34B]

2.4 X-ray Diffraction

Commonly used for research and medical diagnoses since the beginning of the 20th century, X-rays have been an essential probing tool for the advancement of science. In crystallography, diffraction measurements have given way to a simple method of analysis which permits the determination of any unknown crystalline powder at hand. Quantification of the amount of crystalline phases in a material has been made possible, especially through the Rietveld method [35], which allows an in-depth look at its structure and properties, but the practice is yet to be considered fully reliable throughout the scientific community.

For a cubic or tetragonal unit cell, the main characterization tool for crystal structures is the group of Miller indices (h, k, l) [36]. The combination of three values (h, k, l) indicates the orientation of the lattice planes. All parallel planes of the structure are separated by a distance d_{hkl}. This distance is directly correlated to the lattice constant *a* :

$$d_{hkl} = \frac{a}{\sqrt{h^2 + k^2 + l^2}} \tag{2.2}$$

When an incident electromagnetic wave is reflected by parallel planes in the crystal, the resulting beams can only be observed if they are interfering constructively. **Figure 2.3** represents this principle that was introduced by W.L. Bragg, and gave this relationship :

$$2d_{hkl} \sin\theta = n\lambda \tag{2.3}$$

n : any integer number
λ : Wavelength of incident beam

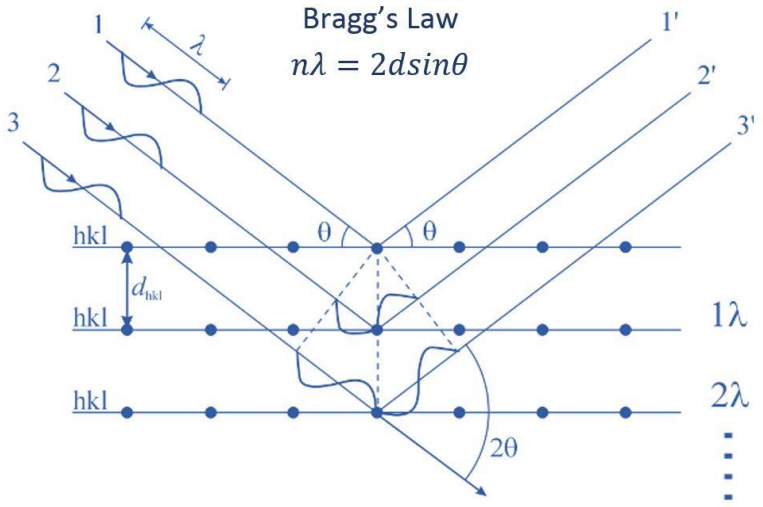

Figure 2.3 : Diffraction of X-rays on periodic lattice planes representing Bragg's law [36B]

Bragg's law - where *n* is any integer number, λ the wavelength of the incident beam, θ the angle of the same beam relative to the lattice planes, *d* the distances between the (h, k, l) planes - determines the nature of the electromagnetic wave that needs to be used for crystal structure analysis. Because of the $sin\theta$, the beam's wavelength is restricted to $\lambda \leq 2d_{hkl}$. The average lattice constant is between 2 and 9 Å, which means the photons used for diffraction are in the X-ray range of the EM spectrum.

The data obtained from the X-ray analysis of a crystal is usually presented in the form of a graph that shows the intensity (number of counts) of peaks in relation to the Bragg angle, 2θ. With each peak related to a specific combination of the indices h, k and l, the array obtained is always unique to each material structure and gives a clear picture of what the studied substance is made of, see **Figure 2.4** for a barium titanate spectrum [37]. When composed of more than one type of crystal lattice, especially with close phases such as tetragonal or cubic, determination of the structure can be challenging. A specialized method of X-Ray diffraction such as using

synchrotron X-ray scattering or advanced analysing techniques like the Rietveld method, can be useful to investigate troublesome cases .

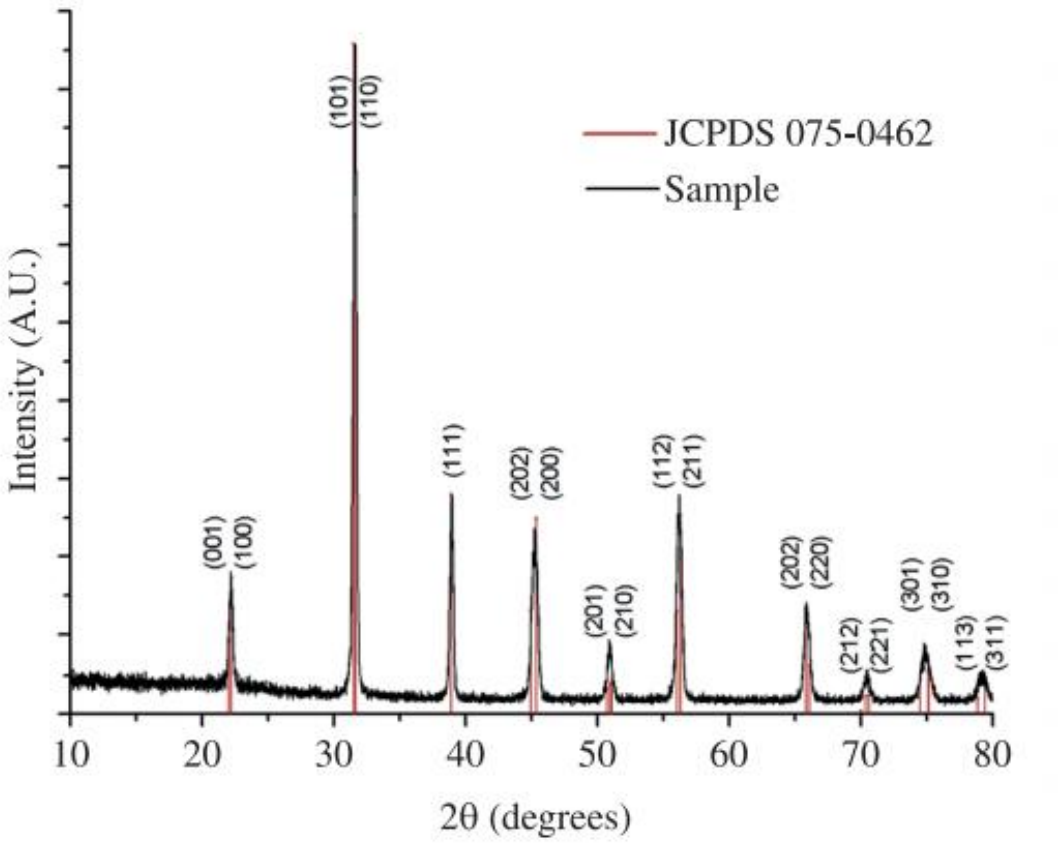

Figure 2.4 : X-ray spectrum of barium titanate with designated (hkl) coordinates for each peak. Red lines are reference peaks of cubic $BaTiO_3$. [32]

2.5 X-Ray Photoelectron Spectroscopy

Almost forty years ago, the practice of X-ray photoelectron spectroscopy (XPS) became common in the scientific community as an alternative way to analyze the surface composition of materials, probing a deeper range of electronic energies than before [38].

The XPS apparatus emits X-Ray photons from a range of energies, typically from 100 to 1200 eV. An X-ray photon at the right frequency interacts – mainly on the surface of the material – with an electron from a particular orbital shell and expulses it from the atom with a kinetic energy E_k. The emitted electron is captured by the spectrometer receptor and its E_k is measured to calculate the binding energy E_B using the following relationship :

$$E_k = h\upsilon - E_B - E_R - \varphi - \delta E \qquad (2.4)$$

The paramater $h\upsilon$ represents the energy of the X-Ray photons established by the Planck-Einstein relation, the frequency υ multiplied by the Planck constant h; E_R is the recoil energy, a very small contribution to the equation (0.1 - 0.01 eV) that comes from the nature of the solid; φ is the work function of the instrument, a correction factor compensating for the loss of energy when the detector absorbs the electron and δE is another correction factor, to counteract the effect of electrostatic charging on the surface [39], mostly important when using non-conductive material such as barium titanate.

An element's electrons in different orbitals have specific binding energies that can be used to precisely characterize the element with photoelectron spectroscopy. These binding energies slightly vary depending on the compound formed with the element. Therefore, they can be used as benchmarks to determine if a material is pure or if undesired compounds formed during the synthesis process. More specific to our project, the XPS focuses on lanthanum's

binding energies to analyze the doped barium titanate particles. We can see the important XPS peaks obtained by various lanthanum compounds in **Figure 2.5**. The binding energy peak of La3d is split in two because of the spin-orbit interaction, separating $La3d_{5/2}$ and $La3d_{3/2}$, but these two peaks are also split by the possible transfer of an electron from an oxygen atom to the lanthanum's empty electronic orbital 4f. The low binding energy peaks are usually referred to as f^0 (electron not transferred) and the high energy ones as f^1 (electron transferred) [40, 41].

The manipulation and analysis of our powder samples were entirely done by an expert from the Surface Interface Ontario institute on a Thermo Scientific K-Alpha instrument. Therefore, no experimental section will be attributed to the XPS measurements before the results and discussion.

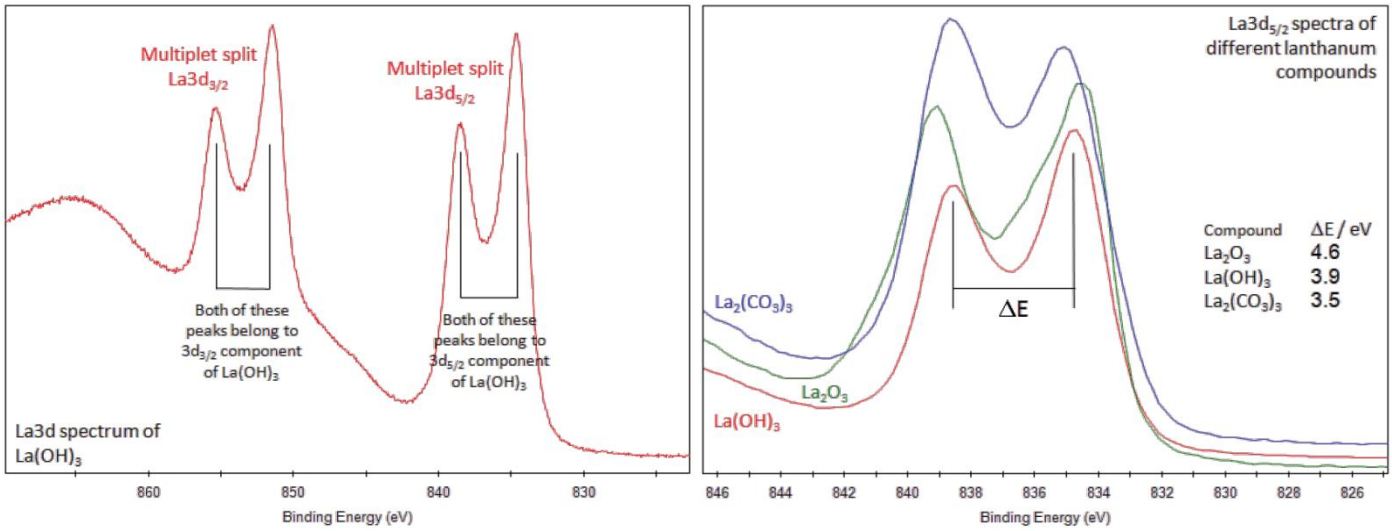

Figure 2.5 : Binding energies peaks of lanthanum compounds. The two multiplet splits of the La3d orbital is the characteristic pattern to look for in the XPS spectrum to confirm the presence of lanthanum. To determine the specific compound, we need to measure the separation between the peaks in the splits. [42]

2.6 Profilometry

The idea of a stylus following a roughness profile of a surface goes all the way back to the invention of the phonograph by Thomas Edison in 1877. Two types of profilometers are used nowadays, optical profilometer, **Figure 2.6** (A), and contact profilometer, **Figure 2.6** (B). Optical profilometers have been developed to eliminate any contact with the surface. They use interference microscopes to measure the height variations on the samples' surfaces. It has the advantages of not altering the sample in any way (except if it is photosensitive) and quickly renders the topology of the surface [41]. However, to obtain a signal the samples must be reflective. Contact profilometers use a stylus to probe the surface through either a tapping or a continuous scanning mode. The movements of the stylus on the surface can damage the sample when too much pressure is applied. This process takes more time but the data acquired is usually more reliable than that obtained with an optical profilometer [44].

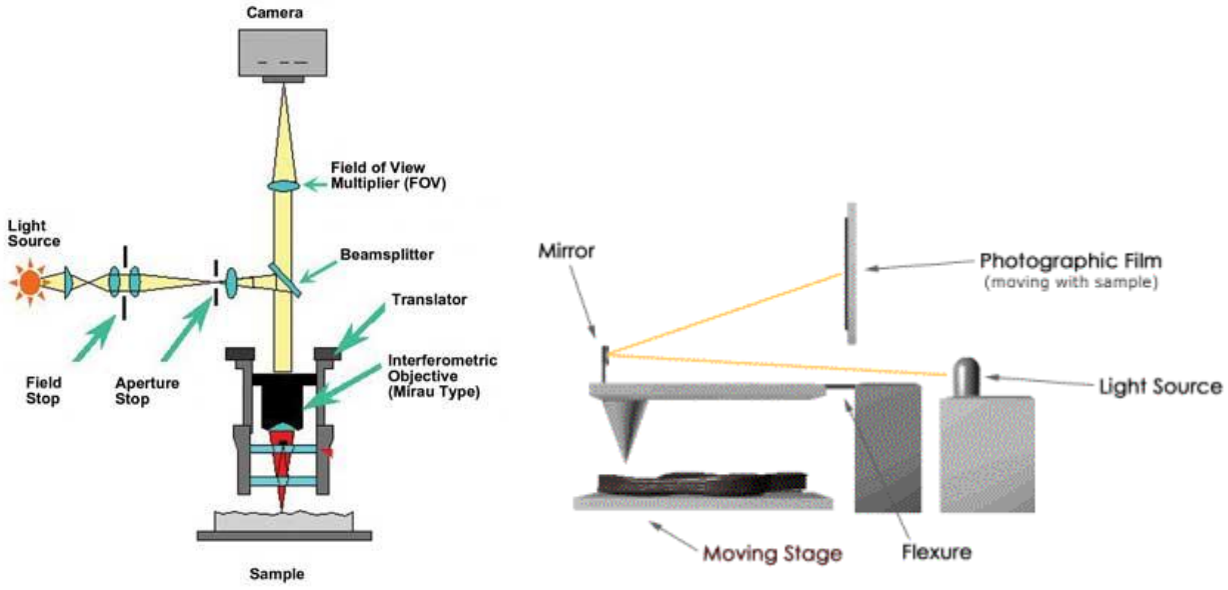

Figure 2.6 : (A) Optical profilometer schematic, measuring the distance with an apparatus similar to a Michelson Morley interferometer [45]. (B) Stylus profilometer with mechanical contact and laser source to determine the height variations [46]

2.7 Impedance Spectroscopy

The first theoretical and experimental plotting of the impedance plane was done by Sluyter in 1960, for aqueous electrolytes [47, 48]. Over the last 30 years, impedance spectroscopy has grown to become one of the most robust techniques to analyse reaction mechanisms in solutions and investigate solid and liquid impedance systems [49]. The main complication, when dealing with impedance spectroscopy, is the ambiguity in the interpretation of the results. Hence, it is important to understand what electrical system one is dealing with and find a suitable physical model (equivalent circuit). Theoretically, there is an infinite amount of possible models but we generally want to base our data on the simplest one. The Kramers-Kronig (KK) relations were developed to ensure the coherence of impedance with models. Algorithms were created to ease the application of the relations to raw data and it has now become an essential part of impedance spectroscopy software [50]. KK relations are thus good quantitative tools to verify the chosen model.

Impedance is defined as the current I(t)'s proportional response to an electrical circuit when a voltage V(t) is applied. When a signal $V(t) = V_0\sin(\omega t)$ is applied, the resulting current will have a phase difference θ such as $I(t) = I_0\sin(\omega t + \theta)$, except for a circuit containing uniquely resistive components. This delay is caused by two mechanisms that affect the impedance only in an alternating current, the accumulation of charges on a closely separated conductor (a capacitance, *C*) and the self-induced voltage, going in the opposite direction to the circuit's general V(t), caused by the magnetic field in a conductor coil (an inductance, *L*). These capacitive and inductive elements' interactions with the flow of the circuit is given by these equations :

$$I(t) = C\,\frac{d\,V(t)}{dt} \qquad\qquad V(t) = L\,\frac{d\,I(t)}{dt} \tag{2.5}$$

An increased number of such elements in a system will quickly produce a set of equations too complex to be solved if kept in the differential state. With the use of Fourier Transforms, these relationships are greatly simplified and can be combined in the frequency domain for a large number of elements. I(t) and V(t) become I(j ω) = C*j*ω*j*V(j ω) and V(j ω) = L*j*ω*j*I(j ω), with "j" as the imaginary "i" constant. The voltage-current ratio in the frequency domain is similar to Ohm's law in direct currents :

$$I(j\,\omega) = \frac{V(j\omega)}{Z(j\omega)} \tag{2.6}$$

In impedance spectroscopy, the complex impedance space, also referred to as Nyquist plot, is the essential experimental data to analyze the circuit (see example in **Figure 2.7)**. Every capacitive element in parallel with a resistance adds a semi-circular arc while a resistive element creates a displacement on the real axis. Although there is no frequency information directly on the plot, in the data presented in this thesis the lowest frequency data points always start at the bottom right of the circular curves while the highest frequencies are found near the origin.

The impedance of a circuit RC in parallel, as there is in this project, goes as follows [51] :

$$Z = \frac{1}{\frac{1}{R} + j\omega C} \tag{2.7}$$

Separating the real and imaginary parts to visualize in a Nyquist plot :

$$Z = \frac{R}{1 + j\omega RC} = \frac{R}{1 + (\omega RC)^2} - j\,\frac{\omega R^2 C}{1 + (\omega RC)^2} \tag{2.8}$$

When examining the modulus of the impedance we can predict the general shape of the complex plot :

$$|Z| = \frac{\sqrt{R^2 + (\omega R^2 C)^2}}{1 + (\omega RC)^2} = \frac{R}{\sqrt{1 + (\omega RC)^2}} \tag{2.9}$$

When the frequency goes to infinity the impedance goes to zero because the order of ω is higher in the denominator, and when the frequency goes to zero the impedance becomes real as Z = R . The minimum for the imaginary part is attained when ω = 1/RC, as RC is usually referred to as the time constant of the system. This time constant τ = RC represents the time at which the majority of the charges, percentage N = 1 - e^{-1} = 0.63, are displaced from one end of the capacitor to the other. As this project aimed at studying the dielectric constant of the material, the current is calculated once the impedance data is obtained (from a given voltage function). The system's capacitance is then extracted from the current as seen in the previous equation (2.8). The dielectric constant is directly proportional to the capacitance and is obtained with the physical characteristics of the analyzed sample.

The device's correct equivalent circuit, as seen in **Figure 2.7**, contains an extra resistor outside the parallel system, to represent the contact resistance. The impedance can written as :

$$Z = \frac{R}{1 + j\omega RC} + R_s = \frac{R}{1 + (\omega RC)^2} + R_s - j\,\frac{\omega R^2 C}{1 + (\omega RC)^2} \tag{2.10}$$

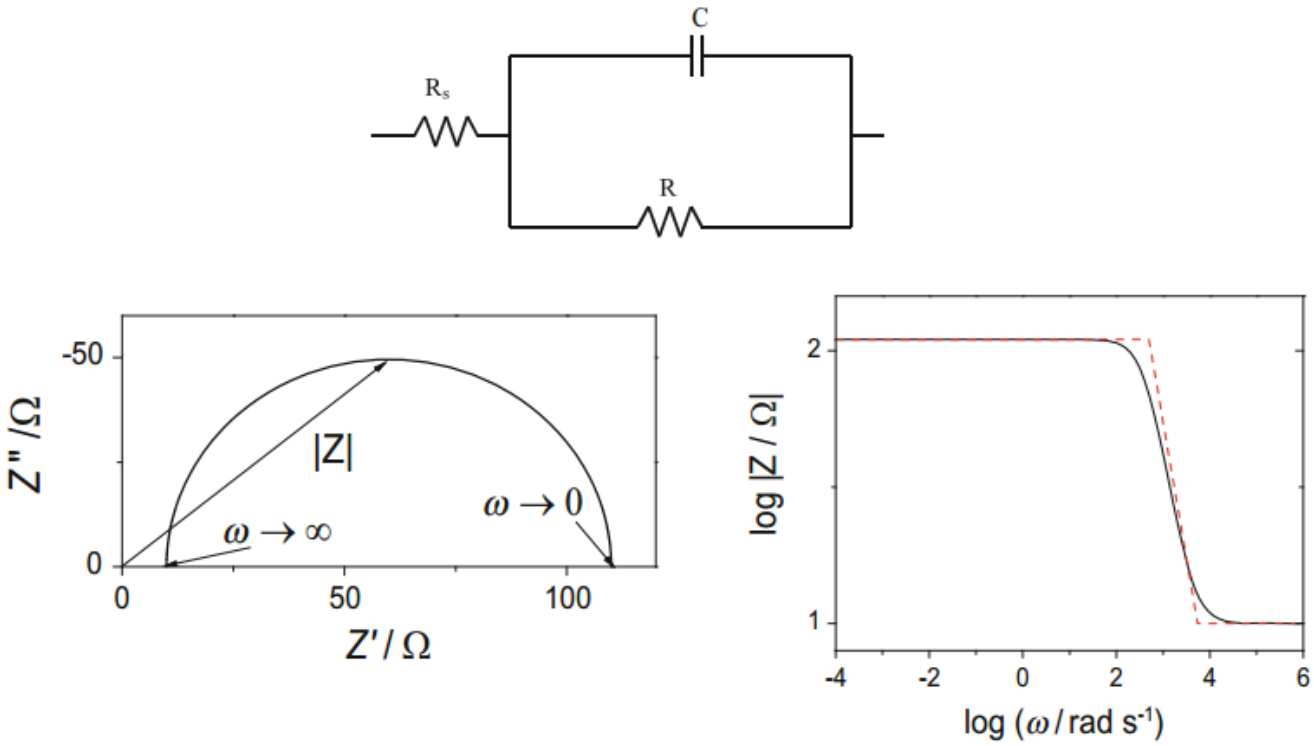

Figure 2.7 : Standard Nyquist plots of impedance (left) with Bode plots (right) with the equivalent circuit used (top) [46]. These plots refer to the equation (2.10) where the added resistance R_S translates the semi-circle on the real axis. The equations (2.8) and (2.9) would generate a semi-circle intersecting at the origin of the plot.

2.8 Electroluminescence and Photometry

There are two common ways to produce light, in the visible spectrum, from a material : incandescence and luminescence. Incandescence refers to light emitted by conductive bodies when a current is applied and the electric resistance of the material causes an increase in temperature. The intensity of light produced follows the black body radiation principle. On the other hand, luminescence is defined as the emission of light by any process other than heat and there are many different types of such phenomena [52]. Chemiluminescence produces light from a chemical reaction, such as the one that occurs in fireflies, or when luminol reacts with iron found in hemoglobin to help forensic scientists detect the presence of blood. A Photoluminescent substance will emit light during a certain amount of time after being illuminated by a primary source of light. For example, most glow-in-the-dark tools and toys use this process. The list of examples is quite long and beyond the scope of this thesis. In this project our objective is to test the efficiency of screen-printed *electroluminescent* devices fabricated using our BaTiO3 nanomaterials. Electroluminescence is the emission of light when an electric field is applied to a substance. The field excites electrons in the material, which subsequently go back to their ground state causing the emission of photons of a specific wavelength depending on the luminescent material. The discovery of this process showed the possibility of converting electric energy directly into light with a low power input making it of high interest for different fields working with luminescence [53].

Electroluminescent devices can be assembled with a minimum of four layers : a conductive layer (contact), a luminescent layer (often phosphor materials), an insulating dielectric layer and a second conductive layer. Four steps occur when light is produced in an electroluminescent device. Firstly, electrons tunnel from electronic states at the insulator-

phosphor interface. Secondly, a high electric field gives kinetic energy to electrons in the phosphor. Acting like a leaky capacitor, the device accumulates charges at the conductive interfaces, which creates the electric field. Thirdly, the accelerated electrons impact the luminescent center, exciting the electrons in the phosphor atoms to higher states of energy. Finally, those electrons relax to their ground state, transposing their lost energy as light. That emission of light can then be measured with a photometer to compare the efficiency of each device.

Photometry can be defined as the science of measuring the intensity of light compared to its human visual response. It is a relatively young science, as it was only in 1924 that the "Commission Internationale de l'Éclairage" decided to document the average human eye's response to light. The collected data, from a large sample group, gave a Gaussian curve that created the standard of photometry for decades. It was found that the human eye's sensitivity changes with the wavelength of the received light. It is most receptive to green light emissions of around 555 nm, **Figure 2.8,** in bright light conditions where the eye's less-sensitive cones are responsible for the vision called *photooptic* [54]. When the light is dimmer, the eye's rods take over and switch to a *scotoptic* vision with the response curve peaking at 507 nm. The lumen is the standard unit for photometry and luminance can be defined as :

$$L = 683 \int_{\lambda_1}^{\lambda_2} P(\lambda) V(\lambda) d\lambda \qquad (2.11)$$

P(λ) is the light power, in Watts, and V(λ) is the relative luminosity coefficient, which only attains unity at 555 nm according to the eye's response in normal conditions. Photometry follows similar laws to electromagnetic wave theory, such as the inversed square and the cosine laws. The inverse square law states that the intensity per unit-area on a given surface is inversely

proportional to the square of the distance between the source and the surface. As for the cosine law, the light intensity on a same surface diminishes as the angle from the normal increases, following a cosine relation.

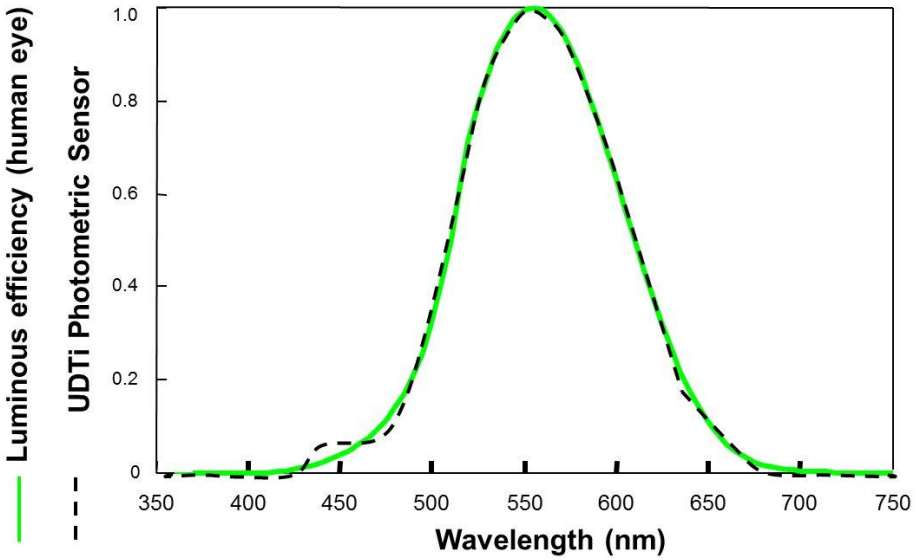

Figure 2.8 : Human visual response to the spectrum of light, compared to a standard photometric sensor. [55]

Chapter 3 : Experimental Techniques

The theory behind the important concepts in this project having been presented, this chapter will describe the manipulations and different instruments used during experimentation. From the creation of $BaTiO_3$ nanoparticles to the acquisition of structural and impedance data and the scientific art of screen-printing, the experimental techniques described here were all essential components in attaining this project's objectives. Several samples of new electroluminescent devices have been made with different $BaTiO_3$ syntheses and the relative permittivity of the perovskite was studied thoroughly through impedance spectroscopy.

3.1 Particles Synthesis Methods

3.1.1 The Sol-Gel Process

The first step in this process, **Figure 3.1**, is to create solutions containing either Ba^{2+} or Ti^{4+} compounds. For the former, barium acetate powder (99% Sigma Aldrich) is dissolved in purified decarbonated water to a 1,165 M concentration. The solid dissolves quite quickly, in about 2 minutes, and to make sure no aggregates are left, the solution goes back and forth between a high-speed stirring and an ultra-sound basin. The Ti^{4+} solution uses ethanol as a solvent, to which titanium isopropoxide and acetylacetone are added, at a volume ratio of 6:3:1, resulting in a light, yellow-colored solution. In this project, the acetylacetone quantity varies between 100%, 71.0% and 49.7% of this initial ratio with the ethanol amount increasing to maintain a constant volume. The Ti^{4+} solution is then added to the Ba^{2+} solution with more ethanol at a specific volume ratio of 2:3:7. The milky-yellow mixture is left stirring vigorously for 24 h. After the aging, KOH (1 M) is slowly added until gelation occurs.

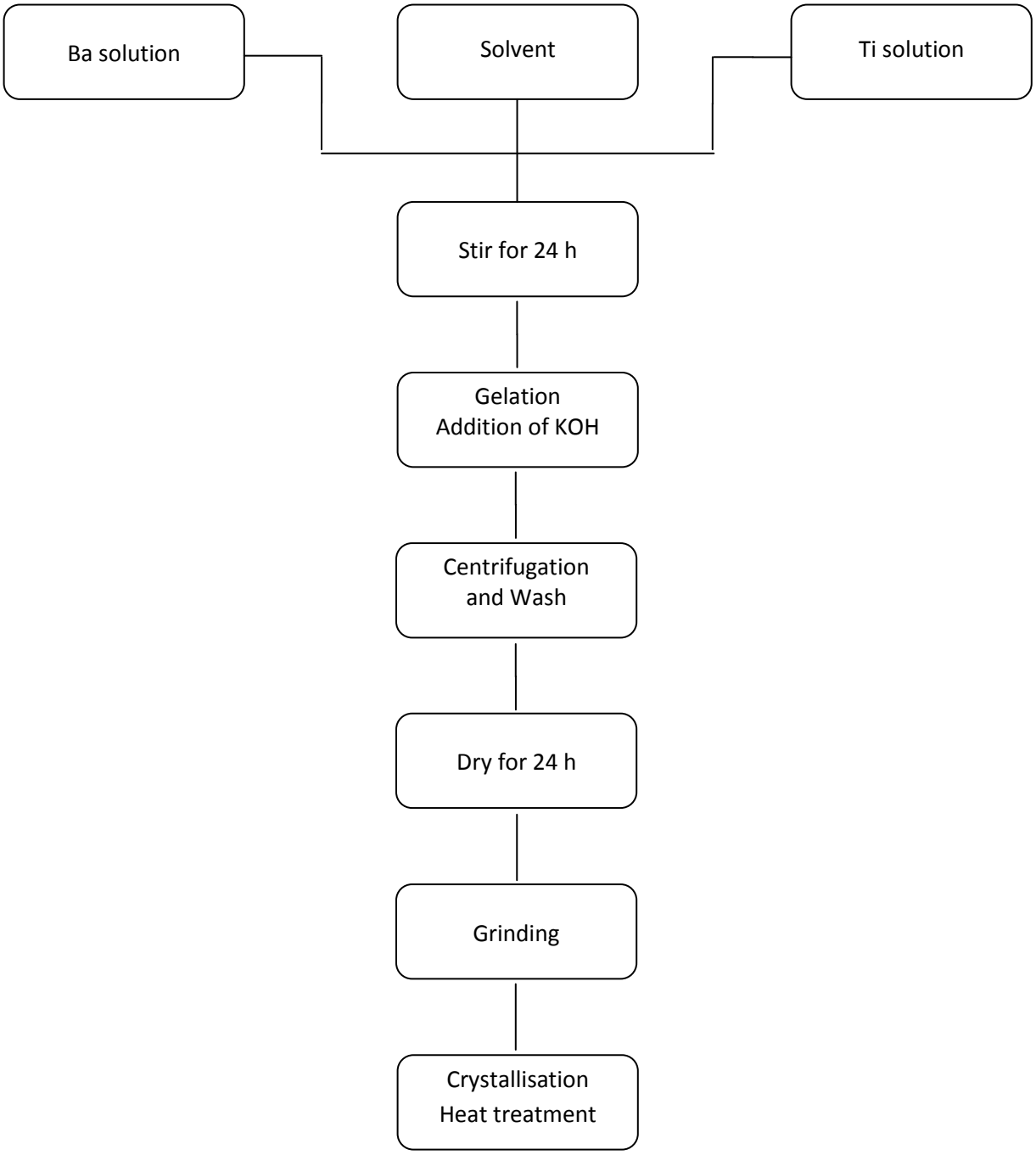

Figure 3.1 : Generic process flowchart for particle synthesis using the sol-gel method.

We add a volume of KOH solution that is ca. 30% the volume of solution to which it is added, and the solution is left unstirred for an hour.

The resulting product is a milky-yellowish dense solution but does not result in the solid gel characteristic of this method of fabrication because of the deliberately large amount of alcohol. This greatly simplifies the next step, which consists in centrifuging the suspension, washing it three times and drying it at a temperature of 80°C for 24 h. Upon drying, the yellowish material shrinks to form an aggregate that is ground carefully in a mortar. The resulting powder is whiter than the dried aggregates. The powder is placed in the furnace at the chosen annealing temperature of 700°C for 4 hours with the temperature increasing at a rate of 3 degrees per minutes until it reaches 800°C and annealed further at 800°C for 2 hours. If the amount of powder is too large, the sample has to stay for a longer time in the furnace. The final powder should be a pure white. It is then ground again to ensure that there are no large aggregates.

3.1.2 The Pechini Resin Process

Similarly to the sol-gel process, this method, **Figure 3.2**, requires the creation of two separate solutions of Ba^{2+} and Ti^{4+}. Both use ethylene glycol and citric acid in which either the barium acetate or the titanium isopropoxide is dissolved. For every 10g of barium acetate (the equivalent for 1.188 mL of titanium isoproxide in the second solution), 35.02 mL of ethylene glycol is used with 400.0 mL of 1 M citric acid solution, in purified water. This dissolution takes longer than in the sol-gel process but, as in the sol-gel process, any solid needs to be fully dissolved before moving to the next step. The two clear solutions are then mixed, resulting in a pale-yellow solution and, as the stirring occurs, the dopant, lanthanum nitrate hexahydrade, is

added (exact amounts are added to yield 0.3%, 0.5% and 0.7% mol of La based on the number of moles of Ba^{2+}).

The formation of the resin, or esterification, occurs during the first thermal treatment at low temperature, 140 °C. The liquid slowly decreases in volume turning a dark orange colour and becomes very viscous. This process takes between 10 and 20 hours depending on the size of the synthesis. After this stage, the material is treated at 250 °C for an hour and at 300 °C for four hours to decompose the resin, creating a low-density black solid, visually similar to hard foam. The solid needs to be pulverized in a mortar. Even though it is very porous it is still quite hard. A small aluminium container was specifically made to crush larger pieces of the material, thus accelerating the grinding process (**Figure 3.2.A**). The fine precursor powder can then be treated in the furnace for a last time at 500 °C for 4 hours, 700 °C for 4 hours and 800 °C for 2 hours (minimum required times given). During the heat treatment, the powder goes from a black-brown to a pure white colour (**Figure 3.2.B**), which is expected for $BaTiO_3$.

During the process, a large amount of $BaCO_3$ was created due to the inability of the samples to evacuate the entirety of the carbon thus preventing some Ba^{2+} ions from forming $BaTiO_3$. It was later found that a flow of O_2 during the last thermal treatment would have helped with the preparation of pure $BaTiO_3$.

Figure 3.2 : (A) Aluminium container and lid used with a hammer to crush large pieces of decomposed pechini resin. (B) Transformation of the powder before (right) and after (left) thermal treatment.

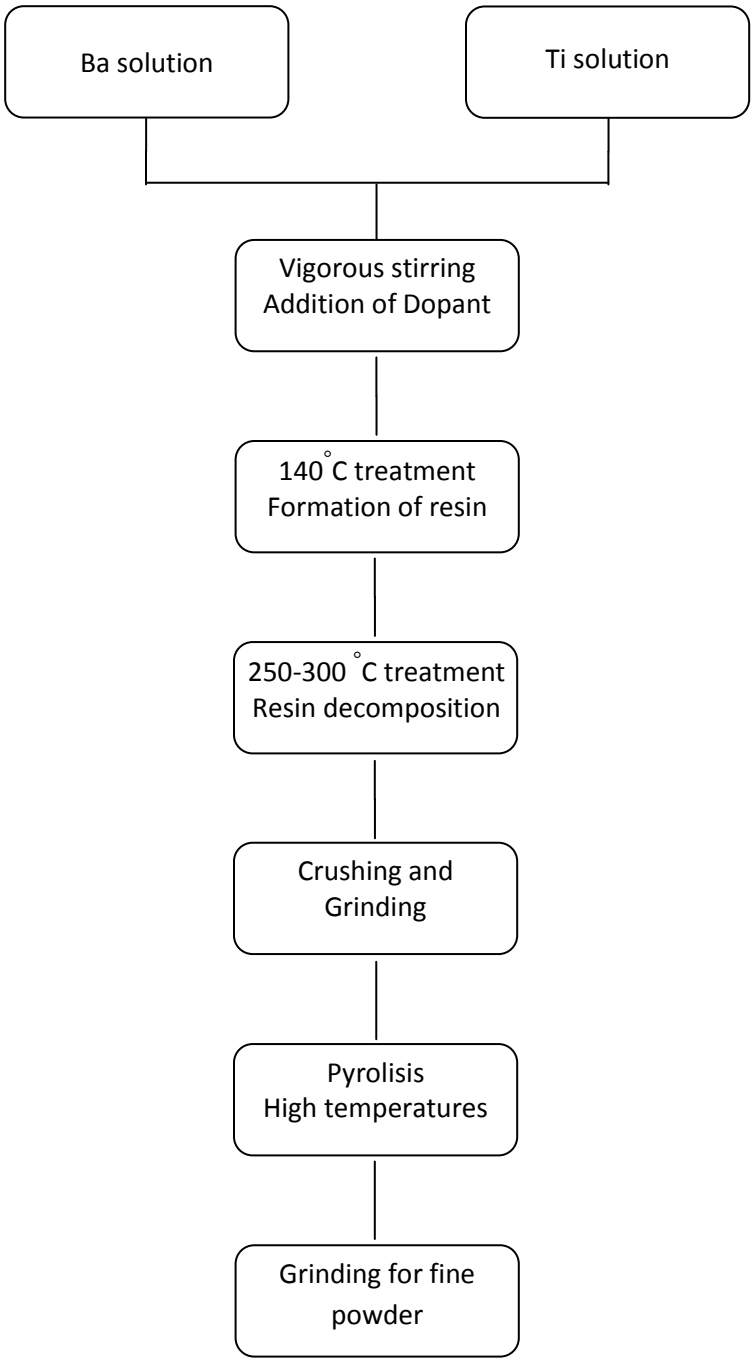

Figure 3.3 : Generic process flowchart for particle synthesis using the Pechini resin method.

3.1.3 Acetic Acid Purification Tests

Chapter 4 will show the results of the $BaTiO_3$ fabrication attempts and the problems that occurred with the $BaCO_3$ contaminations. To verify the possibility of purifying the samples, tests with acetic acid were done. The acid added to the powder is expected to react with the carbonate in the $BaCO_3$ compound, extracting it to create CO_2 and the free Ba^{2+} ions can then be recombined to form more $BaTiO_3$. The purification is visible due to the formation of CO_2 gas bubbles during the reaction. When the bubbling stops in the presence of excess acetic acid, one can assume that most carbonate has reacted. The powder is then washed repeatedly with ethanol, dried and can be used to do further characterization.

EDX analysis was done to study the relative concentration of carbonate and titanate of acetic acid treated and untreated samples. The results showed some decrease in $BaCO_3$ concentration but no complete purification using this method. It was thus decided to concentrate our efforts on preventing the formation of barium carbonate during the synthesis as much as possible instead of trying to get rid of it afterwards with the acetic acid, a method that resulted in significant material losses.

3.2 Characterization Methods

3.2.1 Scanning Electron Microscope (SEM)

The $BaTiO_3$ particles were prepared for SEM observation by spin-coating on a small glass substrate. A very small amount of powder was dissolved in ethanol (about 0.02g/mL). This process did not need to have precisely the same concentration every time as it was purely for observational purposes. It was found that this concentration gives a good amount of monodispersed particles on the surface with few particle agglomerations. For the SEM sample

preparation, three drops of the solutions were used for each sample; the substrate was spinning at 1000 rotations/min for 5 seconds and 3000 rounds/min for 50 seconds between each drop. Every sample was taped (with carbon tape) on the aluminum support in the SEM. The microscope used is a Hitachi S-520A.

3.2.1.1 Morphology and Size Observation

Spin-coated samples were also coated with a minimal amount of gold particles to facilitate the electron microscope observation since barium titanate is non-conductive. When the supports are placed inside the microscope, the door is closed and air is pumped out of the chamber to create a vacuum. For our observations, the microscope chamber was at high vacuum and the electron beam energy used was of 5 keV. The image obtained with the microscope is first calibrated by an automated calculation of the distance between the samples and the detector, followed by an adjustment of the brightness and a *coarse* focus to make the surface of the support and the material of interest visible. For every magnification, a *fine* focus is done and we verify that there is no astigmatism to get a crisper image of the particles. At a magnification of 75 000 x, we can distinguish particles and most pictures taken for size analysis were taken at that magnification or slightly higher. Because of the nature of the material, it is difficult to have clear images at high magnification such as 125 000 x, but we can nevertheless observe the small particles seemingly forming the 100nm range particles (as discuss in chapter 4) and their morphology indicative of the barium titanate's crystal structure.

3.2.1.2 Energy Dispersive X-ray (EDX) Spectroscopy

Energy dispersive X-ray measurements can also be performed in the SEM. This is a quick and effective tool to analyse the chemical composition of the observed samples. Instead of

using finely spread particles on a glass substrate, a small amount of the dielectric powder is directly deposited on the carbon tape. The high concentration of particles facilitate the EDX measurements. However when inspecting the data it is important to consider that the presence of more intense carbon peaks is possibility because of the tape.

3.2.2 X-Ray Diffraction

The X-ray diffraction measurements were acquired using an AXS D8 Discovery Microdiffraction system with Cu kα point-focus x-ray source operating at 40 kV and 40 mA. The experimental data was collected on frames with an exposure time of 400-480s that cover a 2-θ range of 20^{o}-70^{o}. The diffraction peaks diagram obtained has a resolution of 0.005^{o} 2-θ. For some of the samples, the data were acquired with a Siemens D5000, an older model, using the same acquisition settings. We can see in **Figure 3.4** a spectrum acquired from a $BaTiO_3$ powder using this instrument, with the intensity of the diffraction peaks given as a function of the 2θ angle.

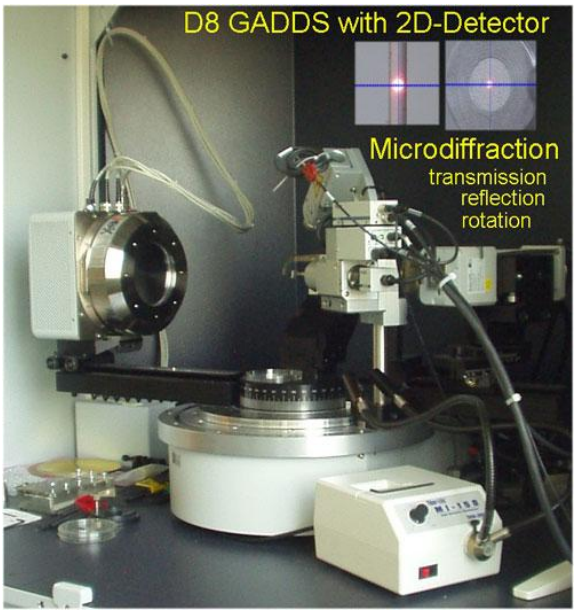

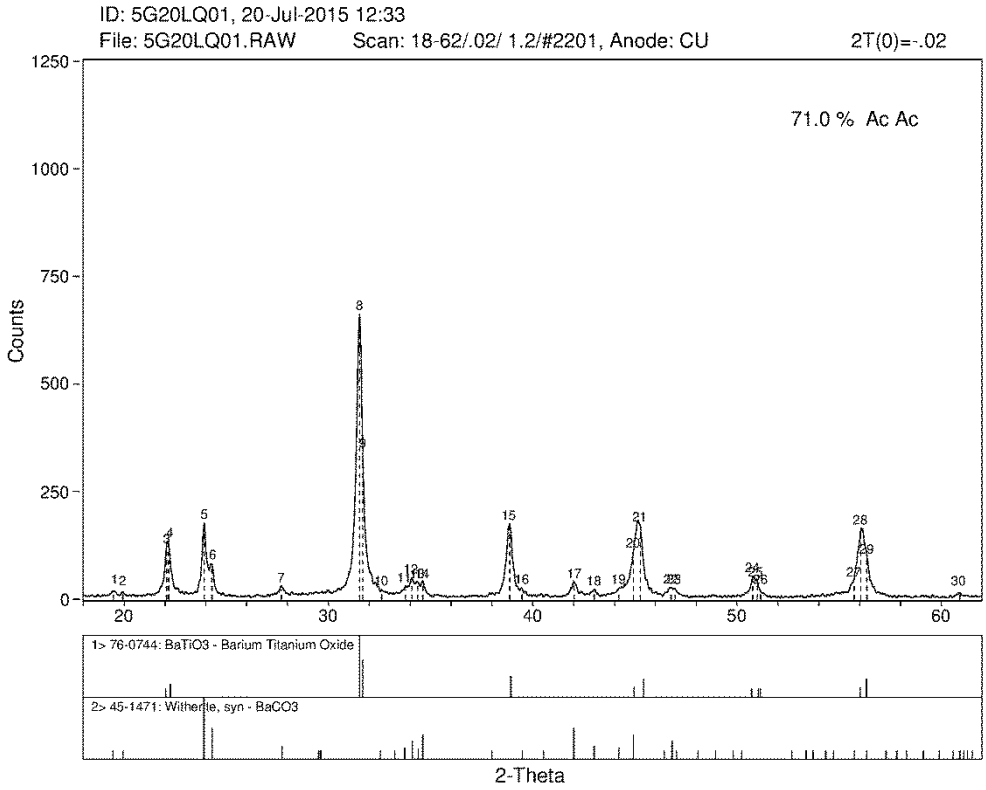

Figure 3.4 : (A) Diffractometer D8 University of Toronto (B) Diffractometer D5000 Université Laval (C) Example of peak spectrum for $BaTiO_3$ powder (71.0% acac)

3.3 Screen-Printing

The first printed samples were done with an industrial printer at the company Scobil inc. for a side-to-side comparison with the commercial barium titanate used in the electroluminescent device and our experimental ones. Although the product obtained was of good quality, the process demanded a very large amount of ink, and thus dielectric powder, to get started. The squeegee of the instrument is very large and needs to be completely covered with ink before the actual printing, even if the samples were small, about 2,83 cm^2. This wasted too much of our powder, and a manual screen-printing device was installed in a laboratory at York University.

3.3.1 Set-up

The main component of our manual printer is a screen that has three cut-outs in the blue, impermeable mask for each of the three layers of the electroluminescent device. These stencils are separated by the necessary distances to prevent the ink from overflowing from one stencil to the next during the printing. The screened ink passes through a mesh count of 130, meaning 130 openings per inch. This gives openings of 124 µm given the thread diameter of about 71 µm.

A small hand vacuum was purchased to create the suction necessary to hold the indium tin oxide (ITO) plastic surface down during the printing process. After some difficulties with the samples sticking to the screen even with the vacuum, especially when thicker silver ink were used, the borders of the ITO plastic was also taped to the base of the apparatus. The use of vacuum and tape were quite effective, as the tape alone cannot hold the center of the samples in place, **Figure 3.5**.

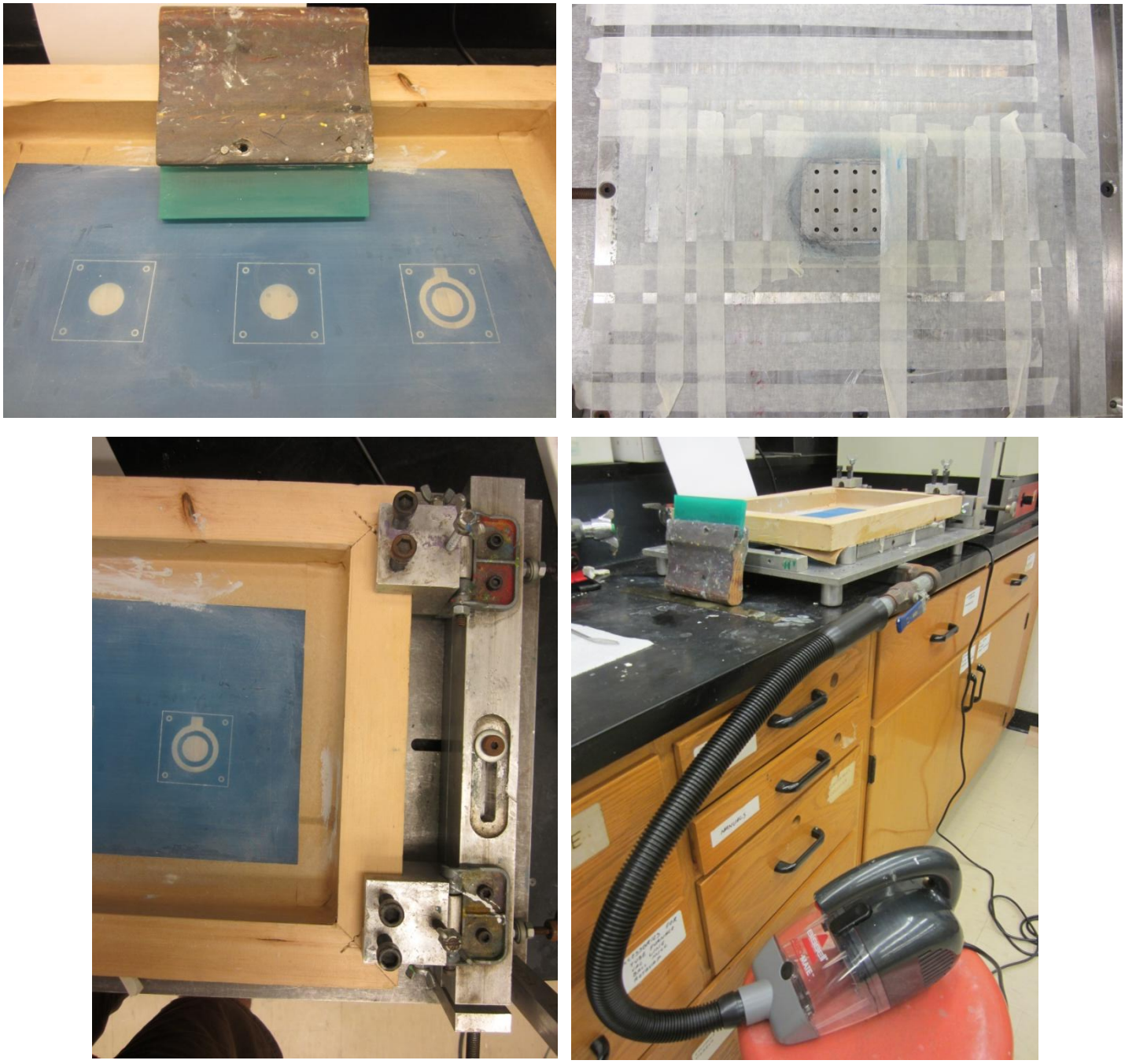

Figure 3.5 : Manual Screen-printing apparatus. (A) The three stencils from left to right are respectively for the phosphor, $BaTiO_3$ and silver inks. A squeegee (green) was used to spread the ink. (B) The surface under the screen that contains holes to create suction to hold the substrates in place. (C) The screen supports that allow it to move in the x-y and z directions relative to the bottom surface. (D) The hand vacuum is linked to the apparatus with a rubber seal.

3.3.2 Technique

The inks are prepared by using protocols similar to these mentioned in the literature for printing dielectric and luminescent materials [56] . An epoxy paste is mixed with the powder to form the ink. For a given mass of the paste, we used the equivalent of 1.1 times the mass for $BaTiO_3$ powder or 1.2 times the mass for ZnS powder. ZnS was chosen as a luminescent material as it was shown to be effective in such devices [57], [58] and is economically suitable for use in large quantities. The solution is stirred vigorously and put in an ultra-sound basin to create a homogenous and air bubble free solution. This mixture can be prepared in advance and stored until it is needed. Just before the printing, a liquid solidifier is added to the ink, 0.36 g for every 10g of powder. The solution needs to be stirred again until it is smooth and put in the ultra-sound basin (any vibrating support device can do). To help get rid of the air bubble, slow linear streaks with a metal spatula were done in the solution while it was vibrating. It is essential for the ink to be prepared carefully so that it does not contain air bubbles because they can cause important perturbation on the surface. However, if too much time is taken, the ink will solidify slowly on the screen making the printing increasingly difficult.

A thick line of ink is first put on the screen just above the stencil, extending slightly wider. With the squeegee, the ink is gently spread in a single linear motion, without any pressure on the screen, to fill the mesh in the stencil. With a good amount of pressure, a quick streak of the squeegee is then done over the stencil to print the ink on the substrate underneath. The squeegee needs to be at an angle between 45° and 60° to ease the penetration of the ink through the screen. The ideal print would take only one streak of squeegee and yield a smooth surface, but it does not happen frequently, only a few samples were perfect after a single streak. Often, small defects appear on the surface and require a second streak with some added ink but reduced

pressure or speed to smooth them out. This will increase the thickness of the sample, but, for the purposes of this project, this is not a problem since profilometry measurements are done on all the samples – the relative permittivity calculated will remain the same as long as the thickness is known.

The wet samples are then placed in an oven at 110 °C for 20 minutes to quickly solidify the ink and a second layer is applied after rotating the samples 90° to ensure that the surface has no pin-holes. It is very important to carefully wash the screen immediately after completing the printing of a series of samples. The mesh openings can otherwise stay obstructed and it is extremely difficult to clean once the ink solidifies.

3.4 Profilometry

A surface profilometer was used to measure the thickness of the $BaTiO_3$ layer in the printed samples. Because of technical difficulties, different profilometers were used during this project. The DekTak 150 (Veeco Instruments) was used first, at Laval University, and the KLA-Tencor P16+ was used second at the Surface Interface Ontario center at the University of Toronto, **Figure 3.6**.

Because of the stress exerted on the substrate during the printing and drying process, the surface tension curves the samples. This makes the profilometry measurements more difficult. While the instrument's software can level the data for a linear tilt, it cannot compensate for a parabolic surface. Small weights or double-sided tape were used to flatten the substrate as much as possible. All samples were usually measured three times to obtain a statistical sampling. Because of the roughness of the surface, the height may vary by 15% on a given sample. That is

why it was important to do at least three measurements to yield an average thickness that was representative of the sample.

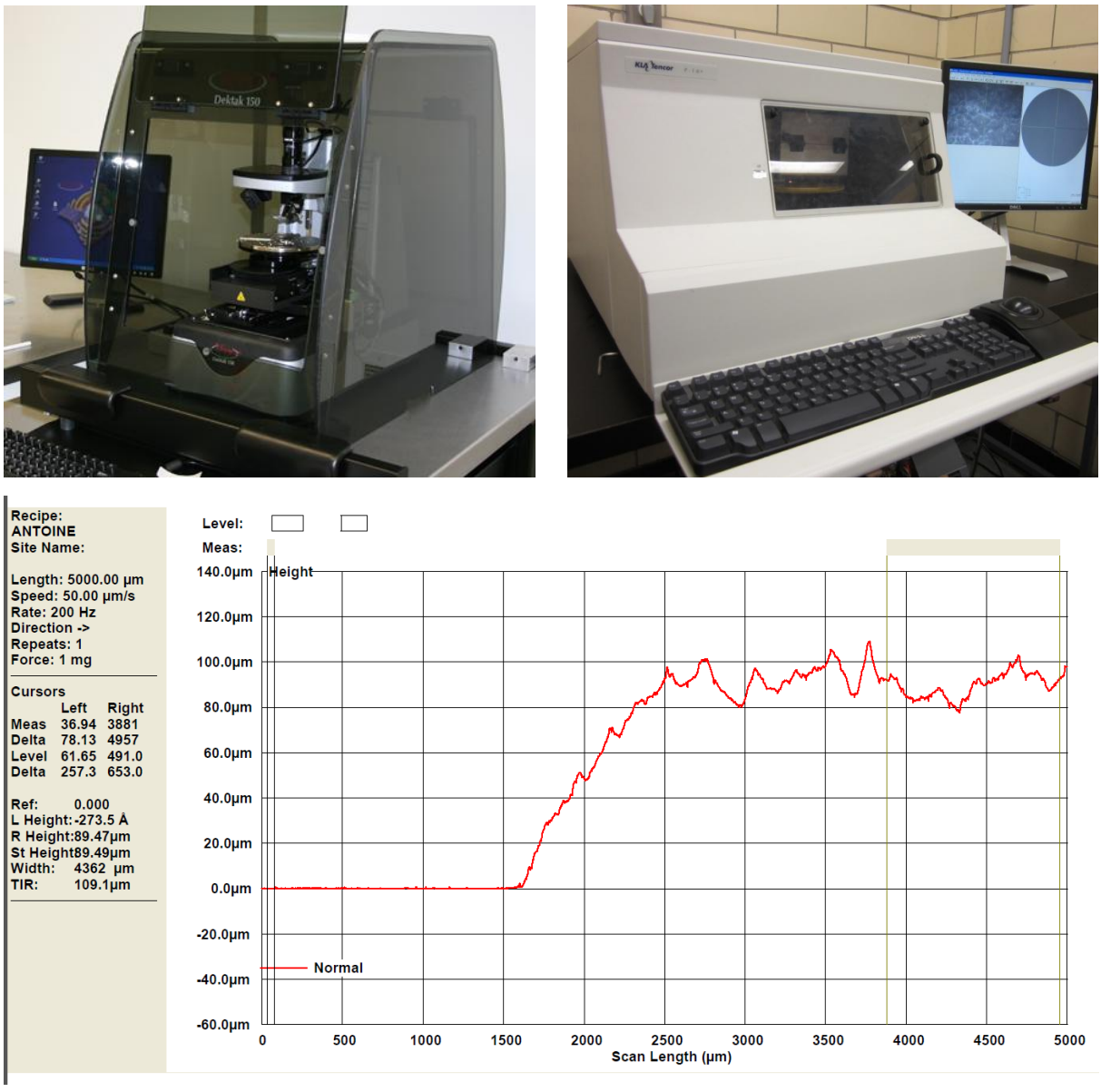

Figure 3.6 : (A) DekTak 150 profilometer (B) KLA-Tencor P16 + profilometer (C) Example of profile measurement with the KLA-Tencor P16 + of a $BaTiO_3$ ink layer (49.7% of AcAc) printed directly on the ITO surface - sample for relative permittivity measurement.

3.6 Impedance Spectroscopy

The impedance spectroscopy measurements were accomplished with the use of VoltaLab 80, the combination of the PGZ 402 potentiostat and the VoltaMaster 4 Software. A three probe cell (using a working electrode, a counter electrode and a reference electrode) was used for the impedance measurements. The working electrode and the counter electrode are in contact with the silver that has been printed as an outer ring, as close as possible to the other layers' border and as a small contact on top of the dielectric, creating a capacitor-like system. The potentiostat applies an alternative potential of low voltage to the device and continually changes the frequency. The system generates a very low current, in the range of 100 μA, that is near the limit of detection of the instrument. The Voltalab measures the impedance response of the samples in a range of frequency typically from 500 Hz to 10 kHz. A Nyquist plot is also generated by measuring the real and imaginary components of the current (as discussed in Chapter 2). We used the electrochemical impedance spectroscopy spectrum analyser (EISSA) software to compare and fit the data we obtained to a perfect equivalent circuit. The circuit model started with a low resistance and continued with a capacitance in parallel with a very high resistance **Figure 3.9**. This circuit represents the electrons' path in a perfect device and deviations from it are key to understanding problems that can occur with the $BaTiO_3$ films and to examine the quality of the screen-printing.

A single-sample support that allowed for better electrical contacts and quick manipulations was assembled by professor Pietro to facilitate the measurements (**Figure 3.11**). When the electrodes are connected, the source of the system, the cell, is activated and we can start our sequence program. Different editable programs are available for impedance measurements. We used a sequence that measures the impedance by small frequency increments,

with a short time between each to make sure the electric charges flowing in the system had stabilized before the program calculates the capacitance. The program in the measurement used a set of logarithmically decreasing frequencies, about 10% between each value, from 10 kHz to 0.5 kHz with a resting time of 2 seconds (approximate time constant for the system τ = 0,005 s). When the capacitance is known, it is possible to directly compute the relative permittivity with the profilometry data using the capacitance formula :

$$C = \varepsilon_0 \varepsilon \frac{A}{d} \tag{3.1}$$

ε : relative permittivity, ε_0 : vacuum permittivity, A : silver ink's area, d : $BaTiO_3$ ink thickness

$$\varepsilon = d \frac{C}{\varepsilon_0 A} \tag{3.2}$$

The relative permitivity only needs *d* to be measured when the area capacitance (*C/A*) is known. Since the impedance spectroscopy registers data for a series of frequencies, an average of the dielectric constant is done near the frequency (1000Hz) that would be used in the electroluminescence device.

To verify the accuracy of the potentiostat, first measurements were done using a reference circuit box that came with the device, see **Figure 3.7.** Using the same program but with a larger range of frequencies than what was used afterwards on the experimental samples, the impedance of two reference circuits was measured, i.e., with the working electrode plugged in positions C and D. The data showed clear and consistent Nyquist plot semi-circles, representing the expected form for the RC circuits, and the impedance fitting program yielded excellent result as can be seen in **Table 3.1**.

Table 3.1 : Resistance and capacitance values measured by the potentiostat compared to the theoretical values given for the electric circuit of the RCB 200 box.

Element	Measurement	Theoretical values	Uncertainty th. values
A-R1	1.19 kΩ	1.21 kΩ	1%
A-R2	4.97 kΩ	4.99 kΩ	1%
A-C1	4.70 nF	4.7 nF	10%
B-R1	1.19 kΩ	1.21 kΩ	1%
B-R2	4.97 kΩ	4.99 kΩ	1%
B-C1	4.69 nF	4.7 nF	10%
B-R3	9.95 kΩ	10.0 kΩ	1%
B-C2	0.96 µF	1.0 µF	10%

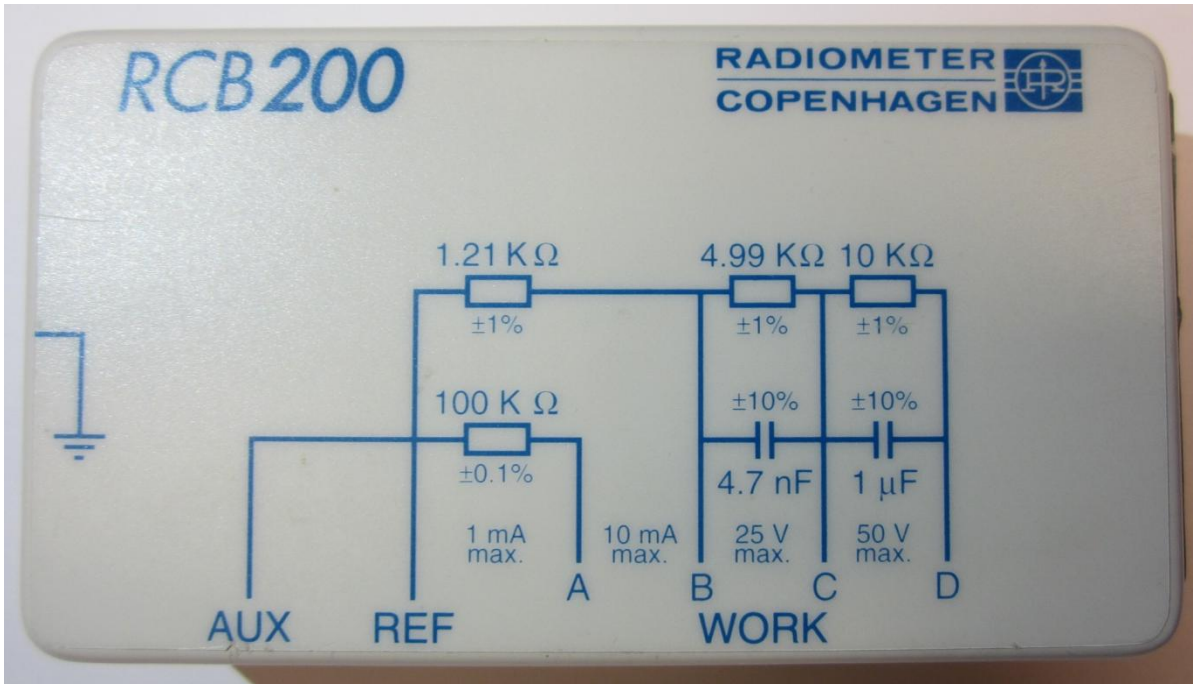

Figure 3.7 : Reference circuit box to calibrate the potentiostat. Auxiliary and reference electrodes were plugged in at the AUX and REF ends and the work electrode was plugged at the C end first (one capacitor-circuit) and the D end afterwards (2 capacitors-circuit)

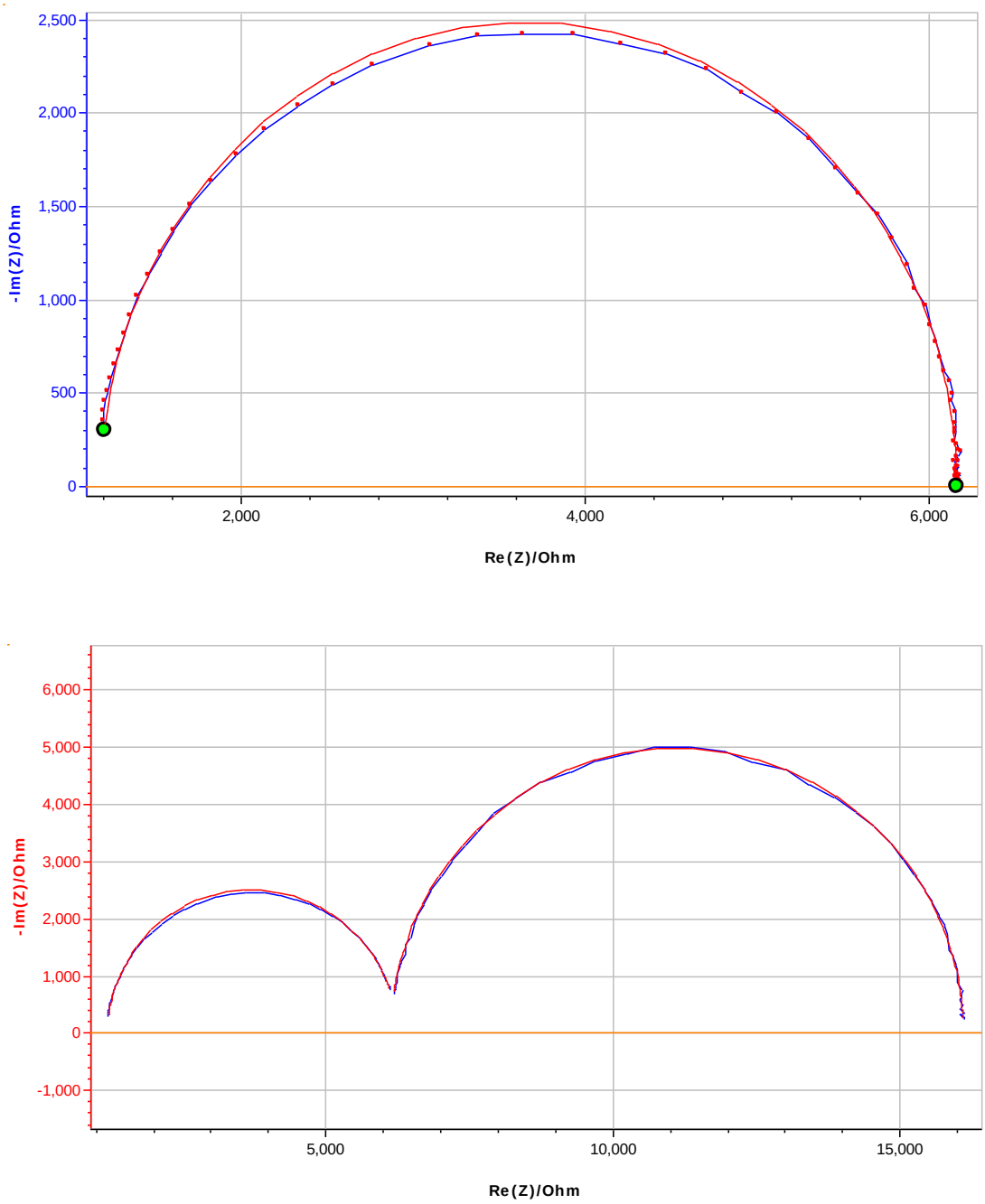

Figure 3.8 : Nyquist plots of reference box for circuit C (top) and D (bottom), experimental data in blue and simulated plot in red.

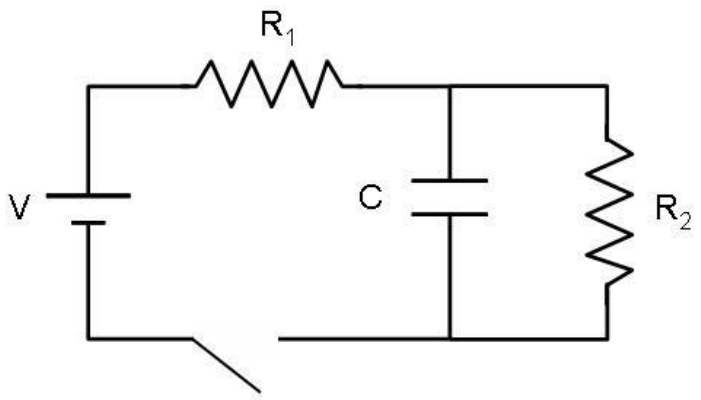

Figure 3.9 : Equivalent circuit for the devices in our project. R_1 is technically as small as possible, representing the resistance of the circuitry around the printed layers. C is the capacitance of the system and the characteristic that is mostly affected by the changes in $BaTiO_3$ particles. The layers resistance R_2 needs to be extremely high for the device to behave primordially in a capacitor manner and ranges usually above 1MΩ.

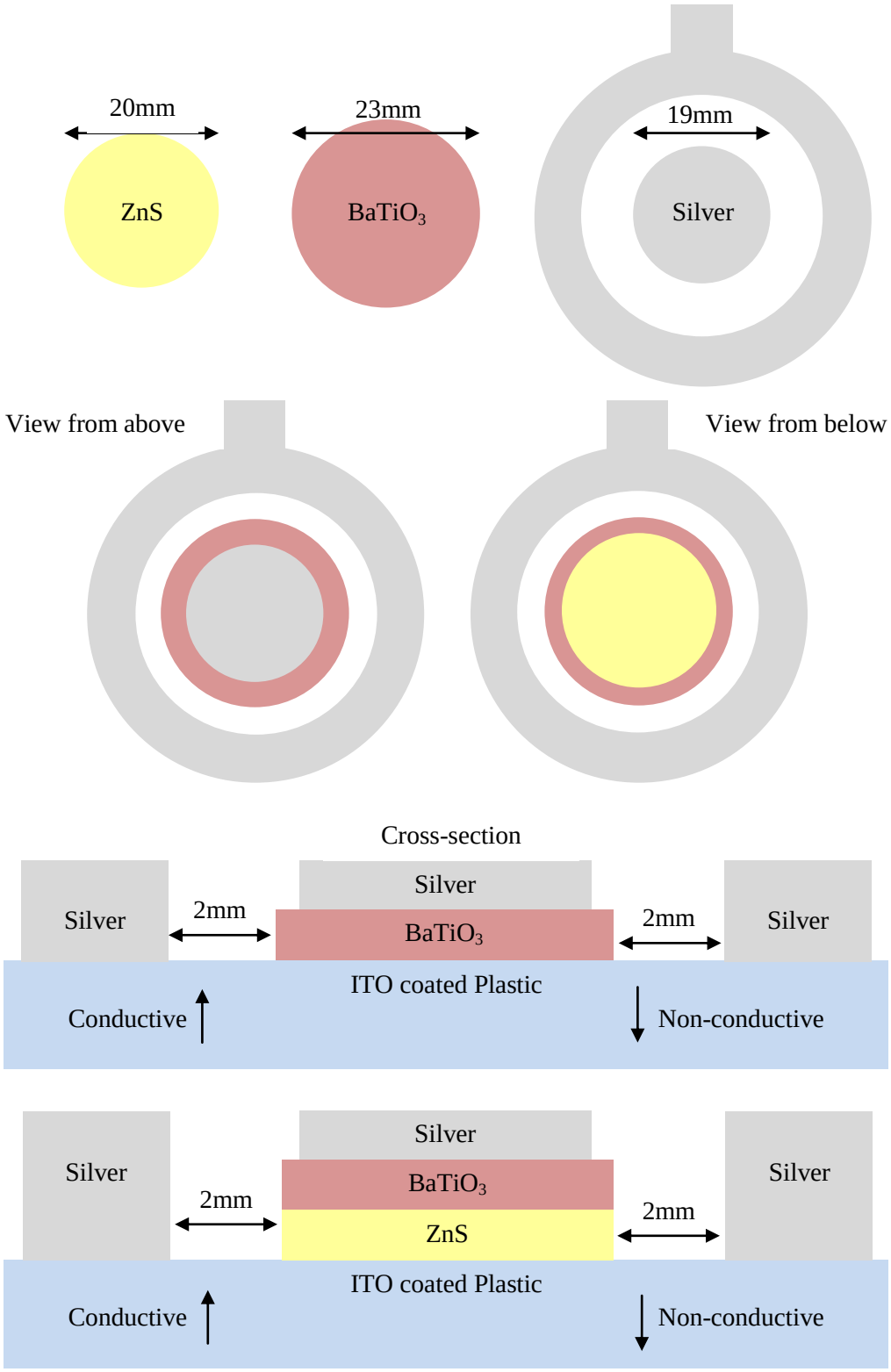

Figure 3.10 : Printed device diagram with and without luminescent ZnS layer.

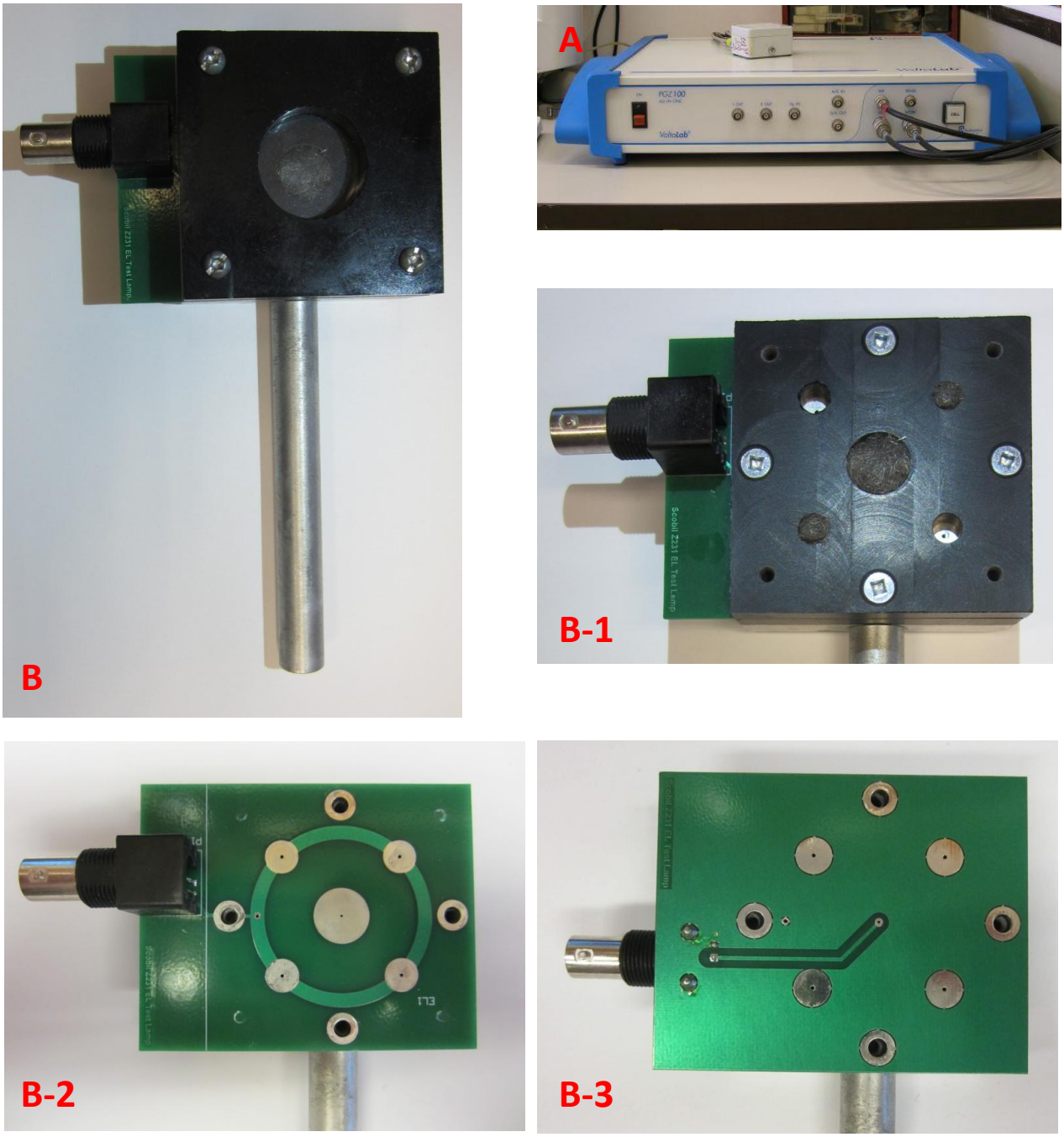

.

Figure 3.11 : (A) The potentiostat in use for the impedance spectroscopy measurements. (B) Support for the printed samples. B-1 shows the middle layer of the device with fine steel wool to provide a good contact on the silver electrode. B-2 and B-3 are pictures of both sides of the bottom layer, a simple electronic circuit transferring the current to a coaxial cable connection.

3.7 Photometry

The same support that was used for the impedance spectroscopy is used to perform the photometry measurements. The source used for the former could not apply the voltage needed for the electroluminescence to occur in the device (300 V), so another power source was required. A small circuit board was built to convert 4.5 V, produced by three AA batteries (1.5 V each) to a 300 V input in the device with a frequency of 1000Hz. The board was kindly lent to us by Scobil Industries inc. .

A window at the back of the support makes it possible for the electroluminescent light to be captured by the detector. Since the phosphor ink is the first layer to be printed onto the ITO surface, there is barely any loss in light intensity due to the thin transparent plastic substrate.

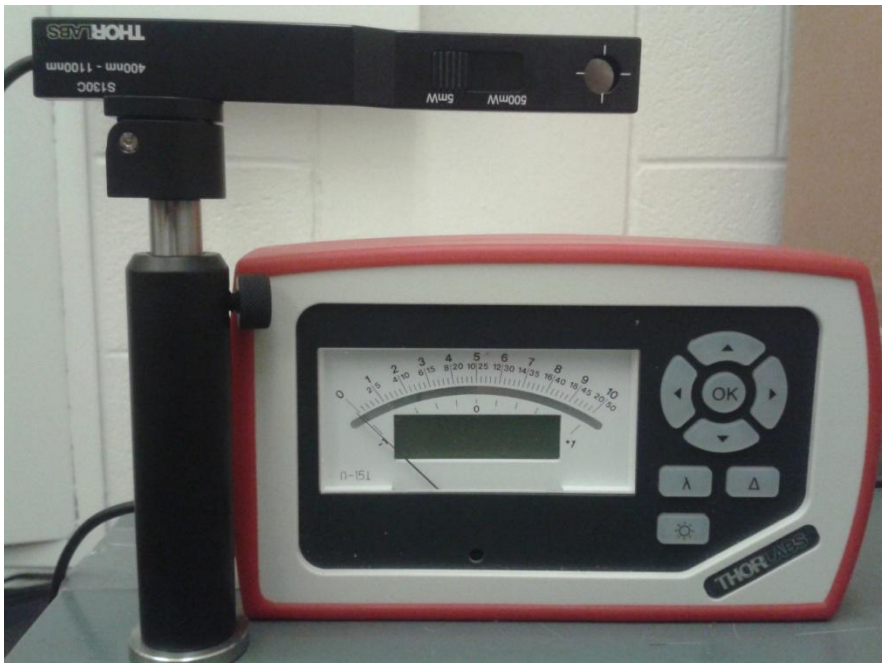

Figure 3.12 : Photometer ThorLab PM100 A, small receptor aperture (9.5 mm) with 2 degrees of sensitivity (5mW and 500mW). The luminescence measurements were done at the most sensitive level.

The photometer used was a ThorLab PM100, **Figure 3.12**, at the highest sensitivity level. The photodetector aperture was placed directly in front of the sample, parallel to its surface, at a distance of 1.2 cm (4 mm thick transparent plastic and detector at 8 mm from the device). Since the power of light emitted was in the nW range, it was essential to ensure that the luminescence measurements were not affect by any source of light outside of the experiment. The laboratory lights were turned off and the set up was put under an opaque container to isolate it from any remaining light.

To obtain the proper potential – 300 V at a frequency of 1000 Hz – to create the luminescence in our device, we used a small circuit to convert the current given by three 1.5V AA batteries, **Figure 3.13**. For each sample, three measurements were taken at different points in time. The sample was reinstalled in the set up every time to make sure that there were no alteration in the electrical connection. The light intensity results were observed before being entered manually into an Excel sheet for compilation.

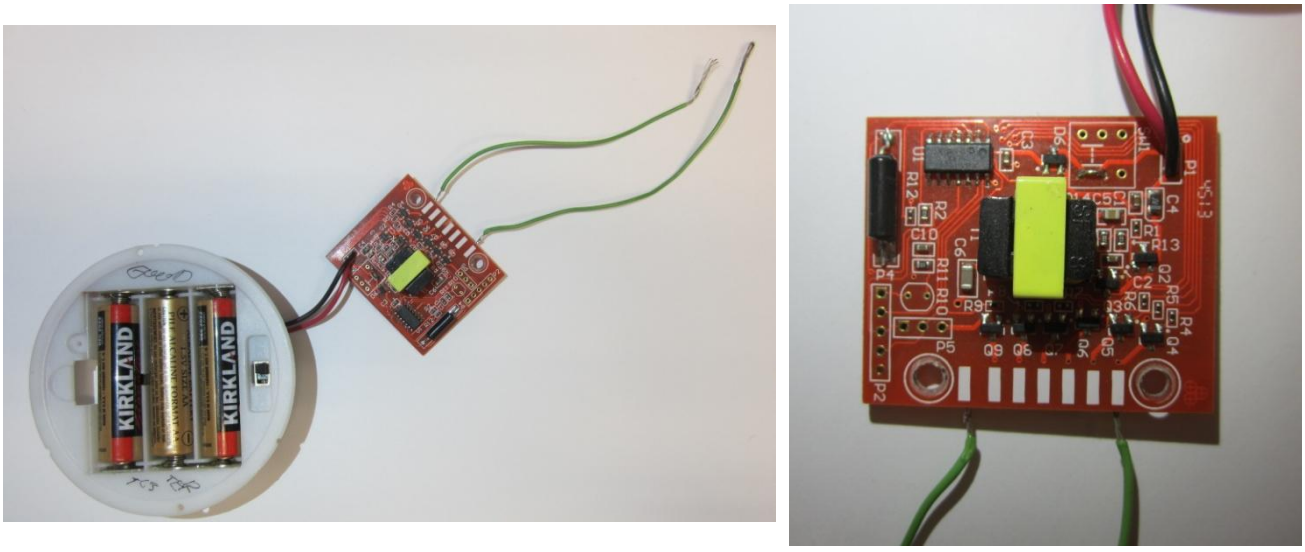

Figure 3.13 : Converter used to apply the 300 V potential at a frequency of 1000Hz onto the samples. Powered by three 1.5 V AA batteries.

Chapter 4 : Results and Discussion

Introduction

During this project, 7 different types of powder samples were studied : Commercially available powder (Com), un-doped sample prepared with varying concentration of acetylacetone (U0, U1 and U2), lanthanum-doped samples (D1, D2, D3) prepared with the same acac concentration as U1, **Table 4.1**. Many other samples were prepared, which consumed time and effort, but did not contribute to the results presented in this chapter. Earlier in this project, several samples were deemed inadequate, due mainly to contamination. In addition to these, an entire set of doped particles that had been synthesized through the Pechini method couldn't be used and the method had to be abandoned, as explained in section **4.2**. Although there were some obstacles, a total of 46 capacitor and 17 complete electroluminescent devices were successfully prepared. They were all used to determine the dielectric constant and to study the luminescence, .

Samples	Experimental Characteristics
U0	Sol-Gel method with 100% (initial amount) acetylacetone
U1	Sol-Gel method with 71 % acetylacetone
U2	Sol-Gel method with 49,7 % acetylacetone
D1	Sol-Gel method with 0.3 % (relative to Ba) Lanthanum
D2	Sol-Gel method with 0.5 % Lanthanum
D3	Sol-Gel method with 0.7 % Lanthanum

Table 4.1 : Description of all non-commercial samples analyzed for this project, with their corresponding abbreviations.

4.1 SEM Observations

It was observed that the nanoparticles respected the standard morphology of perovskite structures. The particles showed right angle apexes and square or rectangular surfaces, characteristic of $BaTiO_3$'s crystal structure in cubic or tetragonal form. Because of the non-conductive nature of the particles, as mentioned in previous chapters, it is difficult to obtain a very clear image with an SEM because of charging.

The samples U0, U1 and U2 were prepared with different concentration of acetylacetone, but can't be proven to follow the expected model, in which higher concentration leads to bigger particles. The un-doped particles turned out to all share the same size within the error - averaging 103 nm for U0, 99 nm for U1 and 97 nm for U2. The uncertainty had to be fairly large, ± 5-7 nm, due to the fact that the measurements were done manually on the imaging software *Image J*. The average deviation also presents a similar value. The doped samples appeared to increase in size (around 105 nm) but were at the limit of the error range. The size distribution had a high standard deviation, which lowered the certainty of the average difference in size, see **Table 4.2**. However this underscored something important. We realized that seemingly individual particles were in fact agglomerations of smaller particles. Although it is difficult to determine the exact size of the agglomerated particles, their size was estimated to be between 20 and 30 nm. The Com powder consisted mainly of much larger particles without any sign of agglomeration and few particles smaller than 100 nm. The SEM observations also confirmed that the three doped samples, which all had the same acac concentration, maintained a stable particles size. We can see examples of the particles from each sample in **Figure 4.1**.

The first capacitors were made with a commercial printer and the U0 powder. Their dielectric layer's particle density was observed by SEM. There was a major difference in density between the commercial samples and the U0 samples, **Figure 4.2**. This could be due to the experimental powder being more heterogeneous. Il could also be due to a difference in the amount of epoxy used during the screen-printing. The person responsible for printing that first series would have had a large supply of commercial powder available next to the low volume of U0 synthesized. The complications related to commercial printing and the very poor impedance spectroscopy results yielded by the U0 samples, lead us to cease investigating the U0 powder. The rest of the study focuses on the other samples in **Table 4.1**.

Particle	U0 [nm]	U1 [nm]	U2 [nm]	D1 [nm]	D2 [nm]
1	96	104	89	94	125
2	98	95	85	115	102
3	99	92	101	96	107
4	102	95	98	103	99
5	105	101	95	96	95
6	109	92	104	108	97
7	103	107	92	99	99
8	99	99	97	96	98
9	94	106	103	118	83
10	92	100	114	101	120
11	111	102	93	106	122
12	114	98	92	108	104
13	105	108	106	102	111
14	102	104	89	115	92
15	107	95	101	117	100
16	98	93	91	93	105
17	115	96	102	106	116
18	110	101	95	114	97
19	99	95	92	125	101
20	97	104	96	118	107
Average	103	99	97	107	104

Table 4.2 : Particle size measurements on 20 different objects from SEM images. Because of the large uncertainty of the measurement, the different samples show the same particle size within the error.

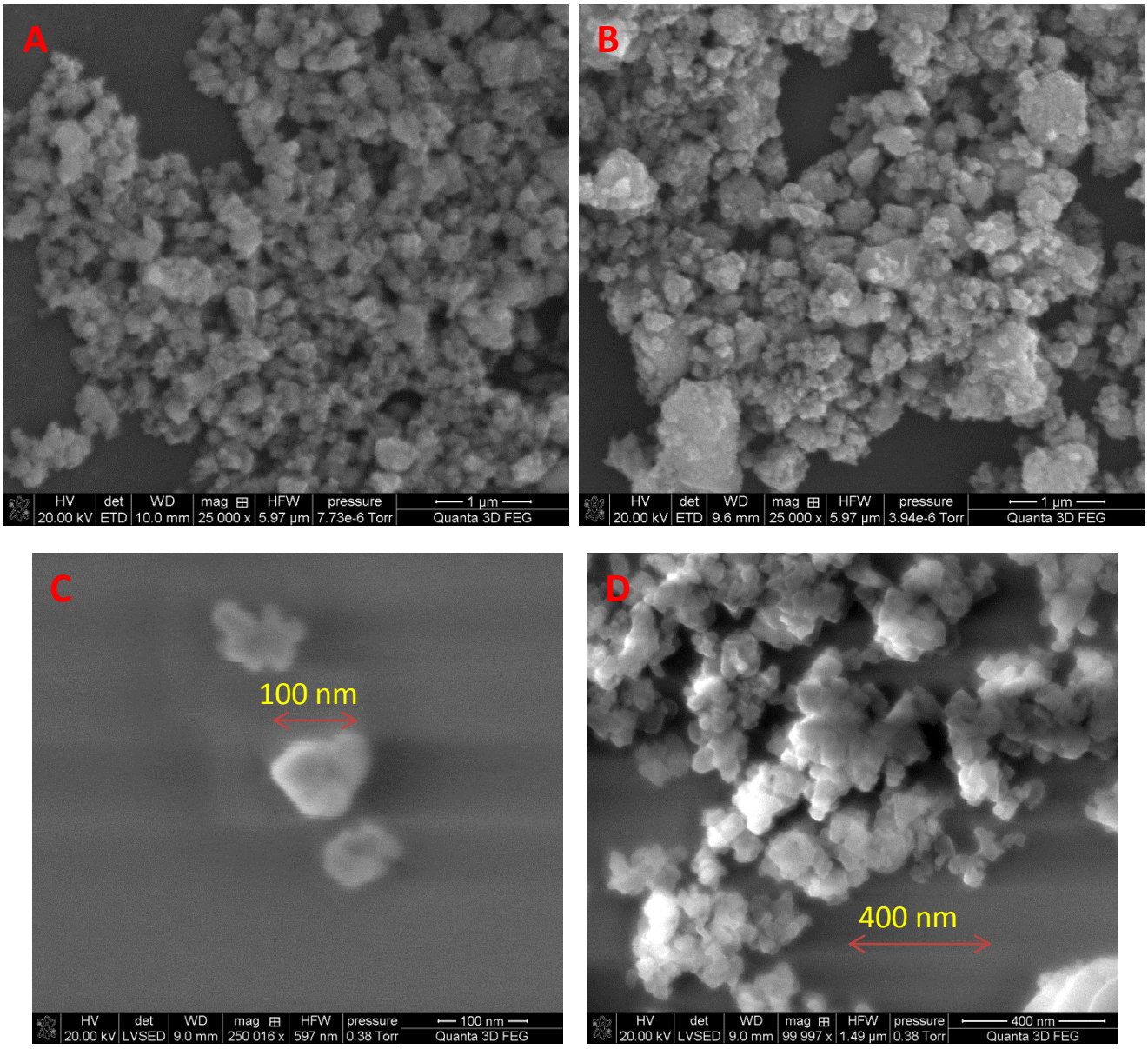

Figure 4.1 : Nanoparticles from U1 (A) and U2 (B) syntheses (71 and 49,7% AcAc respectfully). Individual (C) and agglomeration (D) of nanoparticles from the U2 synthesis.

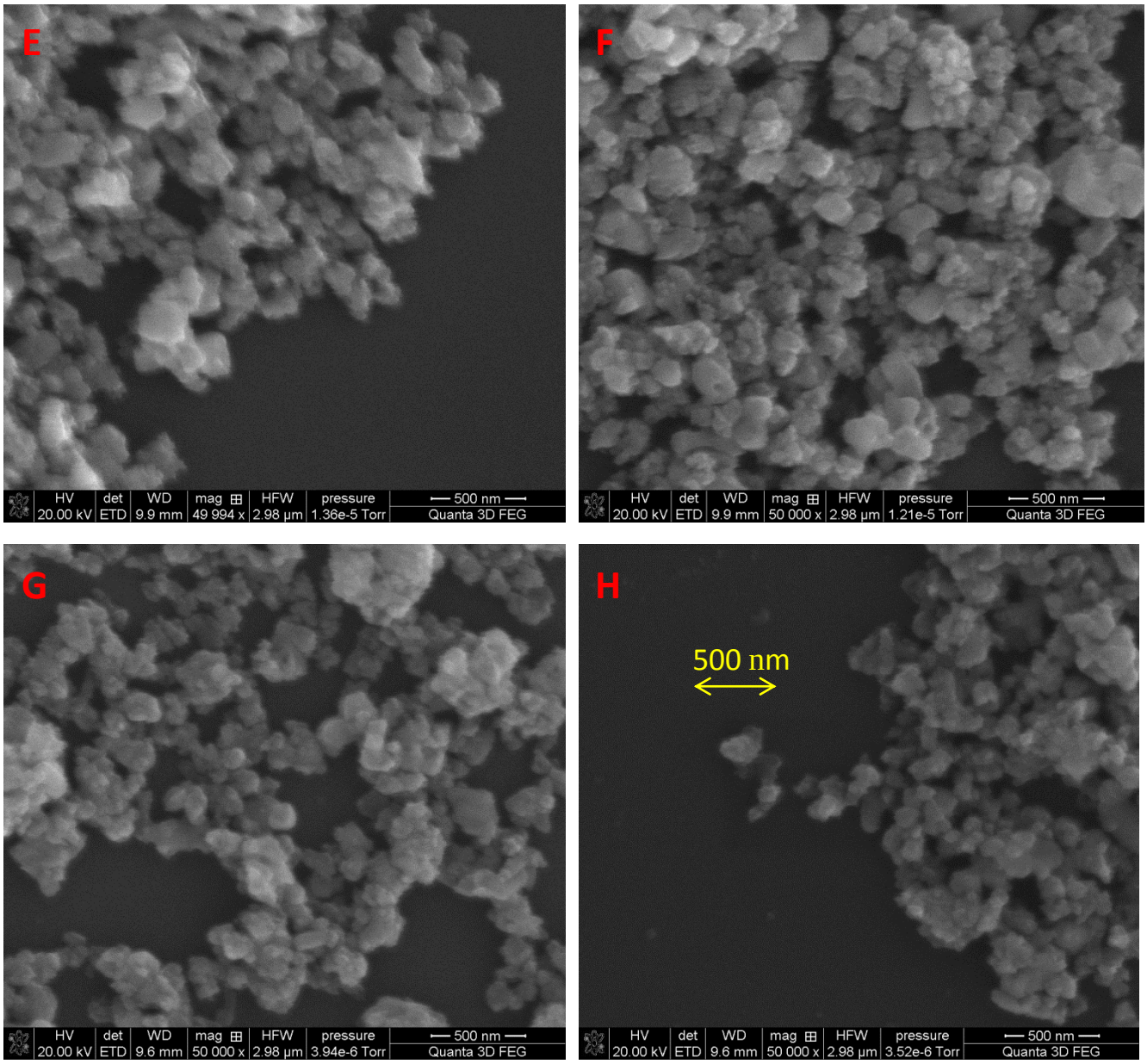

Figure 4.1 (continue) : E-F, particles from the D1 synthesis. G-H, particles from the D2 synthesis.

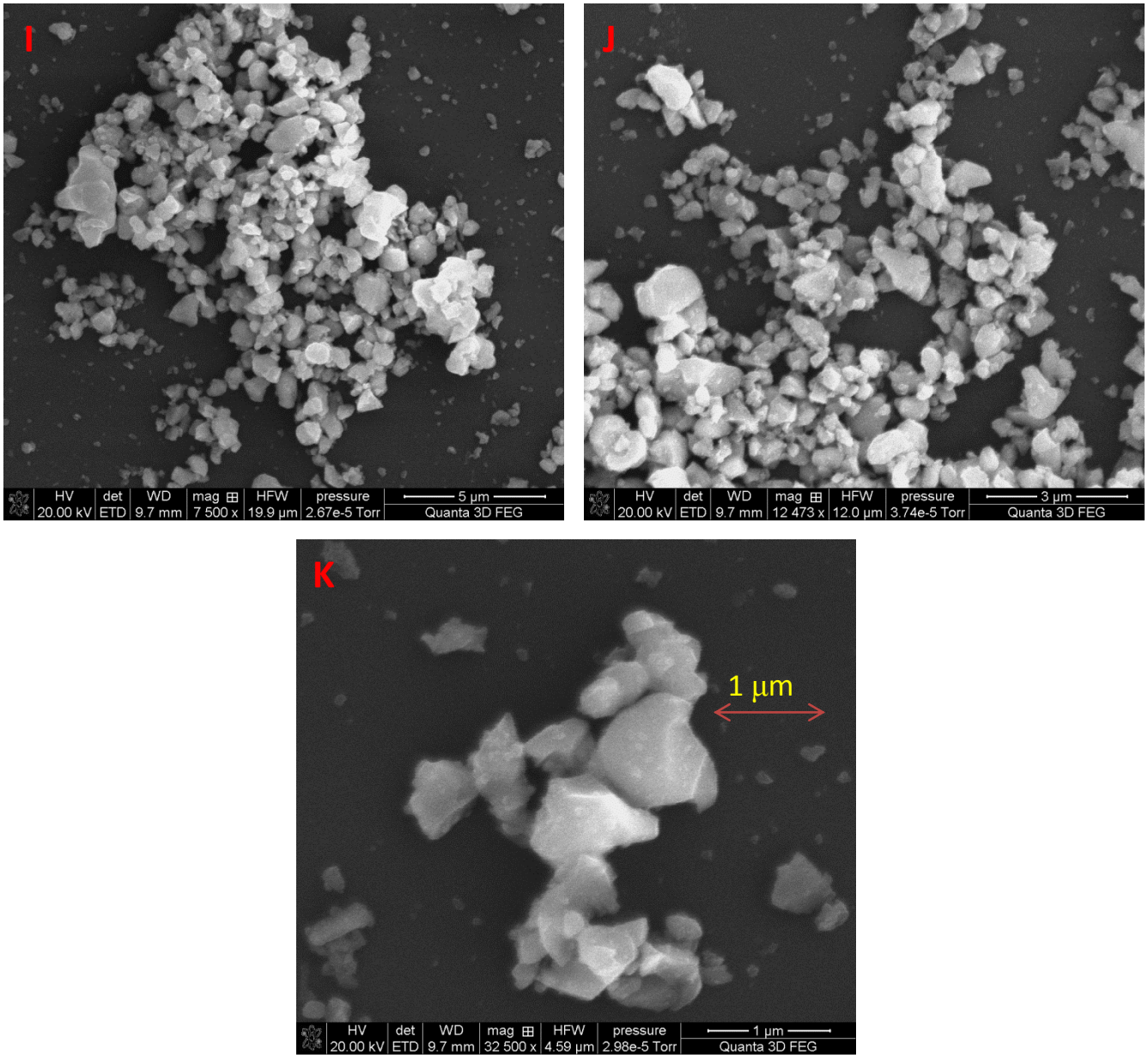

Figure 4.1 (continue) : I-K, particles from the commercial powder (Com samples). G-H, particles from the D2 synthesis. The commercial material consists mainly of larger sized particles, that do not show signs of being agglomerations, as well as a few small particles below 100 nm.

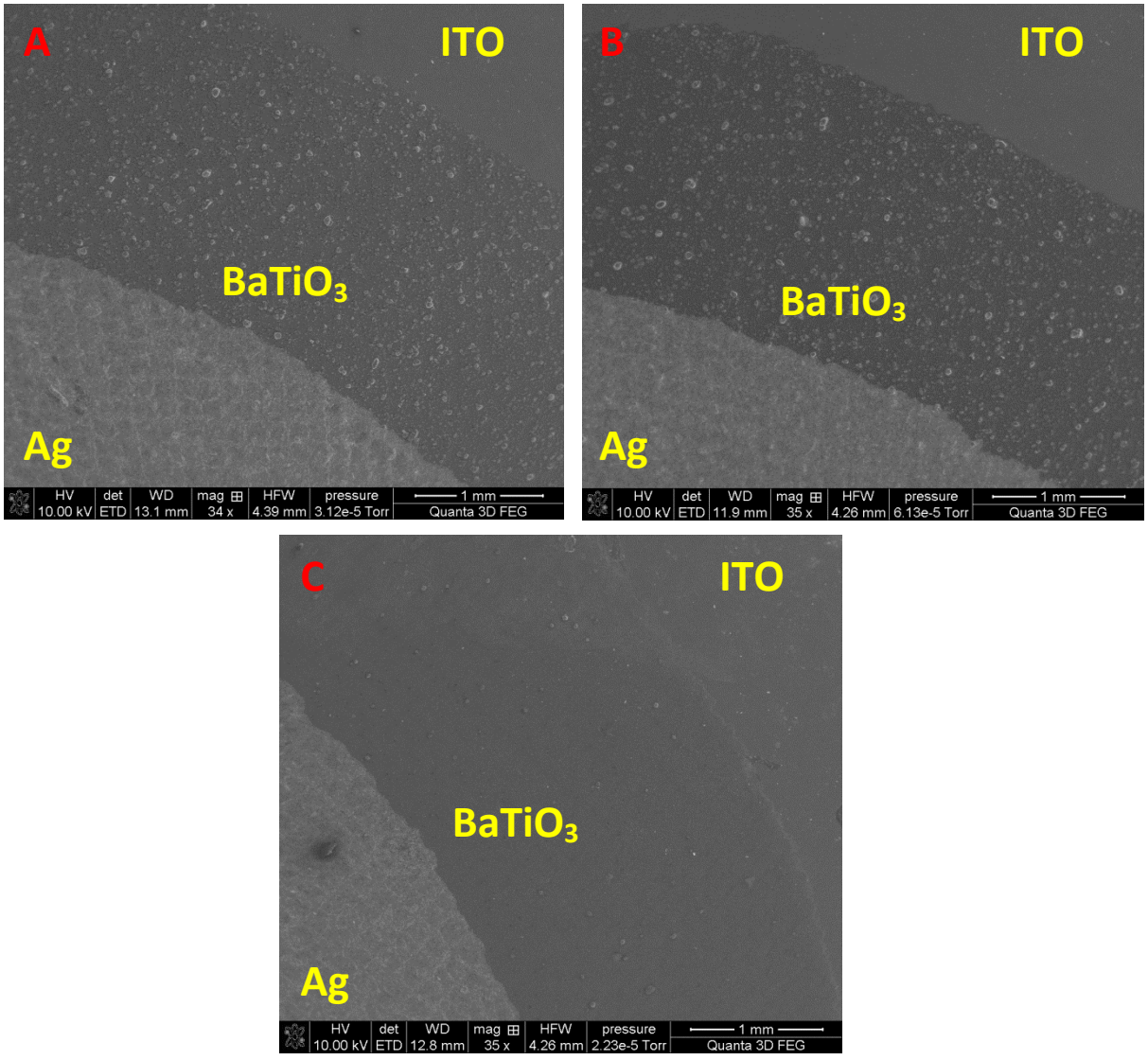

Figure 4.2 : Printed dielectric layer observation. The bottom left corner of each image is occupied by the silver layer, the middle is occupied by barium titanate and the top right corner is the conductive ITO substrate. A and B were with U0 powder from two different syntheses. C was made with the Com powder.

4.2 X-ray Diffraction Spectra

A certain amount of barium carbonate was found to be always present in the samples. As explained in chapter 3, different precautions were taken to minimize the contamination, but impurities are hard to eliminate completely with this method of synthesis. Particularly in our laboratory conditions, since the syntheses were not carried out in a neutral atmosphere glovebox or in a specialized furnace. Some modifications were applied to the syntheses such as adjusting the time and temperature during the heat treatment, as well as boiling the water and flowing argon through it before using it to create a CO_2 free solution. XRD measurements were a suitable way of detecting the formation of $BaCO_3$ in our samples and was used extensively.

The first XRD measurements on satisfactory undoped powders U0 and U1, were processed through a Rietveld refinement analysis software. This ensured a clear picture of the crystal structure of the $BaTiO_3$ and made possible the quantification of elements (University of Toronto, Chemistry Department). We were able to confirm that the samples are crystalline and that, unusually, the peaks were located between the expected peaks for the tetragonal and cubic phases. In fact, they were slightly closer to the tetragonal phase, see **Figure 4.3**. This could possibly be a result of the core-shell structure proposed in the literature [17] . Further XRD analyses were not done with Rietveld analysis because the person responsible for the previous measurements retired and the people who subsequently handled the XRD measurements didn't have access to the software (6 spectra taken at Laval University, Geology department, 4 spectra taken at the University of Toronto, Earth Science department).

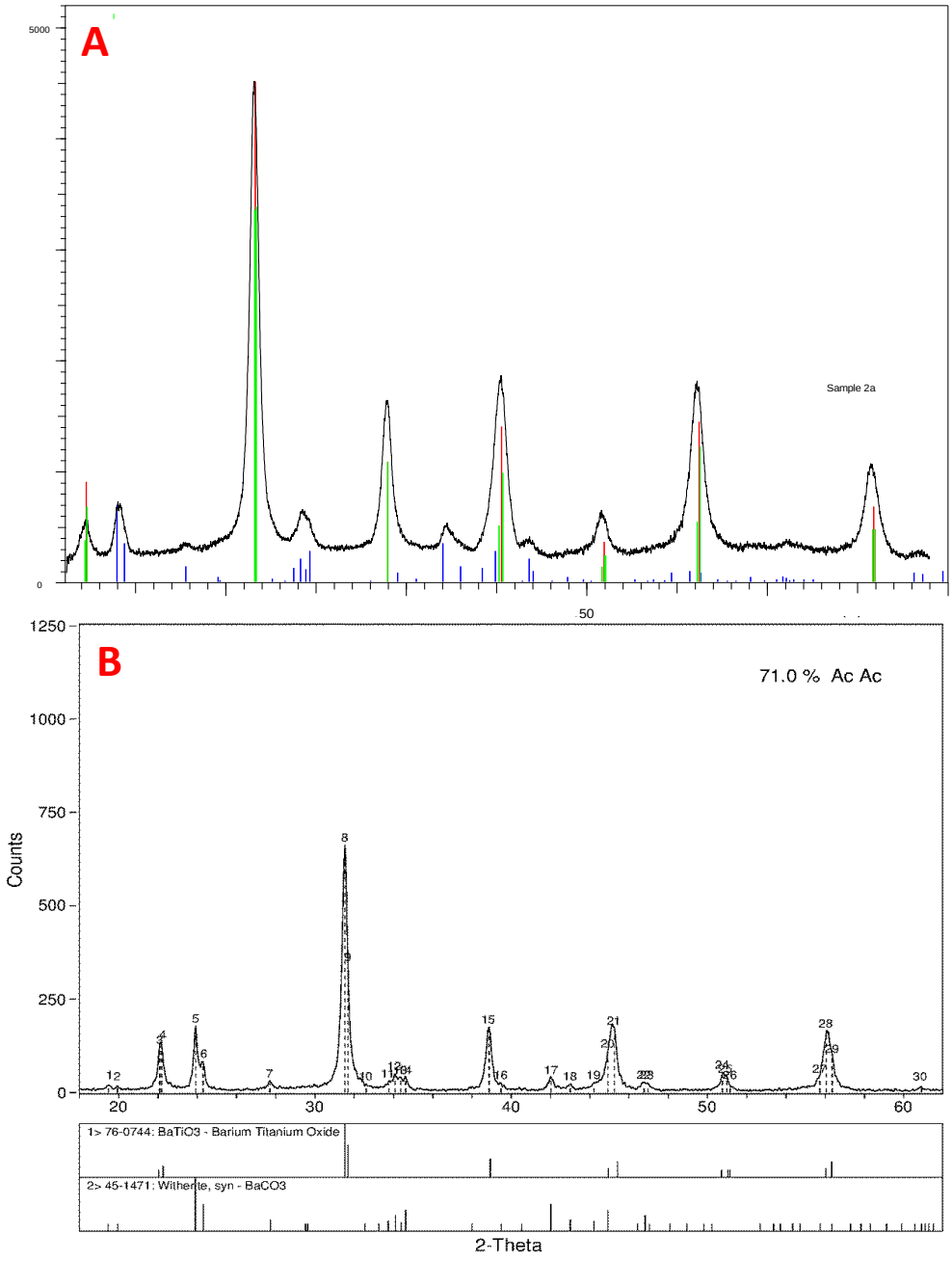

Figure 4.3 : A : X-Ray spectrum of sample U0, analyzed with the Reitveld refinement – Technique used to compare experimental peaks using height, width and position to an extremely large data bank of spectrum patterns of crystals. The black line are the measurement, the red lines represent the Pm-3m cubic $BaTiO_3$ reference, the green lines represent the P4mm tetragonal $BaTiO_3$ reference, and the blue lines show the $BaCO_3$ reference. B : X-Ray spectrum of sample U1 (large synthesis), with reference peaks for $BaCO_3$ and $BaTiO_3$.

Since the amount of powder was deemed too small for a satisfactory production of samples, a larger U1 synthesis was done and reanalyzed with the XRD. The new U1 and U2 powders showed clear barium titanate peaks (T) and some presence of barium carbonate (C). To estimate the percentage of titanate in the powder, the ratio of the intensity of the peaks (T/[T+C]) was calculated. Although this method is considerably less precise than a modern quantitative XRD analysis, it does give a proper idea of the material's purity, as a completely pure powder would obtain a result of 100%.

The Pechini method samples showed a minority of barium titanate and a high level of barium carbonate contamination in the powder, **Figure 4.4**. They were deemed unsuitable for use in dielectric measurements and for luminescence measurements in complete devices. After discussing the matter with professor Pietro, the conclusion was that the thermal treatment to transform the resin into a crystalline powder should have been done under an oxygen atmosphere to help cleanse the carbon from the material. However, this requires a specific set-up to avoid any contact between the oxygen flow and the heating elements. Such a set-up is impossible in the oven used in this project and the necessary type of oven wasn't available at the time in other facilities.

After these disappointing results with the Pechini method, we returned to the sol-gel protocol with the intention of inserting the lanthanum in the first stage of the synthesis. The first tests were satisfying and high-volume syntheses proceeded with D1, D2 and D3 samples. An example of D1 X-ray spectrum is given in **Figure 4.5.** The doped material was found to generally contain less $BaCO_3$. This is thought to be caused partly by the fact that it was

synthesized at the end of this project with more experience and a greater care with regards to the infiltration of carbon in the samples. The D2 sample is the purest of all $BaTiO_3$ samples prepared here, with a 95,1 % ratio of barium titanate to barium carbonate. The D1 is slightly less pure at 90,5% and the D3 drops to 71,3 %, Table **4.3**. At the beginning of the D3 synthesis during the hydrolysis, a stirring problem occurred that caused a disruption in the formation of the gel network. The particles were created but the precipitation was more difficult. We think that the lower purity of this sample is related to this incident since the material had to go through more manipulations and prolonged contact with the ambient atmosphere during processing (longer centrifugation time, a more delicate washing process since the gel was less solid, which also causing additional final product loss, and longer drying time).

	Carbonate peak [arb. units]	Titanate peak [arb. units]	Diel. Constant [ ]	Ratio T /(T + C) [ ]	Diel. C. / ratio [ ]
U1	177	647	48,7	0,785	62,0
U2	212	493	40,1	0,699	57,3
D1	135	1296	36,2	0,906	39,9
D2	71	1372	167,8	0,951	176,5
D3	331	824	29,3	0,713	41,1

Table 4.3 : Intensity Carbonate and titanate peaks in the X-ray spectra with the ratio of pure titanate in each samples and the dielectric constant proportional to the amount of titanate. The third column results come from Figure 4.11, p.74. We can see that the titanate purity of the samples is not a major factor in the dielectric constant result of the material.

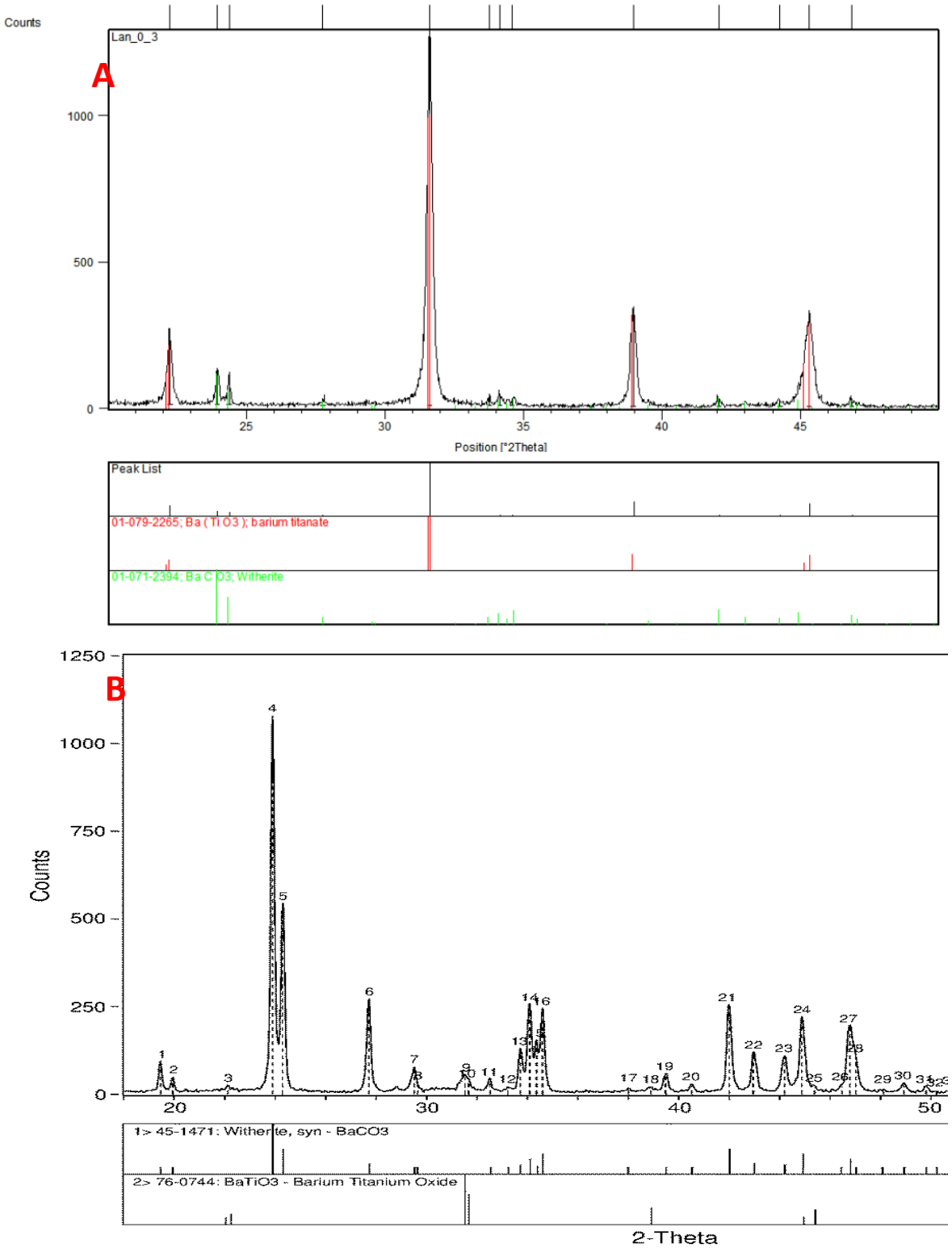

Figure 4.4 : A : D1, doped with lanthanum at 0.3%, synthesized with sol-gel method. B : equivalent sample, 0.3% Lan, made with the Pechini method – $BaTiO_3$ not formed properly. In both figures, the measurement is shown by the solid black line with reference peaks for barium titanate (red in A) and barium carbonate (green in A).

4.3 X-ray Photoelectron Spectra

Among the XPS data, the energy signature of La3d was observed within the structure of our barium titanate, **Figure 4.5-4.6**. Determining the possible lanthanum compounds turned out to be more difficult than anticipated because of the low intensity of the peaks compared to the background noise. Despite the significant presence of noise, we can see the two characteristic multiplet splits of the $La3d_{3/2}$ and $La3d_{5/2}$ electrons, F**igure 4.6**. As previously explained, the XPS technique focuses on the surface of the material, which can alter the data when dealing with low concentrations and reactive elements such as lanthanum. Therefore, it was not much of a surprise when the data showed a higher concentration of lanthanum than was introduced during the synthesis, which seems improbable. Consequently, we still can't determine the exact concentration of La in our barium titanate but the results showed promising pointers as to its insertion into the crystal structure.

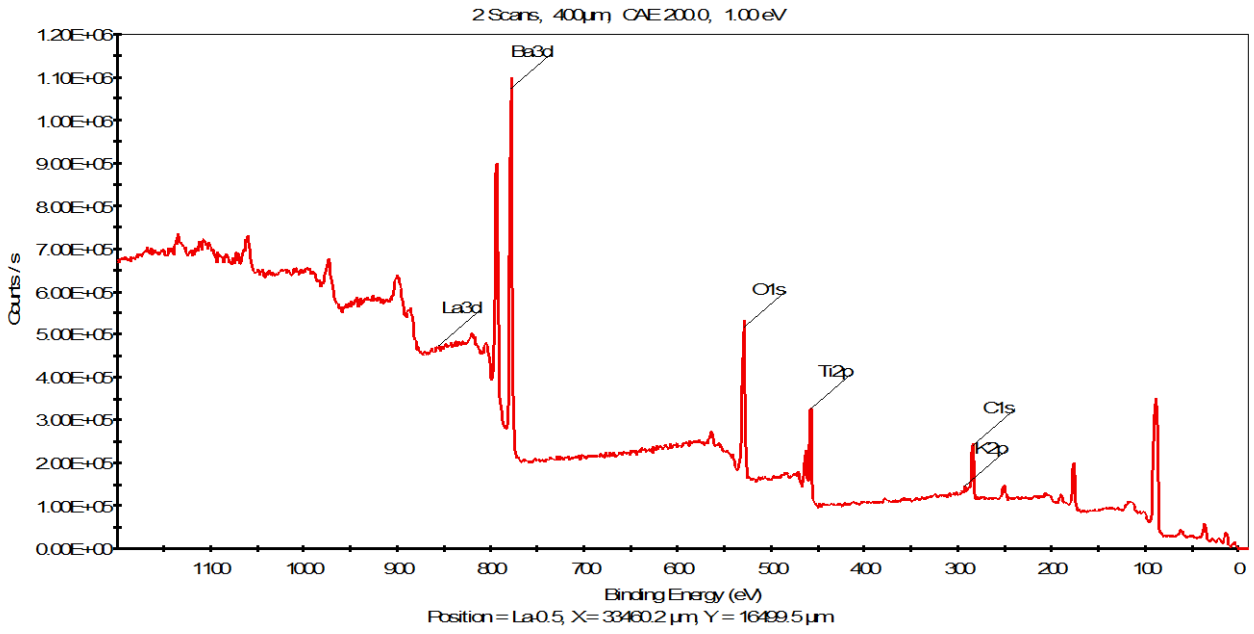

Figure 4.5 : XPS spectrum of barium titanate doped with 0.5% of lanthanum (D2). High levels of carbon are inevitable in this data as the powder is placed on carbon tape for the measurements

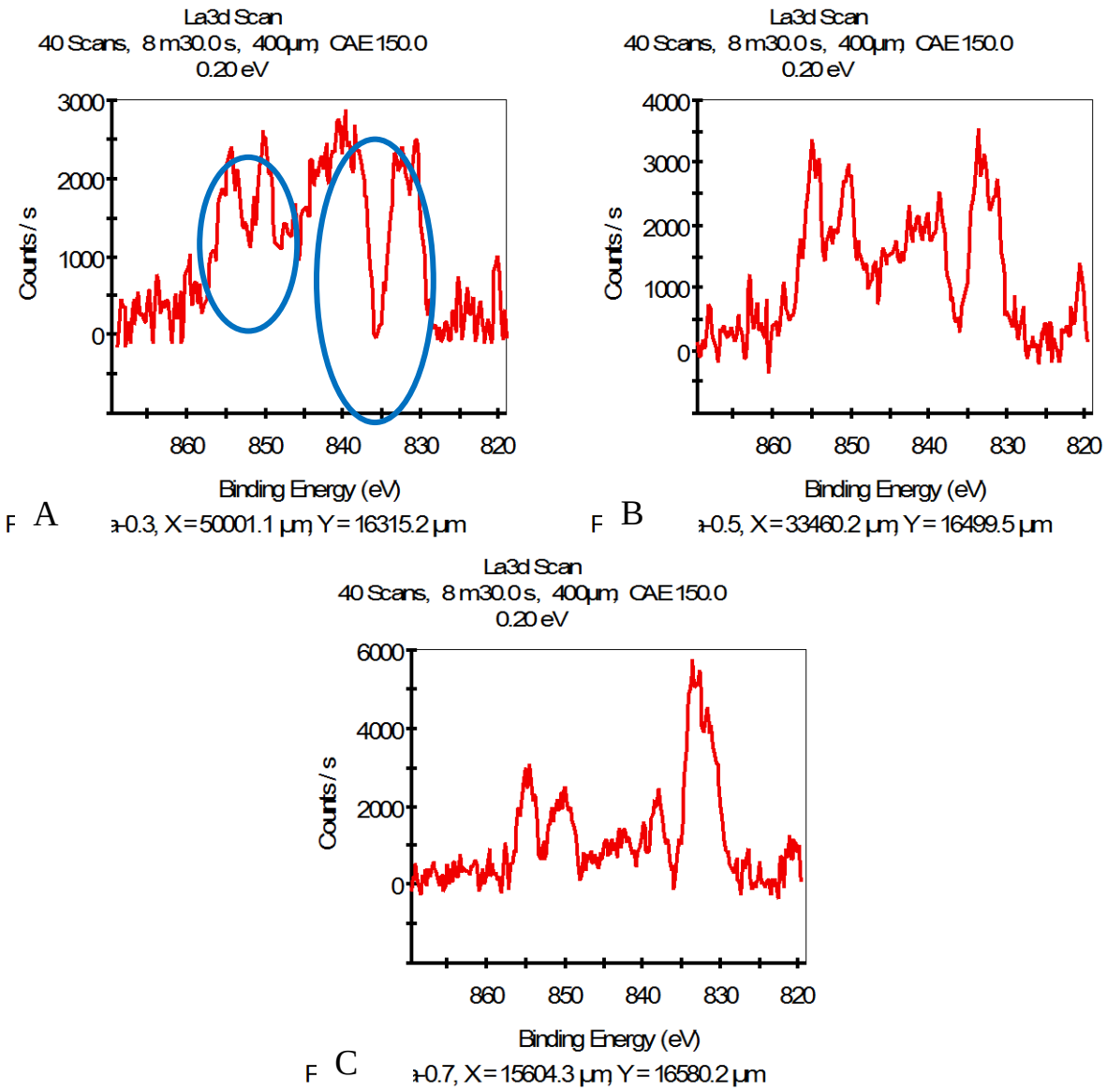

Figure 4.6 : Lanthanum XPS spectra focused on the binding energy range of La3d in (A) D1 (B) D2 and (C) D3 samples. The first multiplet split, on the left (high energy), represents $La3d_{3/2}$ and the second, on the right (low energy) represents $La3d_{5/2}$. The relevant peaks are circled in the first spectrum.

According to the literature found on this subject, the separation ΔE of the $3d_{5/2}$ peaks is the main data used in XPS literature to determine the chemical environment of lanthanum. However, in our data the intensity of the background noise in relation to the lanthanum peaks is too high to obtain a clear measurement of this ΔE, but it is possible to compare the known ΔE from various La compounds to the acquired data, as seen in **Figure 4.7**. We can see that the lanthanum, or at least the majority of it, did not form unwanted compounds such as La_2O_3, $La(OH)_3$ or $La2(CO_3)_3$ because their characteristic ΔE is too small compared to the gap between our two $3d_{5/2}$ peaks, respectively 4.6 eV, 3.9 eV and 3.5 eV. As there was no quantitative literature on the subject of La-doped barium titanate XPS measurements, we also used data acquired by R.P. Vazquez [59] from another perovskite ($La_{1.85}Ca_{0.15}CoO_3$), that showed a larger ΔE, 5.3 eV, than the previously mentionned La compound, as a base reference for the energy split. Even this much larger ΔE seems too small to fill the gap in our data.

Considering the graphs shown in **Figure 4.7**, it is reasonable to postulated that there is a large binding energy split of the $La3d_{5/2}$ in a $BaTiO_3$ environment, estimated at 5.8 eV within our high-noise data. As explained in section 2.5, this split is caused by the transfer of an electron from the oxygen to the lanthanum f orbital. In our La-doped $BaTiO_3$ structure, the lanthanum replaces barium in the central site of the lattice. The titanium and oxygen atoms share a strong covalent bond while the barium is weakly linked to the oxygen atoms by an ionic bond. As the lanthanum takes the place of the barium, the bonding with the oxygen doesn't drastically change and stays of an ionic nature. Consequently, for an oxygen's electron to transfer to the lanthanum f orbital, it needs to be extracted from the extremely strong titanium-oxygen covalent bond. It is a rational hypothesis that the required extra energy is displayed in the XPS spectra as a large $La3d_{5/2}$ ΔE split. While this has not been properly discussed in the XPS literature, it would be a

useful tool to further analyze the binding of lanthanum or any other element used as a dopant in a $BaTiO_3$.

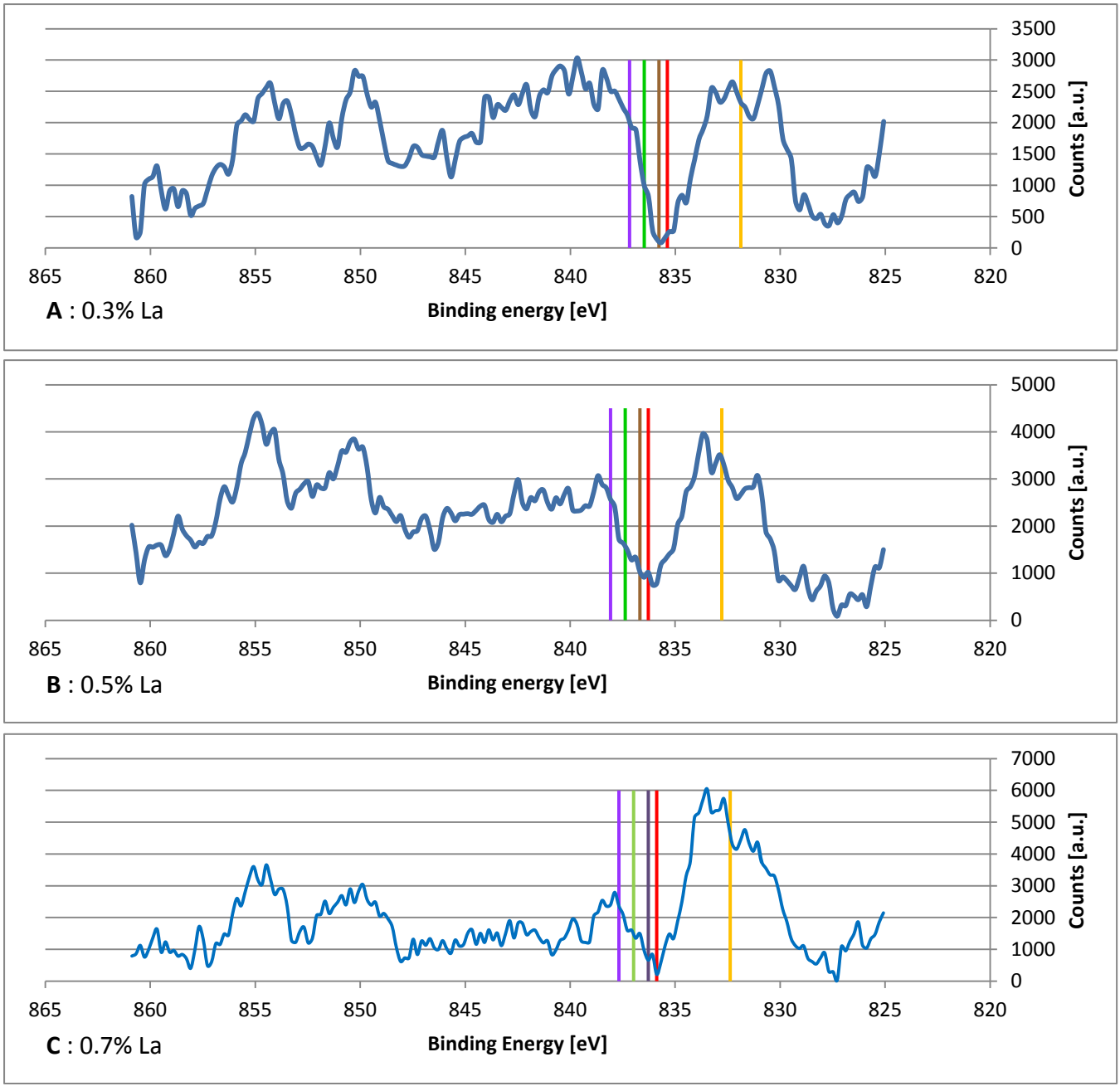

Figure 4.7 : Lanthanum XPS spectra of (A) D1 (B) D2 (C) D3 samples with $La3d_{5/2}$ peaks analyzed and compared to known binding energy gaps from various compounds. From right to left : (orange) half-width binding energy of $La3d_{5/2}$ f^0 peak ; f^0 BE + ΔE from (red) $La2(CO_3)_3$ - 3.5 eV, (brown) $La(OH)_3$ - 3.9 eV, (green) La_2O_3 - 4.6 eV [42] and (purple) $La_{1.85}Ca_{0.15}CoO_3$ - 5.3 eV [59].

4.4 Profilometry

Once a certain amount of practice was acquired, manual screen-printing became very efficient as it enabled the rapid creation of samples suitable for analysis. This process required printing each layer of the devices by hand. However, due to this manual process, the dielectric surface was not expected to be very smooth. Such an increase in the surface roughness may cause an increase of the top conductive electrode surface area. This would result in a higher number of charge accumulated when the device acts as a capacitor. Since the thickness used in the permittivity calculation is determined by the average of the top interface height, where the capacitor samples are considered to be perfectly flat electrodes, the resulting dielectric constant is expected to be slightly higher than it is in reality. This affects all samples in an equal manner (all samples having been produced with the same method) and is not a major concern for this study that is comparative in nature.

The profilometry measurements on the manually printed dielectric layers showed a high level of roughness as expected. **Figure 4.8** highlights the difference between the roughness of manually and commercially printed samples. The commercial samples show, on average, variations in thickness of slightly more than 1 µm for a 6 µm thick films and the hand-printed samples show variations in thickness of about 10 µm for 70 to 110 µm thick films. The film thickness is mainly affected by the printing sequence. 8 samples created less than a minute apart from each other and with the same paste can go from 70 microns to 110 microns because of the curing on the ink with time. In terms of efficiency, it is always preferable to have a thinner dielectric layer for devices such as ours to obtain a better capacitance, as described in chapter 2. However, this project was conducted in a comparative manner since the goal was not to obtain the absolute best electroluminescent device, but to instead study the influence of the dielectric

material on the luminescence in a reproducible way. To attempt the former would have required the synthesis of very large amounts of material in order to use a commercial screen printing apparatus. The thicker devices also have the advantage of lowering the risk of a short-circuit in the device, which would drastically affect the performance of the device.

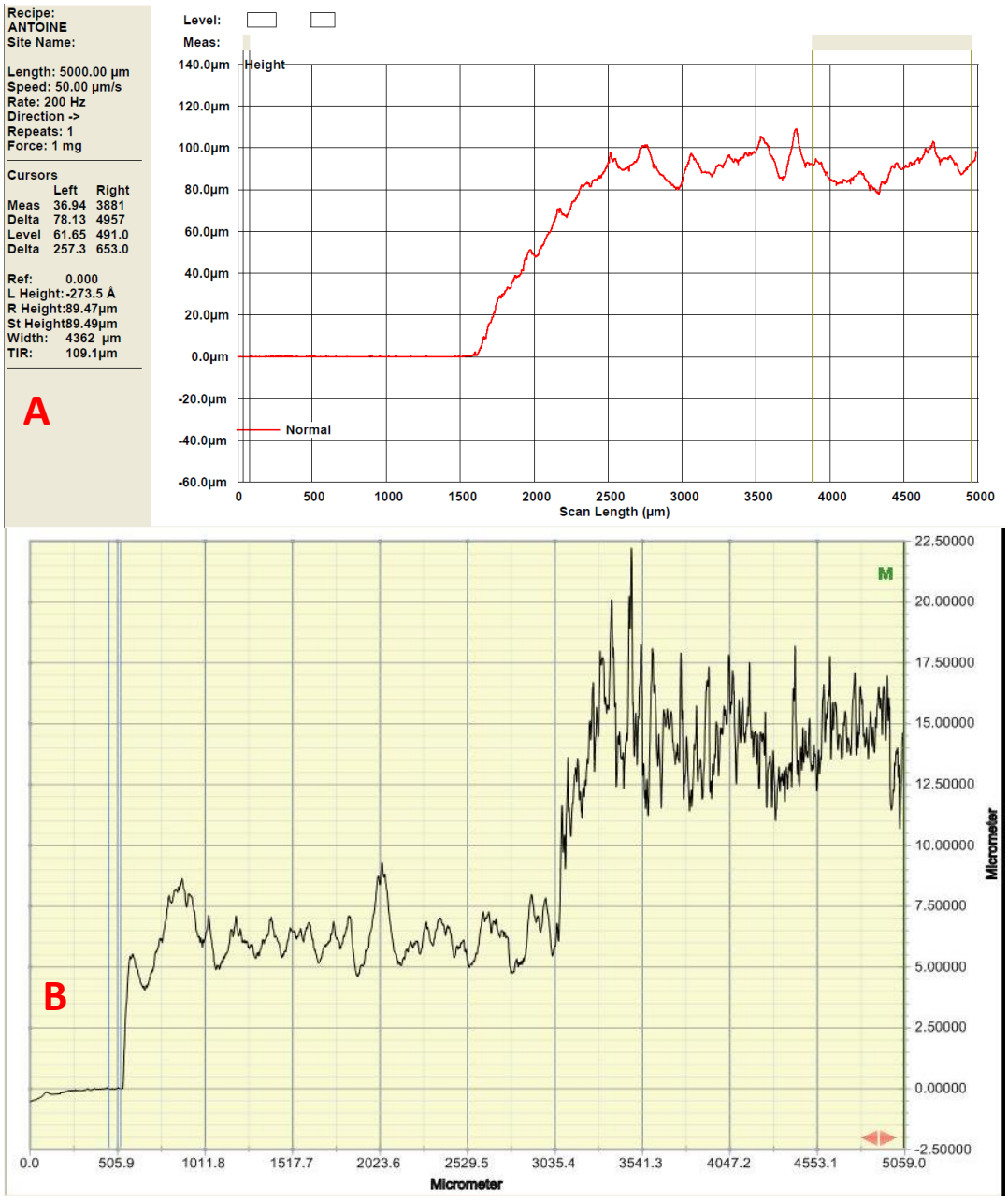

Figure 4.8 : Examples of profilometry measurements. A : sample from the U2 series (University of Toronto) B : first printing tests with a commercial printer, with U0 powder (University Laval)

The thickness of all 46 samples prepared for dielectric measurements - without ZnS - was measured since it can change significantly from one sample to the next during the printing process. To facilitate the profilometry measurements, the data was acquired when the samples consisted only of the conductive plastic substrate with a printed dielectric layer, before the silver was applied. It was deemed unnecessary to do these measurements on the 17 complete devices because the dielectric is sandwiched between the phosphor and the silver. It would have required the profile measurements of the phosphor layer to be recorded first, followed by the printing of the dielectric layer and the profile measurements of this second layer. Other approaches such as imaging of the cross-section of the device using the SEM would have offered a direct measurement, but this would only give a one-dimensional point of view, whereas the profilometry measurements are taken at different locations on the sample. A more precise method would have been to take many "slices" of each samples and look at their cross-section to obtain a definite 3-dimensional perspective of the dielectric layer. This would, however, be highly impractical and require a considerable amount of time for each sample, completely destroying all samples in the process. The dielectric constant was therefore not calculated on the luminescent samples.

At first glance, the error on the thickness values is surprising as it is smaller than the variations on a single profile. The exact uncertainty on a single measurement is difficult to determine and changes every time. The error was established as the standard deviation from three measurements – the average thickness. Additionally, since the results were usually stable, the calculated deviation stayed small compared to the total thickness.

4.5 Impedance Spectroscopy Measurements

The samples printed as capacitors have an extremely high electric resistance and it is impossible for the VoltaLab system to measure the impedance properties on a very large frequency spectrum. The frequency ranged between 500 Hz and 10 kHz, which only created a small arc of the characteristic RC-circuit semi-circle in the Nyquist plot, **Figure 4.9**, but enough to analyze the capacitance and simulate a full plot from the equivalent circuit with resistor and capacitor values estimated by the EC-Lab software. We can see in **Figure 4.9** that the data fits the model relatively well in the Nyquist plot. It is important to mention that the capacitance values used in the dielectric constant calculations are the ones directly measured experimentally and not the overall capacitance estimated by the computed model.

The Kramers-Kronig relations (mentioned in the Chapter 2) were not applicable to the data obtained here because it is necessary to have completely closed semi-circles in the Nyquist plot, to verify the coherence of the data with this method. Using them on the extrapolated data from the equivalent circuit wouldn't be relevant as the simulated plot always gives a perfectly coherent semi-circle non-representative of the real acquired data.

From the impedance data, we also created a Bode plot for each sample, **Figure 4.10. s**Similarly to the Nyquist plot, the experimental Bode plot is only a small fraction of the full curve it would normally be for a wider range of frequencies. By observing how well the experimental data fitted the simulated model data on both the Nyquist and Bode plots, we were able to conclude that the chosen equivalent circuit is satisfactory for our device. The phase angle fitted the model moderately poorly, possibly due to the difficulty in obtaining a clear picture of this parameter with a restricted range of frequencies.

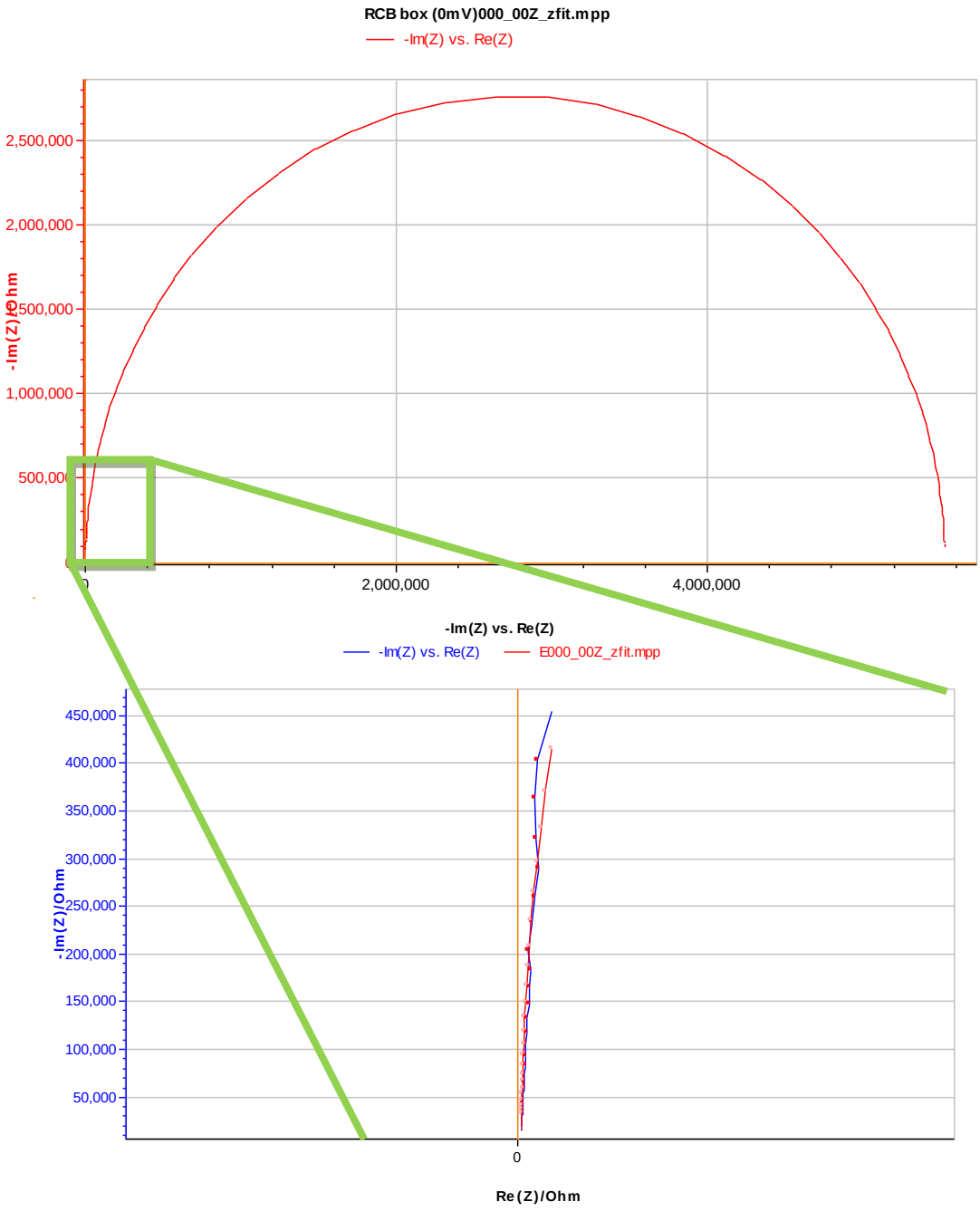

Figure 4.10 : Nyquist plot of a Lan05 sample, experimental data in red and simulated data in blue. The whole red semi-circle is created by the software using the estimated equivalent circuit elements from the short experimental blue line. The green square represents the small portion of the full semi-circle represented in the experimental data.

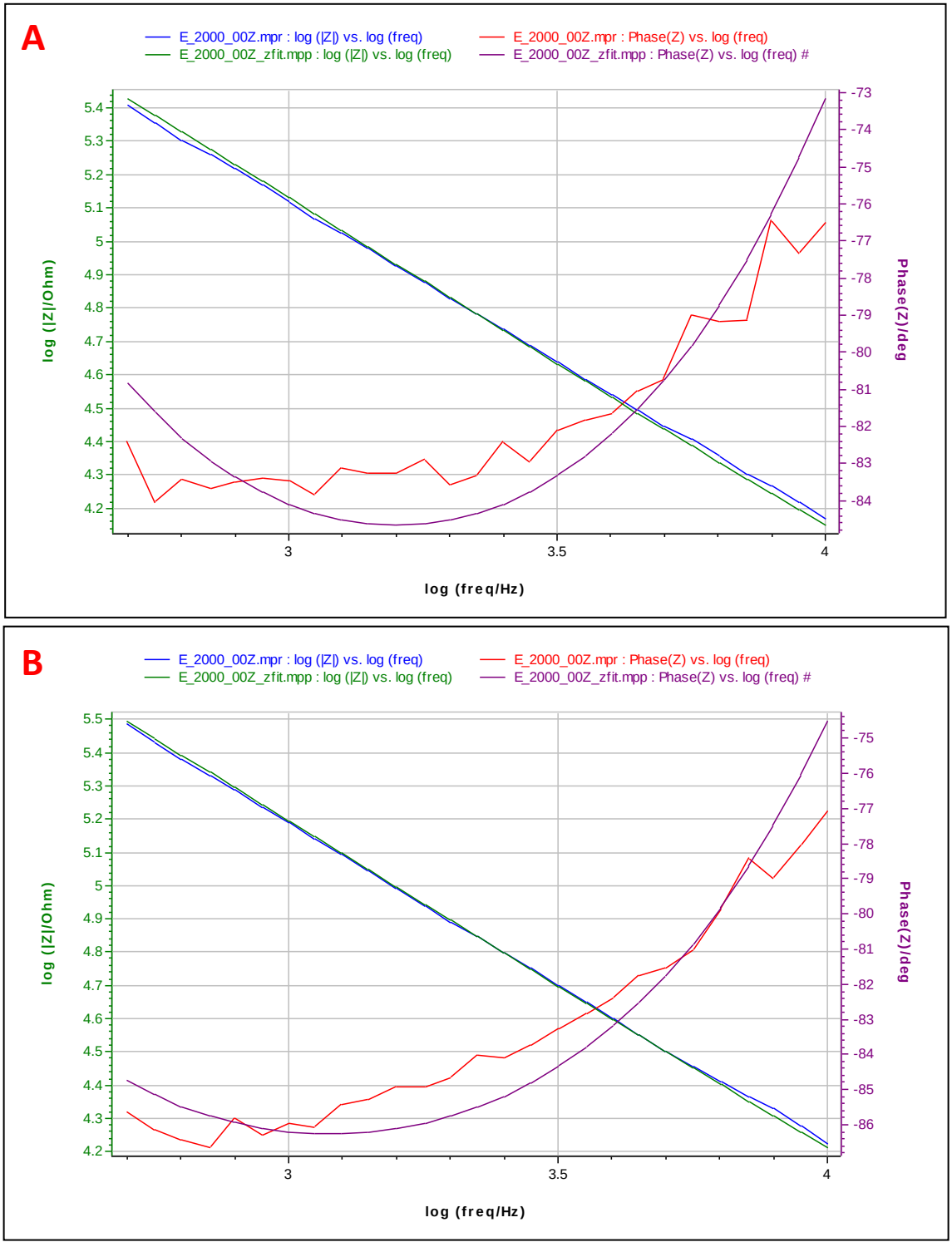

Figure 4.10 : Characteristic Bode plots for samples in series : D2 (A) and Com (B). Experimental data in blue (logarithmic impedance) and red (phase), and simulated model data in green (logarithmic impedance) and purple (phase).

The capacitance of a sample was determined by averaging the capacitance between the frequencies of 500Hz to 10kHz, 27 entries were acquired in total. Once the individual capacitance and dielectric layer thickness are known, the simple calculation to derive the dielectric constant can be carried out. The ε for all the samples printed from one series, such as U1 or D1, are averaged and compared. The histogram in **Figure 4.11** shows these comparisons between the different syntheses**.** Compared to other studies [14, 17, 25] on the dielectric constant of $BaTiO_3$, the ε obtained here is very low since it is a characteristic of the material layer which consists of a mixture of the experimental powder and the epoxy paste.

To determine the impedance spectroscopy error, a series of 10 measurements were performed on the same samples. Between each measurement, the sample was removed and repositioned in the set-up. This combined the instrument's overall error with the slight variations in connectivity that could occur between the silver layer and the steel wool in the set-up. The error for the dielectric constant consists of the combination of the relative error of the thickness data and the relative error of the capacitance. Three different error calculations were tested for the ε value to determine the largest uncertainty on the result. The standard deviation on the individual dielectric constant value for each sample was determined by giving a relative uncertainty of 5 % to 7 %. Partial derivative error calculations were done using the capacitance equation, see **Appendix B** for an example, and between 0.4 % to 0.6 % of uncertainty was found. Finally, using the pre-determined errors for the capacitance per area and thickness, mentioned previously in this chapter, the maximal and minimal possible values of ε were calculated and the uncertainty Δε was determined by the relationship $\varepsilon_{max} - \varepsilon_{min} = 2\Delta\varepsilon$. This showed the largest possible error varying amongst the samples between 6% and 8%, on the permittivity of the samples. The error bars in all the ε histograms represent this value.

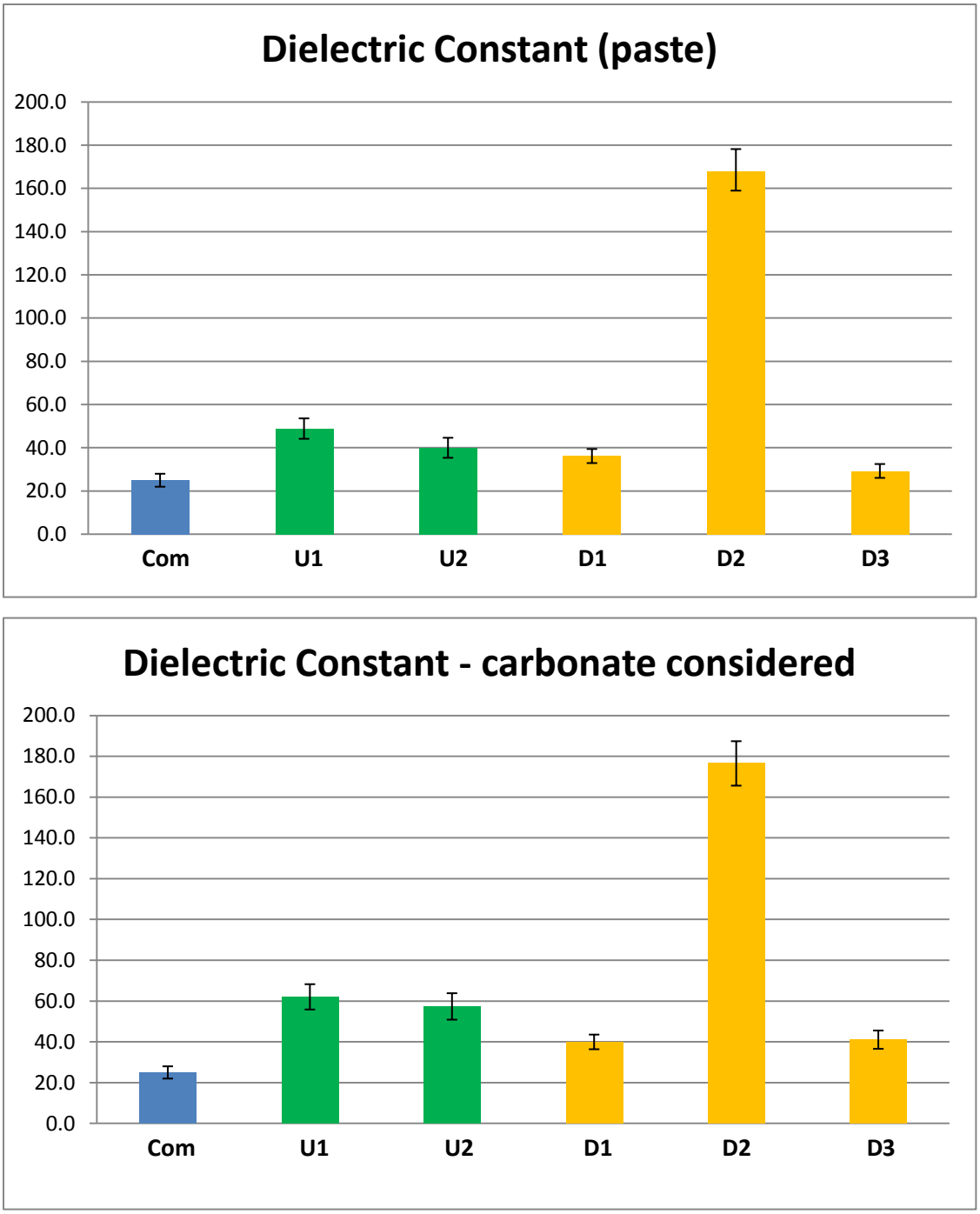

Figure 4.11 : Average dielectric constant for each synthesis. Top, direct calculations from the impedance and thickness measurements. Bottom, compensation for pure barium titanate dielectric constant with the ratio of carbonate and titanate in the samples taken from peak intensities in the X-Ray diffraction spectra. Table available **Appendix A.**

A clearly better candidate stood out among all the produced material : the D2 powder more than doubled the ε of the second best dielectric. It directly showed the expected behavior of doped samples, where a maximum ε was attained with the D2 concentration and decreased in efficiency at a lower or higher concentration. Un-doped samples displayed unexpected results as the U1's ε average value is the same as U2's within experimental error. The difference in $BaCO_3$ concentration between the samples, as discussed in the X-Ray analysis section, have a definitive effect on the dielectric efficiency of the material. Compared to the titanate, the carbonate is not ferroelectric and is thus significantly less responsive to electric fields. Even a small concentration of carbonate would cause a drop in the amount of charges accumulated during the capacitive functions of the device. The impedance measurements then undervalue the relative permittivity results that can be attributed to pure barium titanate particles. To correct this effect and estimate the properties of pure $BaTiO_3$ particles, the relative permittivities were divided by the ratio of the peak intensities of barium titanate divided by the total amount of titanate and carbonate in the material (T/[T+C], where T is titanate and C is carbonate) indicative of the powder's purity, **Table 4.3**. Using this product when comparing the different series of dielectrics puts all the data on a (simili) equal level as it shows what all the measurements would have been for pure $BaTiO_3$, **Figure 4.11** (bottom)**.** No change were brought to the Com data since the powder is commercially acquired and assured a good level of purity. We can see that from this point of view, the data for D1 and D3 becomes practically the same, which still leaves D2 as a clear maximum. U1 and U2 also remain similar, giving the same dielectric constant result within the error bars.

From our data we conclude that there is no net difference of permittivity associated with the change in the concentration of acetyl acetone during the preparation process, as the results

are the same based within error. It is however clear that the addition of lanthanum in the sol-gel process is highly beneficial at the right concentration although it cannot be assigned unequivocally to a size effect and/or doping effect.

4.6 Photometry Measurements

The electroluminescence of all printed samples with phosphor was measured three to four times, so to obtain valid data using the instrument's 3 % uncertainty as the error. The deviation in the data obtained was typically lower than that 3 %, which explains the error value on our results. The data was consistent with the dielectric results for the doped samples: the higher-ε samples emitted more light, tables and histograms are grouped in **Figure 4.12**.

The combination of the results of the impedance spectroscopy and the photometry showed the electroluminescence to be inversely proportional to the resistance, thus confirming that it is affected by the resistance of the device. To observe all data on the same level of resistance, the pure luminescence of each sample was multiplied by its DC resistance which gives a result in Watts·Ohms. The exact relationship between the resistance and the luminescence is, however, not precisely clear for such devices. Nevertheless,, it was decided that this process enables an observation of the relationship between the luminescence and the synthesis method, that is closer to reality which eliminates most of the problems caused by the non-uniformity of the hand-printing.

The drop in luminescence from U1 to U2 is unexpected, considering the dielectric constant results. Although their dielectric constant is the same within the error, the significant difference in luminescence represents a clear gap in efficiency between the samples. This gap is difficult to explain apart from a possible technical problem in the printing process. The X-Ray

analysis showed that the U2 powder contained more $BaCO_3$ (21,5% for U1 and 30,1% for U2) which could affect the electroluminescence process, but should have shown a capacitance deficiency in

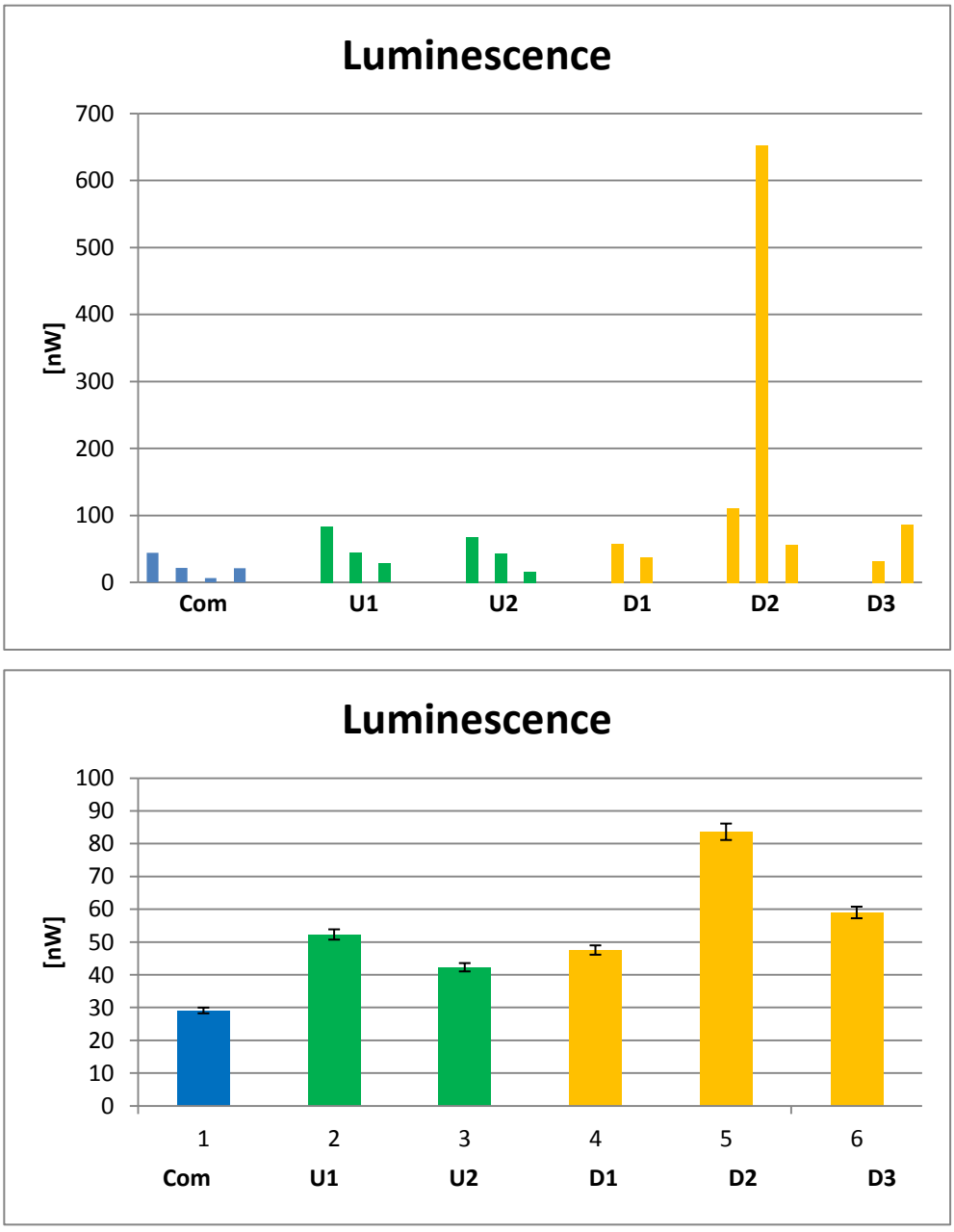

Figure 4.12 : Top : Light intensity, in nW, displayed by all electroluminescent samples. Bottom : Average, and its error, for each synthesis. The average for D2 does not take into account the result for the extremely efficient sample and still shows a significant superiority. Table available in **Appendix A**

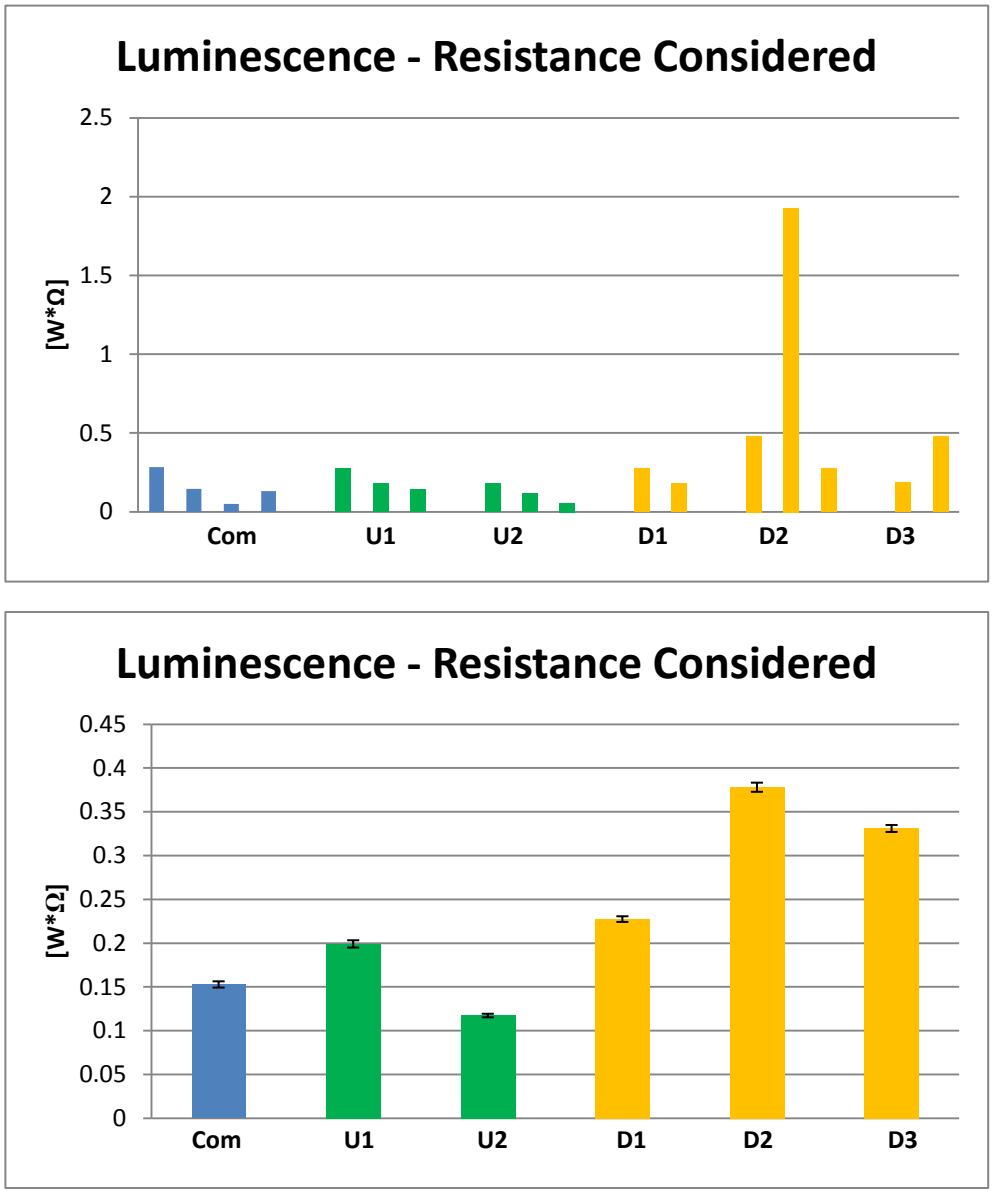

Figure 4.13 : Top : Light intensity, in W*Ω, displayed by all electroluminescent samples. Bottom : Average, and its error proportional to the pure luminescence data, for each synthesis. The average for D2 does not take into account the result for the extremely efficient sample and, again, is the better powder, but by a smaller margin than before.
Table available in **Appendix A**

impedance measurements. Also, when comparing the luminescence of the undoped samples on the same level of resistance, as shown in **Figure 4.13**, we can see that the gap between the two becomes even greater. The difference in $BaCO_3$ concentration is an important point to consider but doesn't appear to be enough to explain the 19,1% difference in the luminescence data, not to mention a 41,1% difference with the resistance is considered, to compensate for the devices' imperfections. The change in tetragonality in relation to the size of the particles, which follows the experimentally verified core-shell model, allegedly affects the dielectric constant as established in the litterature [17], but the change of phase could not be verified by the X-ray diffraction so no conclusions should be drawn ont his matter based on this study.

One sample, containing 0.5% La doped $BaTiO_3$, performed extraordinarily well compared to the others. The luminescence emitted was 755% brighter than the most efficient sample made with the D3 powder and even 590% brighter than the second best device made with the same D2 powder. The device was made exactly the same way and at the same time as the others with the D2 powder. It was confirmed that this result was not due to a glitch of the photometer or some exterior stimulus as the results shown in **Figure 4.12** are the averages of four non-consecutive measurements, where the set-up was reassembled twice. Its resistance was considerably lower than the others in D2, but nothing out of standards for such devices.

This exceptional result is not only important for this study, but could have a dramatic effect on the electroluminescent industry. Safety standards are a major factor in the commercialization of electronic products and the result in this thesis shows the possibility of obtaining a bright luminescent display fed by a much lower input of electrical energy, which lowers the risks, or more precisely the necessary protective precautions for contingencies in the use of this product. With additional research that focuses on the manufacturing process and the

specific dopant concentration, the screen-printed device could be part of the major candidates in the search for a bright and energy-efficient technology, among organic electroluminescent devices [60] [61] and quantum dot electroluminescent devices [62].

4.7 New Series of Samples

Because of the extreme electroluminescent properties of our D2 sample as well as to obtain a better statistical certainty on our results new powders were synthesized with a 0.5% La (D2.1) and a 0.7% La (D3.1) concentration of dopant. This enabled a comparison between the dielectric and luminescent data on similar, new samples. A total of 14 new samples were made, one half for dielectric constant observations and the other half for luminescence testing. These were prepared with the same process that was previously employed to prepared our other samples. By X-Ray diffraction analysis, our new D2.1 powder showed a percentage of 91.3% of barium titanate with the remaining being barium carbonate. This value is close to the 95,1% previously obtained for the other D2 sample. There was a large improvement in the quality of the material for the D3.1 powder with 87,5% barium titanate versus 71.3% for the previous synthesis (D3). The X-ray peaks can be seen in **Figure 4.14**, where the D2.1 spectrum is superimposed on the D3.1 spectrum. The dielectric constant results seen in **Figure 4.15** show a similar pattern to those obtained wuth D2 and D3, but with a much smaller difference between D2.1 and D3.1. We see that the dielectric doped with 0.5% Lan still is advantageous by a small margin and we can confirm that this concentration is optimal for a barium titanate layer used in a capacitor-type device.

The major difference between the dielectric constants of D2 and D2.1 (respectively 155.5 and 37.2) could be explained by the change in the resistance of the samples measured by

impedance spectroscopy. The D2.1 non-luminescent samples have resistances that are three times

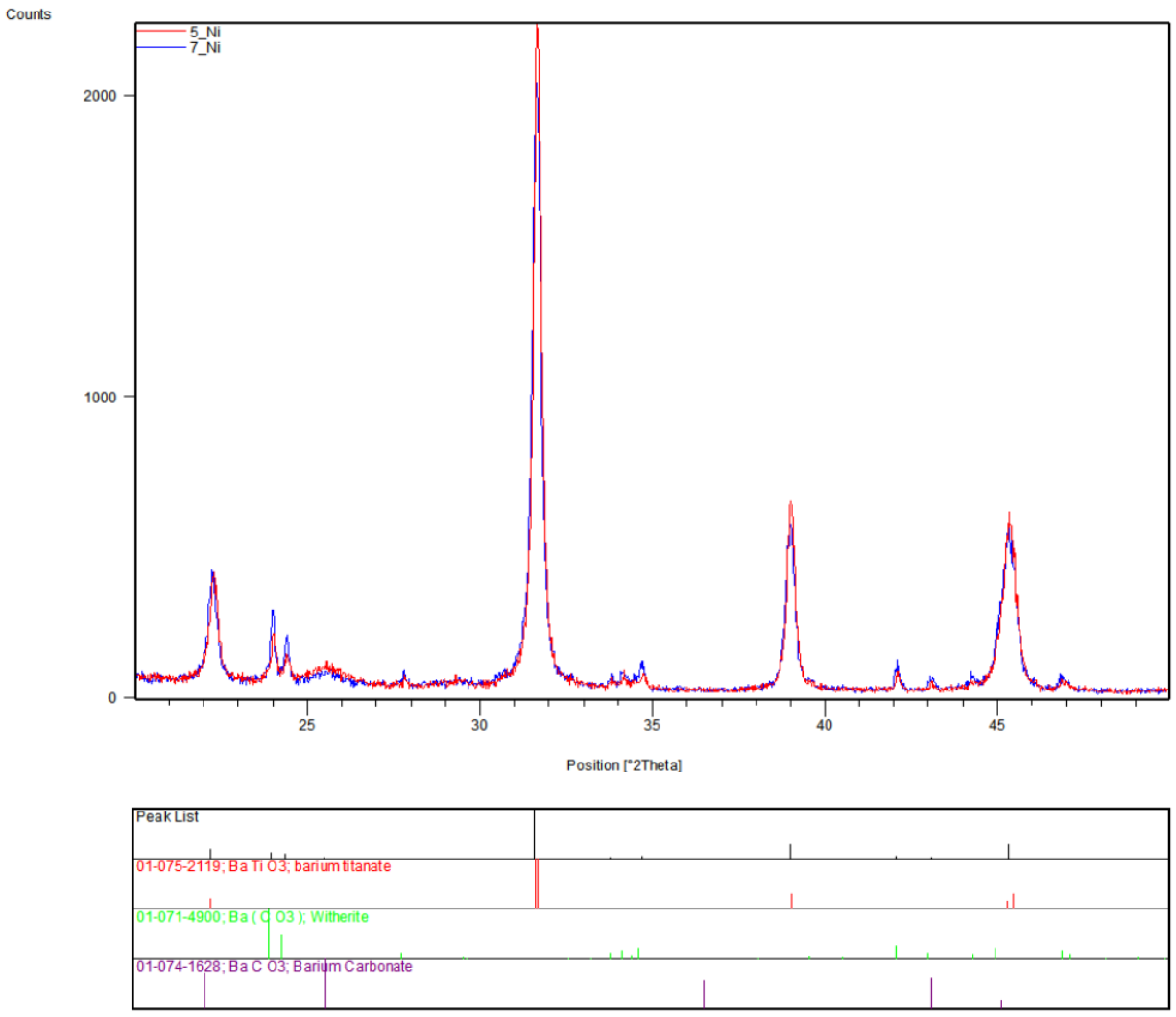

Figure 4.14 : X-Ray spectra of D2.1 (5_Ni red line) and D3.1 (7_Ni blue line).

higher than the D2 samples, with an average resistance of 6.7 ± 0.2 MΩ versus 2.2 ± 0.2 MΩ. Similar observations are made on the D3.1 and D3 samples, with 6.6 ± 0.2 MΩ and 2.2 ± 0.2 MΩ, respectively. Although the electrical resistance is not part of the capacitance equation, such a consistent difference demonstrates a change in the internal structure of the dielectric layer that could result in an alteration of the measured ε. Therefore, we cannot calculate a total average of the results of D2 and D2.1 or D3 and D3.1 together, but we can establish that the material with a 0.5% concentration of La shows a stronger dielectric behavior than with a 0.7% concentration. By extension, we can conlude the 0.5% La material also has a stronger dielectric constant than the one with 0.3% La, since we saw a replicated behavior of the material with the new samples and it can be assumed that the results would have been consistent.

The luminescence measured on the new samples showed quite similar results to the previous samples, although we did not witness another extraordinarily bright example (which is not to say that it was an anomaly unrelated to the rest of the samples, as explained later). The D2.1 devices were clearly brighter than the D3.1 ones as shown in **Figure 4.16**. Overall, the raw luminescence data was lower than with the previous samples, but this seems to be directly correlated with the DC resistance of the samples. The exact relationship is not very clear and does not seem to be discussed in the literature, but we can see a pattern, where as the DC resistance decreases, the luminescence increases. However, there most certainly is a minimal resistance in order to maintain the capacitive behavior of the device. We suggest that an optimal resistance threshold could be found experimentally, in the idea of obtaining an increased output of luminescence given a maintained level of electrical potential. As the exceptionally bright D2 sample had a low resistance compared to the rest of the D2 and D2.1 samples, it might be

possible to correlate the data including the seemingly abnormal result by using an empirical equation that establishes the luminescence as a function of the resistance.

	Carbonate Peak [a. u.]	Titanate Peak [a. u.]	Diel. Constant [ ]	Ratio T /(T + C) [ ]	Diel. C. / Ratio [ ]
D2.1	213	2247	34,0	0,913	37,2
D3.1	292	2052	26,8	0,875	30,6

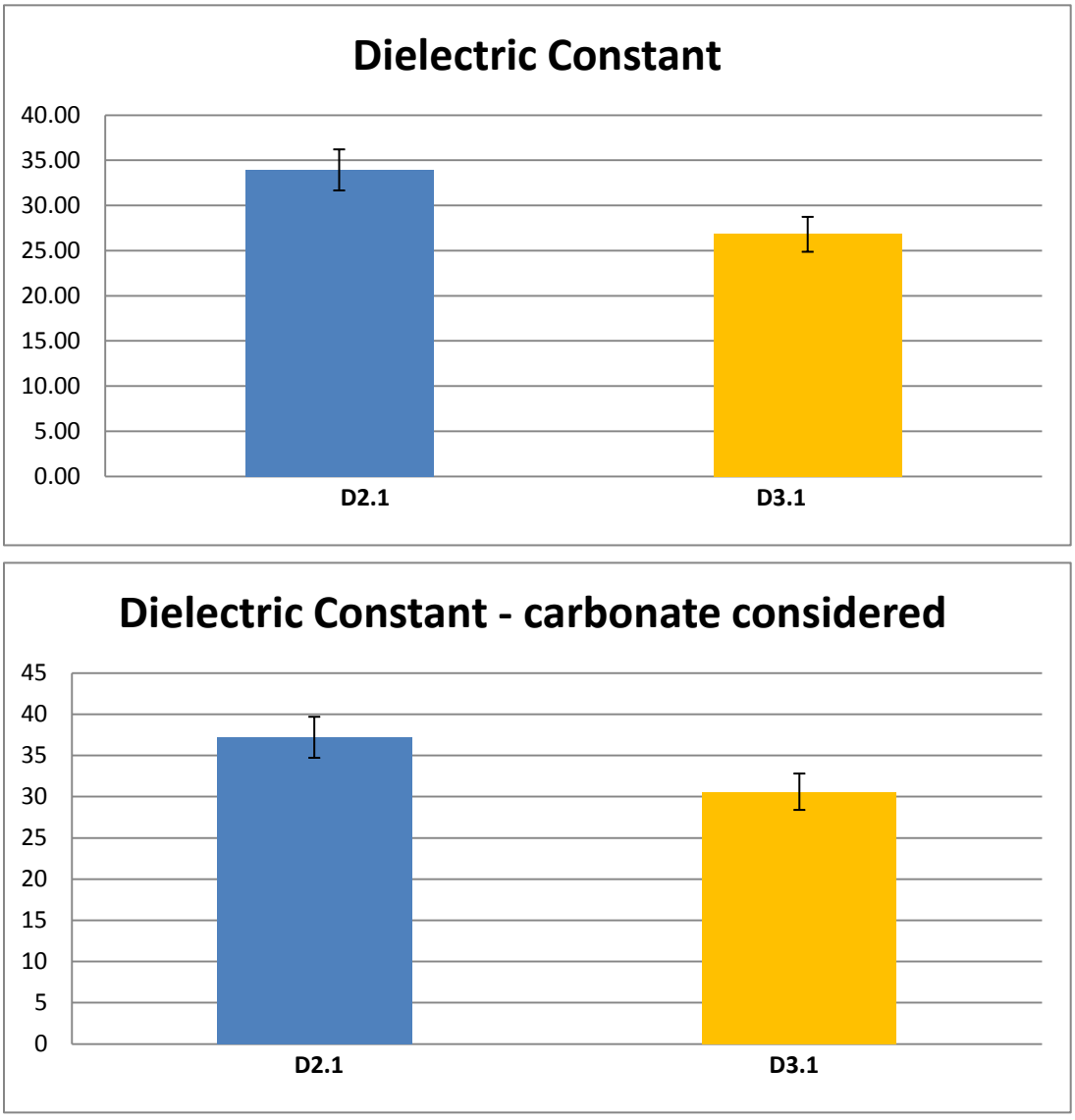

Table 4.3 & Figure 4.15 : A : Intensity of the carbonate and titanate peaks in the X-ray spectra with the ratio of pure titanate in new samples and the dielectric constant proportional to the amount of titanate. B : Histogram of the dielectric constants of the new samples. C : Histogram of dielectric constant with compensation from the ratio of titanate and carbonate in the material.

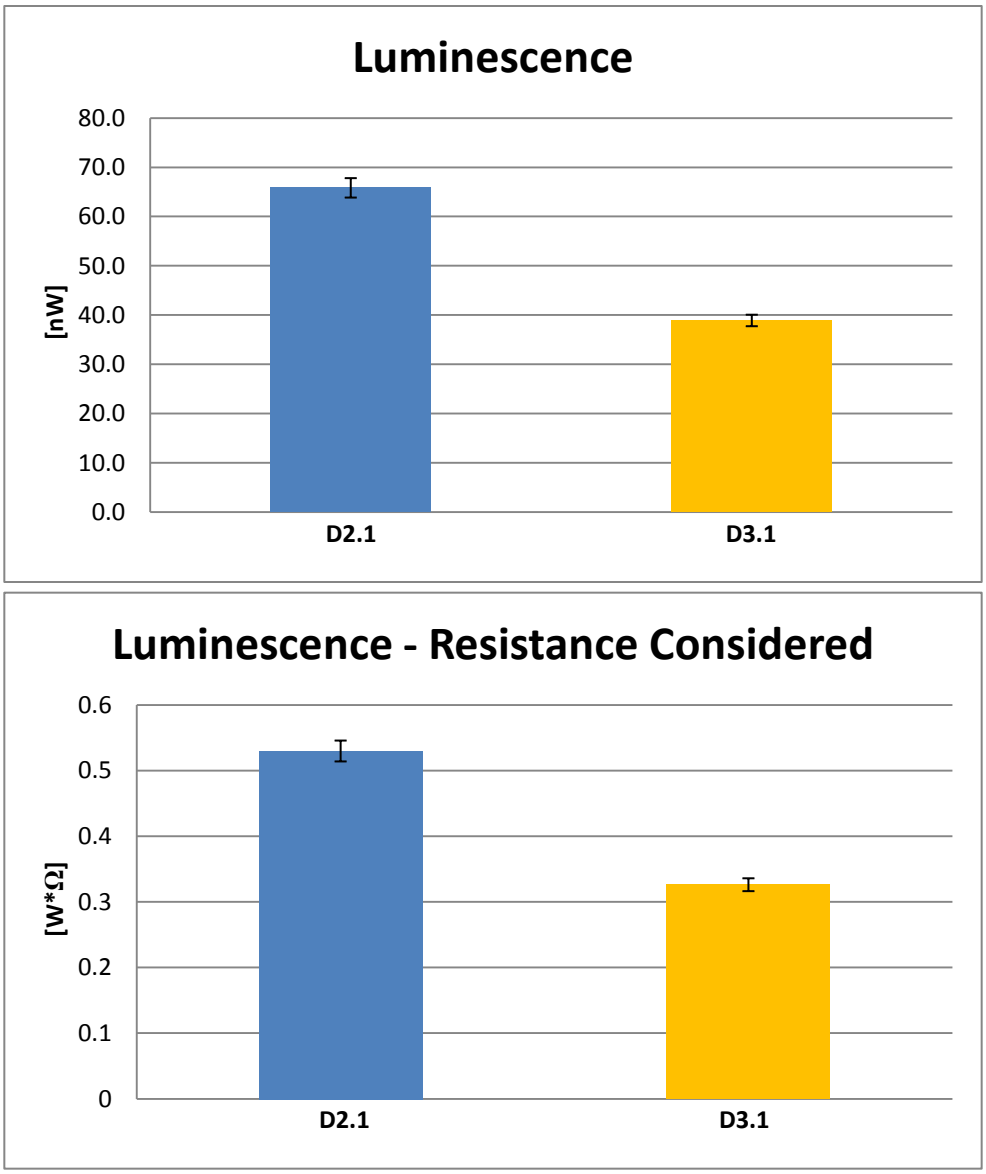

Figure 4.16 : (A) Histogram of luminescent data from new samples (B) Histogram of luminescent data with compensation from DC resistance in the new samples.

Chapter 5 : Conclusion and Future Work

5.1 Conclusion

The objectives of the research presented in this thesis were to synthesize a set of different barium titanate nanoparticle powders, as an intrinsic dielectric or doped with lanthanum, and explore their dielectric properties as well as their effect on electroluminescence efficiency. Two different types of devices were screen-printed for this purpose : a capacitor-like device containing only the dielectric and two electrodes, and a full electroluminescent device where a phosphor layer was added below the dielectric one. The relative permittivity was determined by combining impedance spectroscopy and profilometry measurements while the luminescence data was collected by a sensitive photodetector.

The first step to undertake for this research was to choose the best method with which to synthesize the $BaTiO_3$ particles and conduct several trials to produce good quality material. The sol-gel process was used as it enables the creation of a ceramic material, such as $BaTiO_3$, at room temperature and would normally yield a homogeneous powder since the particles are formed through a self-constructed network. The syntheses of undoped material focused on varying the concentration of acetylacetone thus affecting the size of the particles (97 nm, 99 nm, 103 nm). However, it was impossible to extract relevant information from these experiments because the results were all within the ± 5-7 nm error range. The creation of Lan-doped barium titanate was attempted with an organic resin process called the Pechini method. This failed and produced mainly barium carbonate. We returned to the sol-gel process but modified it slightly so that the desired amount of lanthanum could be inserted into the product. This process was successful.

X-ray diffraction analysis was done on all the samples to ensure that the $BaTiO_3$ crystals were properly formed, as well as to observe the amount of an inevitable contaminant: barium carbonate. The morphology and size of the samples were observed by SEM, using a spin-coating technique to minimize the agglomeration of particles. Once the test samples were deemed suitable, a synthesis was done on a much larger scale to produce the amount of powder necessary for the printing process. For the doped samples, we acquired EDX measurements to validate the theoretical percentage of lanthanum present in the material, but the uncertainty was too high to distinguish between each synthesis.

Capacitor-like devices and ELDs were prepared by manual screen-printing. The dielectric powder mixed with an epoxy paste created a white ink pressed through a specially designed screen onto a conductive plastic substrate. For ELDs, pure ZnS powder was used in a similar way to print the luminescent layer onto the plastic before the dielectric. For all devices a final silver layer was added to create the electrodes: one contact on top of the non conductive layers and one ring surrounding them directly on the plastic.

Before the silver layer was applied, the thickness of the dielectric layer had to be measured with a profilometer for non-ELDs. It was found that manual printing produced thick layers, between 70 μm and 110 μm, that fluctuated significantly from one sample to the next. This was solely caused by the way in which each sample was printed, pressure and speed, which are impossible to calibrate perfectly when done manually. With years of screen-printing practice, a person could be able to produce a more consistent thickness. The sample surface itself had a high amplitude perturbation, about 10 μm, and the average thickness slightly falsifies the permittivity calculation. We implemented it as if we had a flat interface, but the larger area of the rough surface enables more charges to accumulate on it. The capacitance measured is thus higher

than it should be for a flat interface, which gave us a slightly stronger final ε than it is in reality. However, it is too complex to calculate in the context of this project.

XPS measurements were done on the La-doped $BaTiO_3$ powder. They confirmed the insertion of lanthanum in the crystal structure of $BaTiO_3$. The data also showed a very large gap between the two binding energies of the the $La3d_{5/2}$ orbital split peak. We realized that this gap in energy was not discussed in the literature and a hypothesis was advanced related to the process in play. This gap is form by an oxygen's electron that is transferred to the lanthanum f orbital. The electron shared is pulled by a very strong titanium-oxygen covalent bond. It is thus a rational hypothesis that the required extra energy is displayed in the XPS spectra as a large $La3d_{5/2}$ ΔE split

The final step for the capacitors was the impedance spectroscopy measurements. Because of the highly resistive nature of all the samples, only a small fraction of the full Nyquist or Bode plots (which are characteristic of the representative equivalent parallel RC circuit) could be measured. However, the data acquired from 500Hz to 10kHz were sufficient to obtain an adequate capacitance, especially relevant for the electroluminescent devices that run at a frequency of 1kHz. The equivalent circuit capacitance and resistance estimated by the software made it possible for us to simulate plots from the model. The comparison of the experimental and simulated data on the Nyquist and Bode plots revealed that the model was accurate for our devices. The dielectric constant was later calculated from the impedance and profilometry results, and were adjusted considering the carbonate ratio in each powder. We found that the values for the undoped samples U1 and U2 did not vary significantly. The technically smaller particles showed a slightly higher ε than the larger ones, but just as with the size measurements, the difference fits inside the error bars. As such, no conclusion can be derived from this data.

Unexpectedly, the doped samples D1 and D3 gave worse results than the undoped particles. However, a very strong value for D2's ε was observed. It was almost three times higher than the second best of all samples, **Figure 4.11**. The commercial $BaTiO_3$ clearly remained with the lowest ε.

When the ELDs underwent the photometry measurements, they showed a similar pattern to the dielectric constant results. The D2 samples had the brightest luminescence and one of them even had an extraordinary output of light intensity. Sadly, no proper explanation was advanced as to why this device was so efficient. Such a result is of high importance and an investigation using complimentary equipment and a efficient printer is proposed in the next section. The various series of $BaTiO_3$ displayed an average luminescence, in increasing order of : Com, U2, D1, U1, D3, D2. The resistance of each ELD was measured by impedance spectroscopy by using the Nyquist plot of its software-calculated equivalent circuit. We found that a decrease in resistance consistently resulted in an increase in luminescence and we combined the data in an Ω*W product to examine the luminescence of devices on the same level of resistance. This slightly changed the order of increasing performance as it then was : U2, Com, U1, D1, D3, D2. D2 remained the significantly better candidate for the device and all doped samples were then technically more efficient than the undoped samples.

We were successful in this research as we showed that a synthesized dielectric made in our lab could be implemented in a hand printed ELD that emitted extremely bright light. The special D2 sample was even brighter than similar devices from other studies that were made with a sol-gel processed, doped dielectric which were printed using high quality, automated equipment. This opens the way for a drastic decrease in electric energy consumption in the electroluminescent industry.

New doped material were synthesized again for a statistical confirmation of the data. Two powders were studied again with concentrations of 0.5% (D2.1) and 0.7% (D3.1) of La. Although we could not recreate a sample with a luminescence of the special D2 sample, the general pattern of the doped samples was seen again. We observed a stronger ε for the D2.1 than for the D3.1 but by a smaller margin than before. The D2.1 samples also showed a brighter emission of light than the D3.1. These new series of samples confirmed that the 0.5% La concentration was optimal for the increase of the dielectric constant in barium titanate.

5.2 Future Work

The remarkable and surprising luminescence result for the D2 sample could potentially be of great importance for the field of electroluminescence, the new D2.1 samples did not . The most essential work to be done after this project is to verify that it can be reproduced. A very large scale synthesis should be done to enable the use of a commercial printer, which needs a large amount of material to start the process but consumes very little once the machine is saturated with ink. The creation of many high quality ELDs with a 0,5% lanthanum concentration would be very interesting and we could then directly compare the results with the industrially manufactured devices. A stimulating goal would be to bring down the voltage needed for a consistent light, from the 300 V currently used to a value closer to 80 V, a safety standard threshold that would highly facilitate commercialization. A study on the influence of DC resistance in the device would be essential to optimize the process of luminescence with alterations that would probably lower the manufacturing cost. In our study, the printing was done by hand, so the thickness of the different layers varied significantly for each sample. An industrial printer that uses a pre-determined thickness would change this uncertainty into a parameter that could be fine-tuned to research the effect of resistance on luminescence. A

theoretical study looking at this phenomenon would be a perfect complement and would enable a better understanding of the role of power loss and structural changes of the dielectric layer with regards to the output of luminescence.

Another path in the continuity of this research would be to study pellets of pure, compressed $BaTiO_3$, which would eliminate the resin used to prepare the ink. This would remove the variables brought by the manufacturing process that are not directly related to the properties of the dielectric particles but affect the device's final output. This could facilitate the study of the effect of temperature on our doped samples, an important aspect for the durability and efficiency of the material. Similar research has been done on $BaTiO_3$ and other dielectrics and these results could be easily compared with the literature.

Finally, a different and important approach to this research is the theoretical examination of barium titanate's crystal structure through computational studies of its tetragonality, and the suggested core-shell structure's effect on permittivity. These avenues are of great interest for a deeper understanding of the material's behavior. We have already computed the properties of the cubic and tetragonal structure of barium titanate as a base reference with the SIESTA computer program [63, 64]. The model and input file for a 1-dimensional study of the core-shell structure have been put together, though the files need to be optimized. With these computations, and possible further 2-dimensional and 3-dimensional trials, we could have a clearer picture of the combining effect of the tetragonal and cubic lattices on the global electronic structure. If this core-shell is found to be optimal, specific research should be done to discover the best cubic/tetragonal ratio.

Appendix A
Data Tables for All Screen-Printed Samples

Table A-1 : Commercial and Un-Doped Samples.

		C [pF/cm^2]	C [F/m^2]*	d (µm)	d (m)**	Relative ε	Average ε
Commercial	Com-A	336,84	3,37E-06	64,00	6,40E-05	24,35	25,0 ± 3,0
	Com-B	406,05	4,06E-06	44,83	4,48E-05	20,56	
	Com-C	351,89	3,52E-06	64,25	6,43E-05	25,54	
	Com-D	370,73	3,71E-06	64,05	6,41E-05	26,82	
	Com-E	358,72	3,59E-06	59,30	5,93E-05	24,03	
	Com-F	377,20	3,77E-06	64,83	6,48E-05	27,62	
	Com-G	416,58	4,17E-06	55,25	5,53E-05	26,00	
	Com-H	355,66	3,56E-06	62,20	6,22E-05	24,99	
71,0% Acac	U1-A	296,29	2,96E-06	100,30	1,00E-04	33,56	48,7 ± 4,5
	U1-B	638,83	6,39E-06	70,80	7,08E-05	51,08	
	U1-C	1104,47	1,10E-05	78,20	7,82E-05	97,55	
	U1-D	816,21	8,16E-06	79,20	7,92E-05	73,01	
	U1-E	474,92	4,75E-06	90,50	9,05E-05	48,54	
	U1-F	548,75	5,49E-06	71,50	7,15E-05	44,31	
	U1-G	474,21	4,74E-06	83,50	8,35E-05	44,72	
	U1-H	429,02	4,29E-06	93,50	9,35E-05	45,31	
49,7% Acac	U2-A	347,06	3,47E-06	92,30	9,23E-05	36,18	40,1 ± 4,7
	U2-B	411,48	4,11E-06	84,20	8,42E-05	39,13	
	U2-C	385,36	3,85E-06	91,80	9,18E-05	39,96	
	U2-D	789,57	7,90E-06	73,20	7,32E-05	65,28	
	U2-E	341,17	3,41E-06	90,50	9,05E-05	34,87	
	U2-F	363,99	3,64E-06	81,50	8,15E-05	33,51	
	U2-G	322,23	3,22E-06	99,50	9,95E-05	36,21	
	U2-H	327,01	3,27E-06	97,00	9,70E-05	35,83	

* Error on *C* is 0,1% of the measured value

** Error on *d* is 4 µm

Appendix A
Data Tables for All Screen-Printed Samples

Table A-2 : Doped Samples

		C [pF/cm^2]	C [F/m^2]	d (µm)	d (m)	Relative ε	Average ε
0,3% La	D1-A	321,62	3,22E-06	110,00	1,10E-04	39,96	41,1 ± 3,3
	D1-B	327,97	3,28E-06	107,00	1,07E-04	39,64	
	D1-C	322,78	3,23E-06	114,25	1,14E-04	41,65	
	D1-D	346,78	3,47E-06	102,53	1,03E-04	40,15	
	D1-E	315,73	3,16E-06	116,85	1,17E-04	41,67	
	D1-F	351,54	3,52E-06	115,9	1,16E-04	46,02	
	D1-G	351,54	3,52E-06	96,65	9,67E-05	38,37	
	D1-H	120,48	1,20E-06	64	6,40E-05	8,71	
0,5% La	D2-A	1833,93	1,83E-05	108,5	1,09E-04	224,74	167,83 ± 11,7
	D2-B	1675,05	1,68E-05	100,6	1,01E-04	190,32	
	D2-C	2903,93	2,90E-05	110,7	1,11E-04	363,07	
	D2-D	2122,74	2,12E-05	92,4	9,24E-05	221,53	
	D2-E	1014,32	1,01E-05	73,5	7,35E-05	84,20	
	D2-F	1332,35	1,33E-05	77	7,70E-05	115,87	
	D2-G	1163,97	1,16E-05	38,5	3,85E-05	50,61	
	D2-H	918,36	9,18E-06	89	8,90E-05	92,31	
0,7% La	D3-A	387,50	3,88E-06	64	6,40E-05	28,01	29,29 ± 3,2
	D3-B	277,44	2,77E-06	100	1,00E-04	31,34	
	D3-C	293,55	2,94E-06	86	8,60E-05	28,51	
	D3-D	Physical default					
	D3-E	Physical default					
	D3-F	Physical default					
0,5% La	D2.1A	319,6	3,20 E-06	93,5	9,35 E-05	33,75	33,96 ± 2,3
	D2.1B	319,3	3,19 E-06	92,5	9,25 E-05	33,36	
	D2.1C	332,0	3,32 E-06	93,7	9,37 E-05	35,12	
	D2.1D	344,1	3,44 E-06	86,5	8,65 E-05	33,62	
0,7% La	D3.1A	276,2	2,76 E-06	87,7	8,77 E-05	27,35	26,83 ± 1,9
	D3.1B	309,3	3,09 E-06	75,3	7,53 E-05	26,31	
	D3.1C	284,0	2,84 E-06	83,5	8,35 E-05	26,78	

Appendix A
Data Tables for All Screen-Printed Samples

Table A-3 : Luminescent Samples

	Resistance MΩ	Luminescence nW	Average nW	Res*Lum W*Ohms
Com-P1	6,401	44,30	29,1	0,284
Com-P2	6,764	21,57	± 0,9	0,146
Com-P3	7,575	6,53		0,049
Com-P4	6,133	21,50	(No P2)	0,132
			52,3	
U1-P1	3,278	83,93	± 1,6	0,275
U1-P2	4,006	44,97		0,180
U1-P3	5,06	28,03		0,142
			42,3	
U2-P1	2,659	67,17	± 1,3	0,179
U2-P2	2,636	44,03		0,116
U2-P3	3,614	15,73		0,057
			47,6	
D1-P1	4,796	57,6	± 1,4	0,276
D1-P2	4,755	37,53		0,178
			83,7	
D2-P1	4,345	110,47	± 2,5	0,480
D2-P2	2,957	652,33	(No P2)	1,929
D2-P3	4,856	56,83		0,276
			59,0	
D3-P1	5,857	31,67	± 1,7	0,185
D3-P2	5,513	86,4		0,476
			65,9	
D2.1-P1	7,973	73,6	± 2,0	0,587
D2.1-P2	8,012	65,8		0,526
D2.1-P3	8,585	41,6		0,357
D2.1-P4	7,834	82,4		0,645
			38,9	
D3.1-P1	8,317	37,2	± 1,2	0,309
D3.1-P2	8,548	37,3		0,319
D3.1-P3	8,279	42,3		0,350

Appendix B
Error Calculations

Δε Method

The lowest and highest possible values of the dielectric constant are calculated within the uncertainties (with *C*, the capacitance per area, and *d*, the thickness of the sample):

$$\varepsilon_{min} = (\frac{2.835}{2.895}) \cdot (C \cdot 0.999) \cdot \frac{d - 4 \cdot 10^{-6}}{8.854 \cdot 10^{-12}}$$

$$\varepsilon_{max} = (\frac{2.895}{2.835}) \cdot (C \cdot 1.001) \cdot \frac{d + 4 \cdot 10^{-6}}{8.854 \cdot 10^{-12}}$$

The first term accounts for the area uncertainty, the second term represents the 0.1% uncertainty on the measured capacitance and the last term indicates the 4 μm uncertainty on the thickness measurements. Once we obtain these values, the substraction of these two gives us the full range of the uncertainty on the final result of ε, or two times the value of the error Δε :

$$\varepsilon_{min} - \varepsilon_{max} = 2\Delta\varepsilon$$

Although the ε_{min} and ε_{max} are usually not separated from the value of ε by exactly the same amount, the error Δε is considered a good representation of the uncertainty on the calculated value. Example with D2-B :

$$\varepsilon_{min} = 178{,}8 \qquad \varepsilon_{max} = 202{,}3$$

$$\Delta\varepsilon = 11{,}7 \qquad \varepsilon = 190{,}3 \pm 11{,}7 = 190{,}3 \pm 6\%$$

Appendix B
Error calculations

Partial Derivative Method

In chapter 3, the dielectric constant is shown to be equal to :

$$\varepsilon = d\frac{C}{\varepsilon_0 A}$$

The function contains two first order variables *d* and *C* (area constant in this project), that allow simple partial derivatives :

$$\frac{\delta\varepsilon}{\delta C} = \varepsilon_C = \frac{d}{\varepsilon_0} \qquad \frac{\delta\varepsilon}{\delta d} = \varepsilon_d = \frac{C}{\varepsilon_0 A}$$

The maximal error for the data obtained with this dielectric constant function can be calculated with :

$$|\Delta\varepsilon| \leq |\varepsilon_C(d_0, C_0)| \cdot \Delta C + |\varepsilon_d(d_0, C_0)| \cdot \Delta d$$

$$|\Delta\varepsilon| \leq \frac{d_0}{\varepsilon_0} \cdot \Delta C + \frac{C_0}{\varepsilon_0} \cdot \Delta d$$

The specific uncertainties on *C* change on each sample, but are constant for *d*.

Example with sample D2-B :

$$|\Delta\varepsilon| \leq \frac{10{,}1 \cdot 10^{-5} \cdot 1{,}83 \cdot 10^{-9}}{8{,}854 \cdot 10^{-12}} + \frac{1{,}675 \cdot 10^{-6} \cdot 4{,}0 \cdot 10^{-6}}{8{,}854 \cdot 10^{-12}}$$

$$|\Delta\varepsilon| \leq 0{,}019 + 0{,}757 = 0{,}776$$

$$\varepsilon = 190{,}32 \pm 0{,}78 = 190{,}32 \pm 0{,}41\%$$

References

[1] IEEE, *Standard Definitions of Terms for Radio Wave Propagation*, IEEE Standards Board (1997)

[2] Braslavsky S.E., Pure Appl. Chem. **79** (3) 293-465 (2007)

[3] Bhalla A.S., Guo R., Roy R., Mat. Res. Innovat. **4** (2000) 3-26

[4] Randall C.A., Newnham R. E., and Cross L. E., *History of the First Ferroelectric Oxide, $BaTiO_3$*, Materials Research Institute, The Pennsylvania State University, University Park, Pa, USA (2004)

[5] Haertling G.H., J. Am. Ceram. Soc., **82** (4) (1999) 797-818

[6] A. von Hippel, R. G. Breckenridge, F. G. Chesley, L. Tisza, Ind. Eng. Chem., 38 [11] (1946) 1097–109.

[7] Avila H.A., Reboredo M.M., Materials Research. Vol. 16 (4) (2013), pp. 839-843

[8] Hwang C.S., Park S.O., et al., Applied Physics Letters **67**, 2819 (1995)

[9] Balachandran R., Ong B.H., et al., Int. J. Electrochem. Sci. **7** (2012) 11895-11903

[10] Toyama T., Hama T., et al., Nanotechnology **20** (2009) 055203 (5 pp)

[11] Stojanovic B.D., Foschini C.R., et al., Ceramics International **28** (2002) 293-298

[12] Jaffe B., *Piezoelectric Ceramics*, book, Academic Press London and New York (1971)

[13] Barsoukov E., Macdonald J.R., *Impedance Spectroscopy: Theory, Experiment, and Applications,* Second Edition, book, Wiley-Interscience (2005)

[14] Vijatovic Petrovic M.M., Bobic J.D., Materials Chacterization Vol. 62 (2011) 1000-1006

[15] Beltran H., Cordoncillo E., Escribano P., J. Am. Ceram. Soc. **87** [11] (2005) 2132-2134

[16] Aoyagi S., Kuroiwa Y., Sawada A., Journal of Thermal Analysis and Calorimetry, Vol. 81 (2005) 627–630

[17] Wada S., Yasuno H. and Hoshina T., Journal of Applied Physics Vol. 42 (2003) pp.6188

[18] Tick T., et al., Journal of the European Ceramic Society **28** (2008) 837-842

[19] Piskunov S., Heifets E., Eglitis R.I., Borstel G., Computational Materials Science **29** (2004) 165-178

[20] Uchino K., Sadanaga E., Hirose T., J. Am. Ceram. Soc. **72** (8) (1989) 1555-58

[21] Frey M.H., Payne D.A., Physical Review B **54** (5) (1996) 3158-3168

[22] Harizanov O., Harizanova A., Ivanova T., Material Science and Engineering **B106** (2004) 191-195

[23] Kwei G.H., Lawson A.C., Billinge S.J.L., J. Phys. Chem. **97** (1993) 2368-2377

[23B] http://www.physchem.co.za/OB11-ele/capacitors.htm

[24] Panwar N.S., Semwal B.S., J. Phys. **36** (2) (1991) 163-166

[25] Puli, V.S., Li P., Adireddy S., Chrisey, D.B., Journal of Advanced Dielectrics **5** (3) (2015) 1550027 9 pp.

[26] Curecheriu, L., Vijatović Petrović, M. M., Appl. Phys. A **119** (2005) 681-686

[28] Guglielmi M., Kickelbick G., Martucci A., *Sol-Gel Nanocomposites*, book, Springer (2014)

[29] Gong, W., Li. J.-F. et. al., Acta Materialia **52** (2004) 2787-2793

[31] Bogner A., Jouneau P.-H., et al., Micron **38** (2007) 390-401

[32] Moncrieff D.A., Robinson V.N.E., Harris L.B., J. Phys. D : Appl. Phys. **11** (1978) 2315

[33] Egerton R., *Electron Energy-Loss Spectroscopy in the Electron Microscope*, book, Springer (2011)

[34] Hafner Bob, *Energy Dispersive Spectroscopy on the SEM : A Primer*, Websource, Characterization Facility, Universty of Minnesota (last visited on November 22nd 2015)

[34B] http://www3.nd.edu/~kamatlab/facilities_physchar.html

[35] Kniess C.T., Cardoso J., Prates P.B., Intech, ISBN: 978-953-51-0371-4 (2012)

[36] Kittel C., *Introduction to Solid State Physics*, 8th edition, Wiley (2005)

[36B] https://publish.illinois.edu/x-raycrystallography/

[37] Avila H.A., Reboredo M., Castro M., Parra R., Materials Research **16** (4) (2013) 839-843

[38] Watts J.F., Vacuum **45.6** (1994) 653-671

[39] Hollander J.M., Jolly W.L., Accounts of Chemical Research **3.6** (1970) 193-200

[40] Wu Q.-H., Liu M., Jaegermann W., Materials Letters **59** (2005) 1980-1983

[41] B., Han C., Zheng L. et al., Scientific Reports **5** (2015) 9443

[42] http://xpssimplified.com/elements/lanthanum.php

[43] http://www.zygo.com/?/met/profilers/opticalprofilersabout.htm

[44] Poon C.Y., Bhushan B., Wear **190** (1995) 76-88

[45] Novak M., http://www.photonics.com/Article.aspx?AID=49296

[46] http://www.azom.com/article.aspx?ArticleID=3249

[47] Sluyters J.H., Oomen J,J.C., Recueil **79** (1960) 1101-1110

[48] Sluyters J.H, Recueil **79** (1960) 1092- 1100

[49] Macdonald D.D., Electrochimica Acta **51** (2006) 1376-1388

[50] Esteban J.M., Orazem M.E., J. Electrochem. Soc. **138** (1) (1991) 67-76

[51] Lasia A., *Electrochemical Impendace Spectroscopy and its Applications*, book, Springer (2014)

[52] http://www.indiana.edu/~hightech/fpd/papers/ELDs.html

[53] Degenhardt H., Naturwissenschaften **63** (1976) 544-549

[54] J. Peatross and M. Ware, *Physics of Light and Optics*, 2015 edition, book, available at optics.byu.edu

[55] http://www.gamma-sci.com/photometry/

[56] Almeida A.F.L., Fechine P.B.A., Góes, J.C. et al., Materials Science and Engineering B **111** (2004) 113-123

[57] Chen F., Xiang Y., *Luminescent Materials and Applications*, book, Wiley, Chichester (2008)

[58] Munasinghe C., Heikenfeld J. et al., IEEE Transactions on Electron Devices **52** (2) (2005)

[59] Vasquez R.P. , Physical Review B, **54,** 21 (1991) 14398-14941

[60] Baldo M.A., O'Brien D.F. et al., Nature **395** (1998) 151-154

[61] Farinola G.M., Ragni R., Chem. Soc. Rev. **40** (2011) 3467-3482

[62] Lee K., Lee J.., Kang H. et al., ACS Nano **8** (5) (2014) 4893-4901

[63] http://departments.icmab.es/leem/siesta/

[64] Soler J.M., Artacho E., Gale J.D. et al, *Journal of Physics : Condensed Matter*, **14** (11), 2745-2779